2018

The synthesis and characterization of compounds with framework elements of contrasting reactivities {B, Si}-{P, As}

Katherine Woo
Iowa State University

The synthesis and characterization of compounds with framework elements of contrasting reactivities {B, Si}-{P, As}

by

Katherine E. Woo

A dissertation submitted to the graduate faculty

in partial fulfillment of the requirements for the degree of

DOCTOR OF PHILOSOPHY

Major: Inorganic Chemistry

Program of Study Committee:
Kirill Kovnir, Major Professor
Gordon Miller
Julia Zaikina
Javier Vela
Vitalij Pecharsky

The student author, whose presentation of the scholarship herein was approved by the program of study committee, is solely responsible for the content of this dissertation. The Graduate College will ensure this dissertation is globally accessible and will not permit alterations after a degree is conferred.

Iowa State University

Ames, Iowa

2018

TABLE OF CONTENTS

Page

LIST OF FIGURES v

LIST OF TABLES viii

ACKNOWLEDGMENTS ix

ABSTRACT xi

CHAPTER 1. INTRODUCTION 1
1.1 References 4

CHAPTER 2. Mg-Si-As: AN UNEXPLORED SYSTEM WITH PROMISING NONLINEAR OPTICAL PROPERTIES 5
2.1 Introduction 5
2.2 Experimental Section 6
2.3 Methods 9
2.3.1 Powder X-Ray Diffraction (XRD) 9
2.3.2 In Situ Powder Synchrotron XRD 9
2.3.3 Single-Crystal XRD 10
2.3.4 Differential Scanning Calorimetry (DSC) 10
2.3.5 Electronic Structure Calculations 12
2.3.6 Diffuse Reflectance Spectroscopy 12
2.3.7 Powder SHG 12
2.3.8 LDT Measurements 13
2.4 Results and Discussion 13
2.4.1 Synthesis 13
2.4.2 Thermal Stability 15
2.4.3 Chemical Stability 16
2.4.4 Crystal Structure 16
2.4.5 Electronic and Optical Properties 21
2.4.6 Second Harmonic Generation and Laser Damage Threshold 27
2.5 Conclusion 29
2.6 Acknowledgements 29
2.7 References 30

CHAPTER 3. SUPERSEDING VAN DER WAALS WITH ELECTROSTATIC INTERACTIONS: INTERCALACTION OF Cs INTO THE INTERLAYER SPACE OF $SiAs_2$ 33
3.1 Introduction 33
3.2 Experimental 34
3.2.1 Synthesis 34
3.2.2 Powder and Single Crystal X-Ray Diffraction (XRD) 35
3.2.3 In Situ Powder Synchrotron XRD 37

3.2.4 Scanning Electron Microscopy (SEM) and Energy Dispersive X-Ray Spectroscopy (EDS) 37
3.2.5 Differential Scanning Calorimetry (DSC) 39
3.2.6 Sintering 39
3.2.7 Transport Properties 39
3.3 Results and Discussion 39
3.3.1 Synthesis 40
3.3.2 Crystal Structure 42
3.3.3 Metal Substitution Content in $Cs_{0.16}M_xSi_{1-x}As_2$ (M = Cu, Zn, Ga) 47
3.3.4 Transport Properties 49
3.4 Conclusion 50
3.5 Acknowledgments 51
3.6 References 51

CHAPTER 4. BP: SYNTHESIS AND PROPERTIES OF BORON PHOSPHIDE 54
4.1 Introduction 54
4.2 Methods 55
4.2.1 Powder X-Ray Diffraction (XRD) 55
4.2.2 Synchrotron XRD 55
4.2.3 Raman Spectroscopy 55
4.2.4 Solid-State UV-Vis Spectroscopy 55
4.2.5 Scanning Electron Microscopy and Energy Dispersive X-Ray Spectroscopy 56
4.3 Synthesis 56
4.3.1 High-Temperature Solid-State Synthesis from Elements 56
4.3.2 Sn Flux Synthesis 56
4.3.3 Solid-State Metathesis Synthesis 57
4.4 Results and Discussion 58
4.4.1 Synthesis 58
4.4.2 Powder XRD 59
4.4.3 Synchrotron XRD 60
4.4.4 Raman Spectroscopy 62
4.4.5 Elemental Analysis 63
4.4.6 Optical Properties 64
4.4.7 Chemical Stability 66
4.4.8 Sn-Doped BP 66
4.5 Conclusion 67
4.6 Acknowledgements 67
4.7 References 68

CHAPTER 5. SYNTHESIS OF METAL BORIDES USING BI_3 AS A BORON SOURCE 70
5.1 Introduction 70
5.2 Methods 71
5.2.1 Powder X-Ray Diffraction (XRD) 71
5.2.2 In Situ Powder Synchrotron XRD 71
5.2.3 Scanning Electron Microscopy (SEM) and Energy Dispersive X-Ray Spectroscopy (EDS) 72

5.3 Synthesis 72
5.4 Results and Discussion 73
5.4.1 Synthesis 73
5.4.2 In Situ Powder XRD 75
5.4.3 Topotactic Reaction 77
5.4.4 Ternary Borides 78
5.5 Conclusion 80
5.6 Acknowledgements 80
5.7 References 81

CHAPTER 6. EXPLORATION OF NOVEL INORGANIC COMPOUNDS WITH B-P COVALENT BONDS 82
6.1 Introduction 82
6.2 Methods 84
6.2.1 Synthesis 84
6.2.2 Powder X-Ray Diffraction (XRD) 84
6.2.3 In Situ Powder Synchrotron XRD 84
6.2.4 Single Crystal XRD 85
6.3 Results & Discussion 86
6.3.1 Solid State Metathesis 86
6.3.2 Na_2BP_2 90
6.3.3 Non-Copper In Situ Experiments 92
6.3.4 BI_3 Transport Reaction 93
6.3.5 Direct Reaction of Elements 93
6.4 Conclusions 94
6.5 Acknowledgements 94
6.6 References 95

CHAPTER 7. CONCLUSIONS 97
7.1 References 100

LIST OF FIGURES

Page

Figure 1.1 Change in crystal structure with increasing valence electron count (VEC) from bulk Si to As. Local coordination with lone pairs is shown at the bottom. Si: blue, As: black. 2

Figure 1.2 Change in crystal structure with increasing VEC with boron represented by its B_{12} cluster and phosphorus represented by the basic unit of red phosphorus. B: green, P: red. 3

Figure 2.1 Calculated and experimental powder XRD patterns of $MgSiAs_2$ (left) and $Mg_3Si_6As_8$ (right). 2.7(1)% Si and 4.4(2)% SiAs are present as admixtures in the $Mg_3Si_6As_8$ sample based on the profile fitting (admixture peaks are shown with triangles). 7

Figure 2.2 In situ powder XRD of the formation of $Mg_3Si_6As_8$. The results of phase analysis are shown on the left for each region. 14

Figure 2.3 DSC curves for $MgSiAs_2$ (top) and $Mg_3Si_6As_8$ (bottom). 15

Figure 2.4 Crystal structure of A) $MgSiAs_2$ and B) M $g_3Si_6As_8$ (face and body diagonal) with C) ball - and - stick models of $MgAs_4$ from both compounds. $Mg@As_4$ tetrahedra are shown in gold and $Mg@As_6$ octahedra are shown in green. Mg: green, Si: blue, As: black. 17

Figure 2.5 Crystal structure of the Si-As framework in A) $Mg_3Si_6As_8$ and B) SiAs with $Si_2@As_6$ shown as purple octahedra. Mg: green, Si: blue, As: black. 20

Figure 2.6 Crystal structure of $Mg_3Si_3As_8$ showing A) polyhedra around Mg sites and B) polyhedra highlighting the Si-As framework. $Mg@As_4$: gold tetrahedra, $Mg@As_6$: green octahedra, $Si@As_4$: blue tetrahedra, Mg: green, Si: blue, As: black. 21

Figure 2.7 Band structure (top) and density of states (bottom) for $MgSiAs_2$ and $Mg_3Si_6As_8$. Partial contribution of each element is shown in color: Mg: red; Si: blue, As: green. 22

Figure 2.8 High resolution band structure of $Mg_3Si_6As_8$ emphasizing valence band maxima and conduction band minima. 22

Figure 2.9 COHP plots of Si and Mg interactions with As in $MgSiAs_2$ (top) and in $Mg_3Si_6As_8$ (bottom). Corresponding crystal structure polyhedra are shown. 24

Figure 2.10 Solid state UV–vis direct bandgap Tauc plots for $MgSiAs_2$ and $Mg_3Si_6As_8$. 26

Figure 2.11 Diffuse reflectance spectrum of $MgSiAs_2$ (top) and $Mg_3Si_6As_8$ (bottom) with Kubelka-Munk conversion measured with a Thermo Scientific Evolution 220 Spectrometer. 26

Figure 2.12 Absorbance spectrum (top) and direct band gap Tauc plot (bottom) of $Mg_3Si_6As_8$ measured with a BLACK-Comet C-SR-100 spectrometer. 27

Figure 2.13 Comparison of SHG intensity of $MgSiAs_2$ and $AgGaS_2$ at 55–88 µm particle size. 28

Figure 3.1 Projection of crystal structure of $SiAs_2$ (top) and its rearrangement into $Cs_{0.16}Zn_{0.08}Si_{0.92}As_2$ (bottom) through translational motion, as depicted by the blue arrows. Cs: yellow; Si and Zn: blue, As: black. Unit cells are shown as gray rectangles. 42

Figure 3.2 Coordination of both Cs positions to As in $Cs_{0.16}Zn_{0.08}Si_{0.92}As_2$ (top) and $Cs_8Zn_{18}As_{28}$ (bottom). Cs: yellow, Si: blue, Zn: pink, As: black, vacancies: white. Mixed/partial site occupancies are shown as colored fractions. 43

Figure 3.3 Cs disorder between Si/Zn-As layers with all possible positions displayed (left) and potential Cs ordering (right). Cs: yellow, Si: blue, Zn: pink, As: black. 44

Figure 3.4 All possible Cs positions in $Cs_{0.16}SiAs_{1.95}$ (left) and coordination of Cs3 to As (right). Cs1 and Cs2: yellow, Cs3: beige, Si: blue, As: black, vacancies: white. 45

Figure 3.5 Crystal structure of $Cs_{0.11}Zn_{0.05}Si_{0.95}As$ in comparison with SiAs. Unit cell is marked by a black box. Cs: yellow, Si: blue, Zn: pink, As: black. 46

Figure 3.6 Normalized resistivity measurements for selected crystals of each substituting metal, M, in $Cs_{0.16}M_xSi_{1-x}As_2$. 49

Figure 4.1 Normalized powder x-ray diffraction patterns for BP-E (I, black), BP-F (II, blue), BP-SSM before reannealing (IIIa, magenta) and BP-SSM after reannealing (IIIb, orange) along with the reference pattern. Inset shows the low angle region, indicating the presence of crystalline boron starting material in BP-E and BP-F. Calculated unit cell parameters are given on the left. 60

Figure 4.2 Normalized synchrotron powder x-ray diffraction patterns of BP-E (I, black) and BP-F (II, blue). Asterisks indicate unreacted crystalline boron. Inset shows enlarged 1.01–1.0475 Å range. 61

Figure 4.3 Left: normalized Raman spectra of BP-E (I, black), BP-F (II, blue), and BP-SSM (III, orange). Right: each Raman spectrum true to scale. 62

Figure 4.4 Energy dispersive x-ray spectra for BP-E (I), BP-F (II), and BP-SSM (III). Insets show a magnified region from 0–5 keV in which Sn or I peaks would appear. 63

Figure 4.5 Left: Kubelka–Munk converted spectra for BP-E (I, black), BP-F (II, blue), and BP-SSM (III, orange). Right: $(\alpha h\nu)^2$ vs. energy plots. 65

Figure 5.1 Powder XRD patterns of TiB_2, Fe_2B, Co_2B, and Ni_3B. Red lines correspond to calculated powder patterns. 74

Figure 5.2 Contour plot of in situ powder XRD patterns upon the reaction of Ni and BI_3. On top is the resulting powder pattern with tic marks corresponding to calculated positions for Ni_2B and NiI_2. Asterisks mark artifacts in the powder pattern. 76

Figure 5.3 Photos of A) Ni foam, B) Ni_3B foam, and C) a powder XRD pattern of the Ni_3B foam. Asterisks mark peaks of Ni_2B. 77

Figure 5.4 EDS spectrum (top) and powder XRD (bottom) of Ni_2CoB. High background is due to fluorescence contribution from Co. 79

Figure 6.1 Structurally characterized compounds containing at least one B–P covalent bond. 83

Figure 6.2 Schematic of the reaction of Na_3BP_2 and a metal halide and resulting products after oxidation or water washing. 86

Figure 6.3 Powder XRD pattern of the product “Na-Cu-B-P” from the reaction of Na_3BP_2 and CuCl. 87

Figure 6.4 Contour plot of in situ powder synchrotron XRD patterns for “Na-Cu-B-P” heating up to 1123 K. 89

Figure 6.5 Contour plot of in situ powder synchrotron XRD patterns for “Na-Cu-B-P” heating up to 805 K. 89

Figure 6.6 Theoretical B insertion between phosphorus atoms or partial Cu substitution in $NaCu_2P_2$. 90

Figure 6.7 Crystal structure of Na_2BP_2 with A) all boron and average phosphorus positions shown, B) the B-P chain showing all possible positions, and C) a hypothetical B-P chain taking into account reasonable B-P bond distances of 1.7-2.1 Å. 91

LIST OF TABLES

Page

Table 2.1 Crystal data and structure refinement details for $MgSiAs_2$, $Mg_3Si_6As_8$, $Mg_3Si_3As_8$, and $Mg_{3-x}Zn_xSi_3As_8$. 11

Table 2.2 Atomic coordinates and displacement parameters for $MgSiAs_2$ and $Mg_3Si_6As_8$ ... 18

Table 2.3 Bond distances and Mg polyhedra bond angles in $MgSiAs_2$ and $Mg_3Si_6As_8$..... 19

Table 2.4 Integrated COHP energies for individual bond interactions..... 25

Table 2.5 LDTs of $MgSiAs_2$ and $AgGaS_2$ (as the reference) 28

Table 3.1 Data collection and unit cell parameters..... 38

Table 3.2 Data collection and unit cell parameters of $Cs_{0.11}Zn_{0.05}Si_{0.95}As$ 41

Table 3.3 Compositions of $Cs_yM_xSi_{1-x}As_2$..... 48

Table 5.1 Starting ratios for select metal borides 73

Table 5.2 Ratio of Ni:BI_3 starting reagents and corresponding products detected by powder XRD..... 75

Table 6.1 Data collection and unit cell parameters of Na_2BP_2 85

Table 6.2 Comparison of lab powder X-ray and in situ synchrotron results of main phosphide compounds. Temperature of lab synthesis and formation in synchrotron experiments is listed after each compound..... 92

ACKNOWLEDGMENTS

I would first like to express my utmost gratitude to my advisor, Prof. Kirill Kovnir. Not only did you accept me into your group, you somehow found the patience to give me the guidance I needed while dealing with my idiosyncrasies. I thank you for the extensive knowledge and stories that you imparted about science, techniques, and random things in life. Thank you for that initial push for me to attend a conference, and thank you for enabling and supporting me to go to all the conferences thereafter. Thank you for establishing a productive lab culture while still understanding (and sometimes encouraging) the need for vacation time. Thank you for being the integral cause for my growth as a scientist and as a person by encouraging me to experience events and opportunities that put me outside my comfort zone. I am so thankful to have been in your group these past five years, and I am very proud to have you as my mentor.

I would also like to thank my dissertation committee members, Prof. Gordie Miller, Prof. Julia Zaikina, Prof. Javier Vela, and Prof. Vitalij Pecharsky, for their support and helpful feedback during my year at Iowa State University. Thank you to Prof. Zaikina for access to your instruments at ISU, and thank you for all your help at UC Davis.

Back at UC Davis, thank you to Prof. Susan Kauzlarich and Prof. Frank Osterloh for providing easy access to your instruments and for the helpful discussions on my projects. I appreciate the collaborative working environment created between our labs.

Thank you to my amazing friends, old and new, Vicky Tran, Eumi Ko, Brianna Payne, and Justin Mark for all the support and companionship during my journey into (educational) madness. Thank you to Kathy Lee, Shannon Lee, and Josh Greenfield for not only being such helpful and knowledgeable lab mates, but also being such wonderful friends

whom I could rely on both in and outside of lab. I would not have survived my years at UC Davis or my final year at ISU without the guidance and care all of you have shown me.

Thank you to my family for their unending love and support, even when my research was beyond the scope of their understanding. I am very thankful for all the efforts you all put in to make sure I didn't have to worry much about things outside of the lab. Thank you for helping me even get this far.

Thank you to Ashton Liu, Will Liu, and Paul Lummis for stepping in completely unasked to help me and make sure I was going to be okay during some particularly rough times. We may not communicate too frequently, but your actions really mattered and cheered me up more than you know.

Thank you to the rest of my lab mates for the fun times and help provided. Thank you to my undergraduate Joshua Chang for your hard work and perseverance, even when nothing seemed to work until the very end. Thank you to Joe Mazzetti for being such a great and encouraging friend, even though you weren't my undergraduate. Thank you to Jian Wang for sharing your wealth of knowledge and for being so reliable. I learned a lot from working with you as a lab mate and collaborator. Thank you to the rest of my collaborators, both local and international. So much was accomplished with your help.

Lastly, thank you to my late bunny, Tesla, and my happy current bunny, Yuki, for giving me silent companionship as I came home from long days at the lab. Your presence and love blocked any feelings of loneliness and provided me with easy and relaxing happiness.

ABSTRACT

The reactivity difference between boron or silicon with phosphorus or arsenic creates challenges in synthesis. Synthesizing ternary compounds increases the level of complexity. The syntheses of new multinary compounds consisting of covalent bonds between these elements of drastically different reactivities have been investigated, and the resulting products were characterized.

Between silicon and arsenic, a completely new set of compounds in the Mg-Si-As system were discovered, as well as a highly versatile family of $Cs_{0.16}M_xSi_{1-x}As_2$ (M = Cu, Zn, Ga). Compounds in the Mg-Si-As system seem to show a preference with crystalizing in non-centrosymmetric space groups, which is uncommon through solid state synthesis methods. $MgSiAs_2$ has been studied theoretically for years, but had never been realized experimentally. With its now successful synthesis, $MgSiAs_2$ displays a good balance of second harmonic generation response and laser damage threshold. $Mg_3Si_6As_8$ has a space group of $P4_332$ (No. 212), which is in the one Laue class, 432, that does not allow second harmonic generation, but electronic structure calculations suggest the compound may be used as a thermoelectric material upon doping. Layered $Cs_{0.16}M_xSi_{1-x}As_2$ (M = Cu, Zn, Ga) compounds show potential as a thermoelectric material due to the anisotropic 2D crystal structure. Their ability to substitute various metals into the layered framework without altering the crystal structure introduces the option of tuning the material.

Using BI_3 as a boron source was investigated for the reaction with phosphorus and various metals. This method allowed BP to be synthesized very quickly at moderate temperatures and with low contamination compared to flux reactions or the direct reaction of boron and phosphorus. These advantages transferred to the synthesis of metal borides, and

Ni_2CoB was produced when starting with a NiCo alloy. To explore the formation of metal boron phosphide compounds containing covalent B-P bonds, solid state metathesis between Na_3BP_2 and metal halides, mainly CuCl, was performed. In situ powder X-ray diffraction experiments were utilized in conjunction with lab experiments to gain insight on a new "Na-Cu-B-P" compound. Surprisingly, a new non-centrosymmetric Na_2BP_2 compound with the space group of *Pna*2_1 (No. 33) was discovered in a reaction of leaching Na from Na_3BP_2 using CuI and a CsI/NaI flux.

CHAPTER 1. INTRODUCTION

One of the many struggles in solid state inorganic chemistry stem from the difficulty in synthesizing compounds containing elements with vastly different reactivities. For instance, boron and silicon have extremely high melting points of 2352 K and 1683 K with elemental bond energies of 297 kJ/mol and 222 kJ/mol, respectively [1]. Common modes of boride and silicide syntheses involve extreme temperatures achieved through arc-melting or the reduction of oxides, in which contamination may pose a problem [2]. These methods are unsuitable when attempting to form boron or silicon compounds with more volatile elements, such as phosphorus or arsenic. Unlike Group 13 and 14 elements, Group 15 elements easily reach a gaseous state at temperatures below 773 K when under vacuum. Associate challenges include high vapor pressures within the reaction vessel and inhomogeneous mixing of reactants. In spite of synthetic difficulties, these compounds have promising properties for a variety of technological applications. For example, SiP_2 has been studied for use in Li-batteries and BP can act as a photocatalyst for H_2 evolution or be used as protective coating [3]. BAs was calculated to have extraordinarily high thermal conductivity (although experimental data has yet to achieve the reported values) and was studied as a photoelectrode [4].

In addition to properties of interest, the combination of inert B or Si with reactive P or As gives rise to interesting structures. Silicon atoms are commonly found in a tetrahedral coordination, with elemental Si crystalizing with a diamond crystal structure. Arsenic contains an electron lone-pair, whose repulsion causes the formation of layers in elemental As. Together, Si and As form two compounds, SiAs and $SiAs_2$ (Figure 1.1). The introduction of a third element tends to disrupt the layering in the Si-As binaries and instead forms a 3D

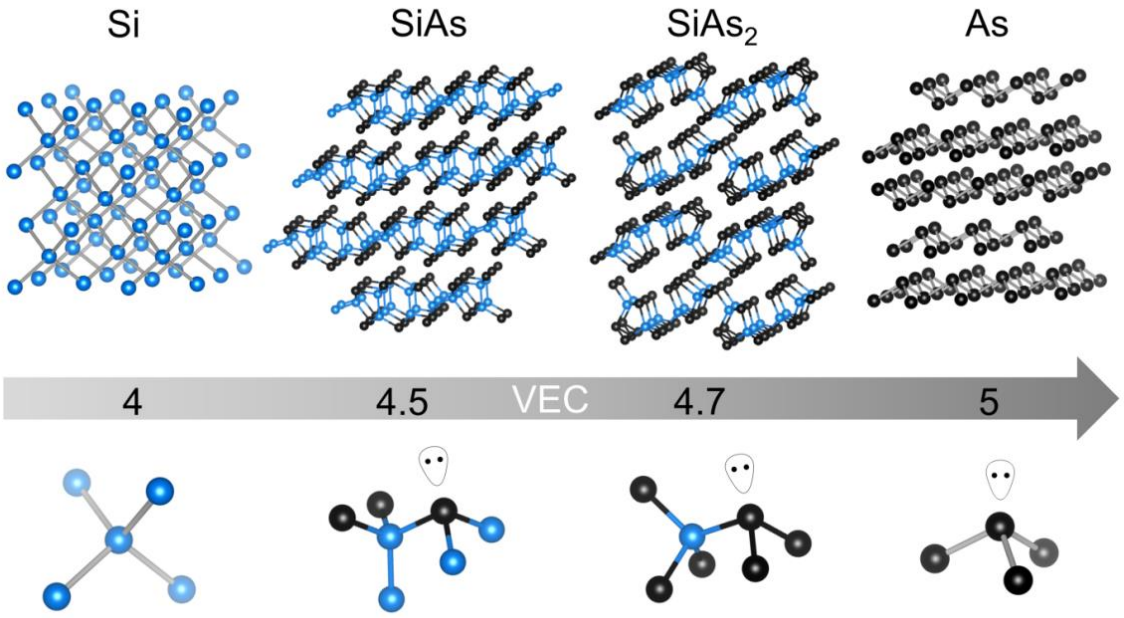

Figure 1.1 *Change in crystal structure with increasing valence electron count (VEC) from bulk Si to As. Local coordination with lone pairs is shown at the bottom. Si: blue, As: black.*

framework, such as those found in Li_2SiAs_2, $Eu_3Si_2As_4$, $CdSiAs_2$, and Ni_2SiAs [5] to name a few. Compounds that still contain 2D Si-As layers are fewer in number and include KSi_3As_3 and $LnSiAs_3$ (Ln = La, Ce, Pr) [6]. The properties that arise from a material are largely influenced by its crystal structure. $CdSiAs_2$, for instance, crystallizes in the space group *I*-42*d*. This space group belongs to the set of non-centrosymmetric space groups that are expected to exhibit second-harmonic generation. Second-harmonic generation is an industrially-relevant nonlinear optical process in which the frequency of an input laser is doubled. Exploring the incorporation of various cations in the Si-As system may form compounds with new 3D structures or possibly retain the 2D layers through intercalation, which may give rise to interesting properties and potential applications.

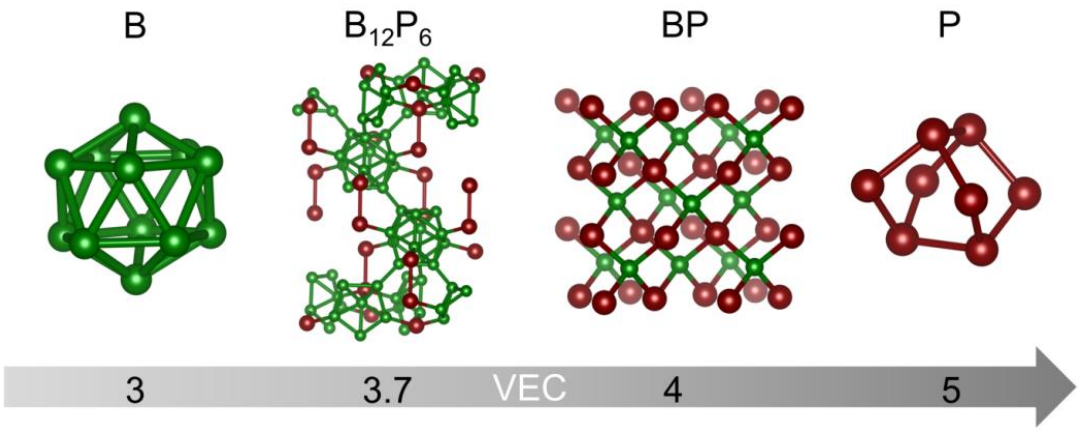

Figure 1.2 *Change in crystal structure with increasing VEC with boron represented by its B_{12} cluster and phosphorus represented by the basic unit of red phosphorus. B: green, P: red.*

Elemental boron has a unique structure formed by B_{12} icosahedron clusters, and its chemistry is known to be more similar to that of silicon than the rest of the Group 13 elements [2b, 7]. Its preference to form covalent bonds and ability to participate in multicenter bonding, as seen in B_2H_6 and $B_{12}H_{12}$, allows boron compounds to have structures containing a wide variety of components, such as chains, nets, and clusters. Boron combined with phosphorus or arsenic forms two types of compounds, either $B_{12}P_2$ and $B_{12}As_2$, which contain boron icosahedra, or cubic zincblende BP and BAs (Figure 1.2). As the VEC increases to 4, BP loses the B_{12} clusters and takes on the same tetragonal coordination as bulk Si, which also has a VEC of 4. The structures taken by binary B-P compounds are drastically different from one another. The addition of a third element then begs the question, how will this third element alter the structure? The information is scarce for boron and phosphorus phases, and there are currently only nine inorganic ternary compounds that contain a B-P bond. The search for better methods of synthesizing boron compounds with other elements, especially volatile elements such as P or As, is needed to expand this list of known ternary B-P compounds so that we may understand the structures and properties that may arise.

1.1 References

[1] C.D. Schaeffer, Jr., C.A. Strausser, M.W. Thomsen, C.H. Yoder. *Data for General, Organic, and Physical Chemistry* **1989**.

[2] a) G. Gouget, P. Beaunier, D. Portehault, C. Sanchez. *Faraday Discuss.* **2016**, *191*, 511; b) R.B. King, *Encyclopedia of Inorganic Chemistry, 2nd ed.*, John Wiley and Sons, Inc., Hoboken, NJ, USA, **2005**.

[3] a) H.-T. Kwon, C.K. Lee, K.-J. Jeon, C.-M. Park. *ACS Nano* **2016**, *10*, 5701; b) B.C. Monachan, A.D. Morrison, E.M. Waddell, D.R. Gibson, S.A.D. Wilson, K.L. Lewis. *Proc. SPIE* **1992**, *10261*, 91; c) A.A. Ogwu, T. Hellwig. *Int. J. Electrochem. Sci.* **2014**, *9*, 8299.

[4] a) L. Lindsay, D.A. Broido, T.L. Reinecke. *Phys. Rev. Lett.* **2013**, *111*, 025901; b) J. Kim, D.A. Evans, D.P. Sellan, O.M. Williams, E. Ou, A.H. Cowley, L. Shi. *Appl. Phys. Lett.* **2016**, *108*, 201905; c) B. Lv, Y. Lan, X. Wang, Q. Zhang, Y. Hu, A. J. Jacobson, D. Broido, G. Chen, Z. Ren, C.-W. Chu. *Appl. Phys. Lett.* **2015**, *106*, 074105; d) N.H. Protik, J. Carrete, N.A. Katcho, N. Mingo, D. Broido. *Phys. Rev. B.* **2016**, *94*, 045207; e) S. Wang, S.F. Swingle, H. Ye, F.-R.F. Fan, A.H. Cowley, A.J. Bard. *J. Am. Chem. Soc.* **2012**, *134*, 11056.

[5] a) K. Lee, *Synthesis and Characterization of Tetrel Pnictides and Compounds in the Lithium-Tetrel-Arsenic System*, University of California, Davis, **2016**; b) X.-C. Liu, S.-Q. Xia, X.-W. Lei, M.-Y. Pan, X.-T. Tao. *Eur. J. Inorg. Chem.* **2014**, *2014*, 2248; c) B.B. Sharma, A.A. Vaipolin, Y.A. Valov. *J. Struct. Chem.* **1971**, *1971*, 726; d) O.N. Il'nitskaya, Y.B. Kuz'ma. *Russ. J. Inorg. Chem.* **1990**, *35*, 1938.

[6] a) W.M. Hurng, J.D. Corbett, S.L. Wang, R.A. Jacobson. *Inorg. Chem.* **1987**, *26*, 2392; b) H. Hayakawa, S. Ono. **1988**, *144*, 177.

[7] F.A. Cotton, G. Wilkinson. *Advanced Inorganic Chemistry, 4th ed.*, John Wiley and Sons, Inc., New York, USA, **1980**.

CHAPTER 2. Mg-Si-As: AN UNEXPLORED SYSTEM WITH PROMISING NONLINEAR OPTICAL PROPERTIES

The contents of this chapter have been published in Advanced Functional Materials. Woo, K.; Wang, J.; Wu, K.; Lee, K.; Dolyniuk, J.; Pan, S.; Kovnir, K. Adv. Funct. Mater. ***2018,*** *28, 1870209.*

2.1 Introduction

Nonlinear optical (NLO) materials play a key role in laser science and technology due to their ability to upconvert frequencies of incoming light. This technology is widely used in solid state lasers [1]. Only crystallographically non-centrosymmetric (NCS) compounds can have NLO performance according to the Neumann principle. Based on their transmission and applied spectrum scope, NLO materials can be classified as UV-NLO materials, visible-NLO materials, or infrared-NLO (IR-NLO) materials. IR-NLO materials are technologically relevant due to their use in optoelectronic devices, resource exploration, and long-distance laser communications applied in the infrared region (2-20 μm) [2]. Certain commercial IR-NLO materials, such as $AgGaX_2$ (X = S, Se) [3] and $ZnGeP_2$ [4], have high second harmonic generation (SHG) coefficients. The widespread application of current IR commercial materials is hindered by many intrinsic drawbacks, such as low laser damage thresholds (LDT) or two-photon absorption [5]. Therefore, searching for new IR-NLO materials with higher LDT is an important challenge for materials chemistry in the IR-NLO field.

Many members of the ABC_2 family are IR-NLO materials. This NLO family covers a broad scope of chemical compositions where either A^{II} = Mg, Zn, Cd; B^{IV} = Si, Ge, Sn; and C^{V} = P, As, Sb; or A^{I} = Ag, Au; B^{III} = Ga, In; and C^{VI} = S, Se, Te [6]. ABC_2 compounds crystallize within the chalcopyrite structure type in the space group *I*-42*d* (No. 122). The commercial IR-NLO materials $AgGaX_2$ (X = S, Se) [6c] and $ZnGeP_2$ [6b] belong to this

family. Other ABC_2 compounds, such as $ZnSiP_2$ and $CdSiP_2$, have recently garnered significant interest due to their potential as IR-NLO materials or for luminescence applications [7]. In addition to excellent performance as IR-NLO materials, the ABC_2 family compounds have also been widely explored for photovoltaic and optical applications [8]. Despite its mature investigational history, the ABC_2 family is far from being fully explored. Many compounds are only predicted by theory, and their experimental properties are rarely reported [8a, 9]. $MgSiAs_2$ is one of these cases. To the best of our knowledge, $MgSiAs_2$ has only been reported by theorists via simulations of its crystal structure combined with calculations of physical properties. As the first ternary compound in the Mg-Si-As system, $MgSiAs_2$ crystallizes as a crystallographically NCS structure with good SHG performance. Another NCS compound, $Mg_3Si_6As_8$, was also discovered during the exploration of the Mg-Si-As system. Herein, we present the first experimental syntheses of these compounds, crystal structure determinations by single crystal diffraction, thermal and chemical stabilities, optical bandgaps, and SHG and LDT properties.

2.2 Experimental Section

All preparation and handling of samples were performed in an argon-filled glove box with the O_2 level below 1 ppm. Magnesium turnings (Alfa Aesar, 99.98%), crystalline silicon powder (Alfa Aesar, 99.99%), polycrystalline arsenic lump (Alfa Aesar, 99.99999+%), and polycrystalline bismuth lump (Alfa Aesar, 99.998%) were all used as received.

$MgSiAs_2$ Crystal: A single crystal of $MgSiAs_2$ was originally found in reaction products of a sample containing Mg, Ge, As, and CsCl. The reaction mixture was placed in an evacuated and flame-sealed silica tube, which was annealed at 1123 K. After cooling, a red transparent crystal was found as a side phase. The source of Si was from the reduction of the silica ampoule with either Mg or Ge.

$MgSiAs_2$ Powder: Single-phase polycrystalline samples of $MgSiAs_2$ were synthesized by loading Mg:Si:As = 1.2:1:2 into carbonized silica ampoules under ambient conditions. The ampoules were sealed under vacuum ($\approx 10^{-2}$ mbar) and then heated up to 1123 K over 17 h and annealed at that temperature for 144 h. After cooling to room temperature, the ampoules were opened in the glove box, the samples were ground with an agate mortar and pestle, and then reannealed with the same heating profile as previously reported. The annealing and grinding cycle was completed a total of three times. Single-phase $MgSiAs_2$ was finally collected after acid treatment ($HCl:H_2O$ = 1:1) of the annealed powder (Figure 2.1).

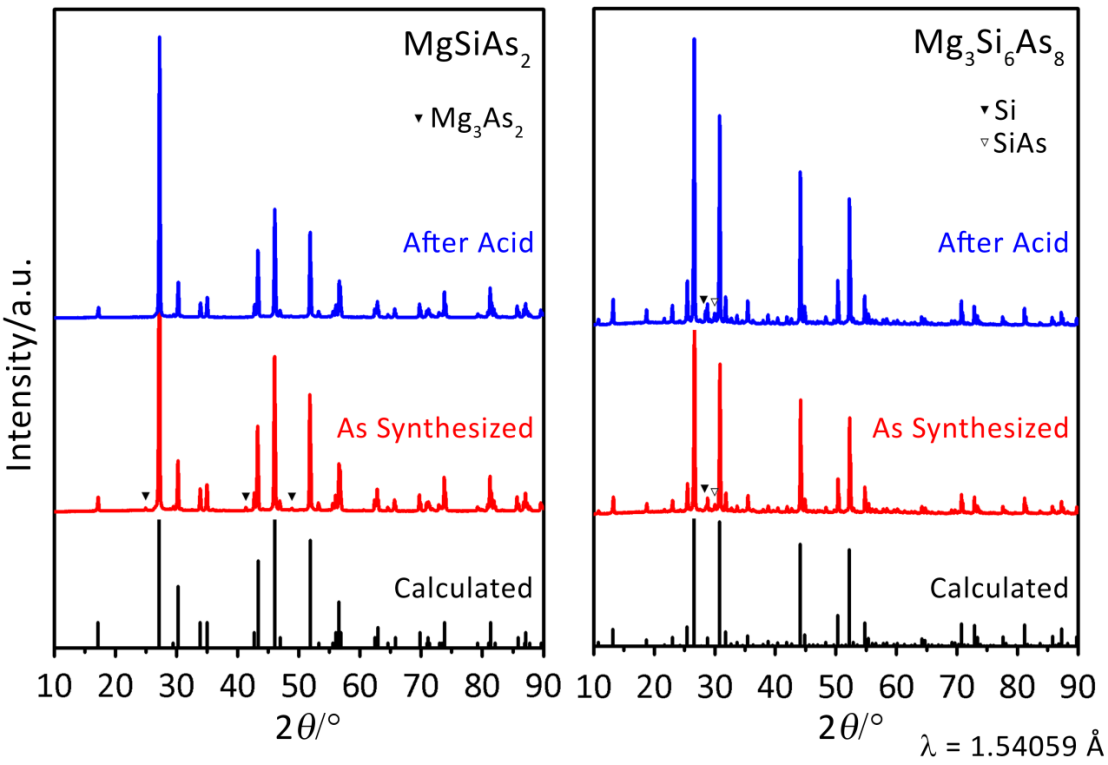

Figure 2.1 *Calculated and experimental powder XRD patterns of $MgSiAs_2$ (left) and $Mg_3Si_6As_8$ (right). 2.7(1)% Si and 4.4(2)% SiAs are present as admixtures in the $Mg_3Si_6As_8$ sample based on the profile fitting (admixture peaks are shown with triangles).*

$Mg_3Si_6As_8$ Crystal: Single crystals of $Mg_3Si_6As_8$, measuring up to $3 \times 1.5 \times 1$ mm^3, were grown using stoichiometric ratios of Mg, Si, and As and a 50 molar excess of Bi flux. The mixture was loaded into evacuated and flame-sealed carbonized silica ampoules with silica wool placed at the top end of the ampoule to be used as a filter during centrifugation. The sample was heated to 1123 K in 17 h and annealed for 140 h. Bi flux was subsequently removed by high-temperature centrifugation. Any remaining Bi was dissolved in a wash of one part glacial acetic acid (Alfa Aesar, 99+%) and three parts water with 2% volume of hydrogen peroxide (Fisher Chemical, 30%). A few milliliters of concentrated HCl (Fisher Chemical, 37% w/w) was used to remove any Bi_2O_3 that remained in the wash after the initial filtering. The products were filtered and rinsed with water, and then air dried. Red single crystals were manually picked out for further analysis and stored in an argon filled glove box.

$Mg_3Si_6As_8$ Powder: Almost phase-pure polycrystalline samples of $Mg_3Si_6As_8$ were synthesized by first loading carbonized silica ampoules with stoichiometric ratios of Mg, Si, and As under ambient conditions with a total weight of 0.5 g. All attempts to scale the synthesis to higher quantities resulted in incomplete reactions. The same heating profile for $MgSiAs_2$ powders was used. After the first annealing, the products were ground in an agate mortar and pestle in the glove box, and additional Mg (about 1 molar ratio for $Mg_3Si_6As_8$) was added. Three sets of grinding and annealing were sufficient to acquire an almost pure target phase. The resulting sample still contained small admixtures of Si and SiAs even after washing with $HCl:H_2O$ (Figure 2.1). The produced red powder was stored in an argon filled glove box.

$Mg_3Si_3As_8$ Crystal: This compound was discovered during the exploration of a quaternary system containing Zn. The crystal structure was first obtained with a quaternary composition with partial Mg/Zn substitution. The single crystal of $Mg_3Si_3As_8$ was obtained during a 5 g scale synthesis of $Mg_3Si_6As_8$ without flux where the reaction annealed for 20 days at 1123 K in an evacuated carbonized silica ampoule. All our attempts to synthesize a single-phase sample of $Mg_3Si_3As_8$ using procedures similar to those described above failed. All samples were contaminated by significant amounts of $Mg_3Si_6As_8$ and $MgSiAs_2$.

Further details of the crystal structure investigations on $MgSiAs_2$ and $Mg_3Si_6As_8$ may be obtained from the Fachinformationszentrum Karlsruhe, 76344 Eggenstein-Leopoldshafen (Germany), on quoting the depository numbers CSD-434187 and CSD-434188. In addition, the data were deposited to The Cambridge Crystallographic Data Centre, CCDC Nos. 1824592 and 1824593.

2.3 Methods

2.3.1 Powder X-Ray Diffraction (XRD)

Powder XRD patterns were acquired using a Rigaku Miniflex 600 diffractometer and Cu-Kα radiation with a Ni-K_β filter. The sample was ground into a fine powder with an agate mortar and pestle and analyzed on zero-background Si holders.

2.3.2 In Situ Powder Synchrotron XRD

A slice of Mg was cut from a piece of Mg turning and pushed to the bottom of a silica capillary (0.5 mm ID × 0.7 mm OD, Friedrich & Dimmock, Inc.). About 10 mg of finely ground and homogeneous mixture of Si and As in stoichiometric ratio for $Mg_3Si_6As_8$ was then added. The capillary was evacuated and flame sealed. Beamline 17-BM-B at Advanced Photon Source at Argonne National Lab was used. The sample was loaded onto a flow cell equipped with electric heaters and exposed to synchrotron radiation (λ = 0.45336 Å). Data

were collected during heating at 15 K min^{-1} until 1123 K, dwelled for 20 min at that temperature, and then cooled at 15–50 K min^{-1} to room temperature. Temperatures were calibrated by comparing the observed melting points of sealed capillary samples of elemental Sn, Sb, and Ge to their expected melting points. GSAS-II was used for data processing and analysis [10].

2.3.3 Single-Crystal XRD

Data collection for $MgSiAs_2$ and $Mg_3Si_6As_8$ was performed at 90 K on a Bruker AXS SMART diffractometer with an APEX-II CCD area detector and Mo-Kα radiation (λ = 0.71073 Å). Data for $Mg_3Si_3As_8$ and $Mg_{3-x}Zn_xSi_3As_8$ were collected at 100 K on a D8 VENTURE diffractometer with a Photon CMOS detector and Mo-$I_{\mu s}$ microsource. Raw data integration was performed with either the APEX2 or APEX3 software [11], and multiscan absorption corrections were applied. Crystal structure solution and refinement was carried out using the SHELX suite [12]. $MgSiAs_2$ was refined as a two-component twin. Data collection and structure refinement details are found in Table 2.1 for $MgSiAs_2$ (ICSD 434187), $Mg_3Si_6As_8$ (ICSD 434188), $Mg_3Si_3As_8$, and $Mg_{3-x}Zn_xSi_3As_8$ (x = 0.4). Crystal structure images were generated using VESTA [13].

2.3.4 Differential Scanning Calorimetry (DSC)

DSC measurements were executed using a Netzsch STA 449 F3 Jupiter Differential Scanning Calorimeter for $MgSiAs_2$ powder (15.6 mg) and a Netzsch 404 F3 Pegasus Differential Scanning Calorimeter for $Mg_3Si_6As_8$ powder (15.5 mg). Finely ground powders were sealed in evacuated silica ampoules and heated to 1373 K and cooled to 323 K at a rate of 5 K min^{-1}.

Table 2.1 *Crystal data and structure refinement details for $MgSiAs_2$, $Mg_3Si_6As_8$, $Mg_3Si_3As_8$, and $Mg_{3-x}Zn_xSi_3As_8$.*

Composition	**$MgSiAs_2$**	**$Mg_3Si_6As_8$**	**$Mg_3Si_3As_8$**	**$Mg_{2.6}Zn_{0.4}Si_3As_8$**
Formula weight (g/mol)	202.24	840.83	756.56	772.98
Temperature (K)	90(2)		100(2)	
Radiation, λ	Mo-Kα, 0.71073 Å			
Space group	*I*-42*d* (No. 122)	$P4_332$ (No. 207)	*Pnma* (No. 62)	
a (Å)	5.9078(8)	11.600(1)	12.5046(6)	12.4519(4)
b (Å)			7.6471(3)	7.6444(3)
c (Å)	10.600(2)		12.9975(6)	12.9298(4)
V (Å^3)	369.96(12)	1560.9(6)	1242.9(1)	1230.75(7)
Z	4			
ρ_{calc} (g cm^{-3})	3.63	3.58	4.04	4.17
Absorption coefficient (mm^{-1})	18.29	17.46	21.62	22.58
Reflections/param.	289/13	816/28	1521/74	2006/76
R_1 [$I > 2\sigma(I)$]	0.008	0.011	0.012	0.015
R_1 (all data)	0.008	0.011	0.014	0.017
wR_2 [$I > 2\sigma(I)$]	0.019	0.025	0.027	0.029
wR_2 (all data)	0.019	0.025	0.028	0.032
Goodness-of-fit	1.14	1.11	1.27	1.24
Diff. peak/hole (e Å^{-3})	0.26/-0.30	0.37/-0.24	0.57/-0.83	0.72/-0.60

2.3.5 Electronic Structure Calculations

Electronic structure calculations and bonding analyses were carried out using the tight binding-linear muffin tin orbitals-atomic sphere approximation (TB-LMTO-ASA) program [14]. The Barth–Hedin exchange potential was employed for local density approximation (LDA) calculations [15]. The radial scalar-relativistic Dirac equation was solved to obtain the partial waves. The basis set used contained Mg(3s,3p), Si(3s,3p), and As(4s,4p) orbitals with downfolded Mg(3d), Si(3d), and As(4d) functions. The density of states (DOS), band structures, and crystal orbital Hamilton populations (COHP) were calculated after converging the total energy on a dense *k*-mesh of 12 × 12 × 12 points with 262 irreducible *k*-points for $MgSiAs_2$ and 16 × 16 × 16 points with 200 irreducible *k*-points for $Mg_3Si_6As_8$.

2.3.6 Diffuse Reflectance Spectroscopy

Powders of $MgSiAs_2$ and $Mg_3Si_6As_8$ were pressed onto a glass slide wrapped with Teflon tape and white filter paper. A Thermo Scientific Evolution 220 spectrometer was used to obtain UV–vis diffuse reflectance data from 250 to 1100 nm, which were then converted by the Kubelka–Munk function. Additional measurements were performed using a BLACK-Comet C-SR-100 spectrometer.

2.3.7 Powder SHG

The SHG response measurement was performed by the Kurtz and Perry method with a 2.09 μm Q-switch laser [16]. The $MgSiAs_2$ sample was finely ground and sieved to select particles in the 55–88 μm size range. Microcrystalline $AgGaSe_2$ of the same particle size range was used as a reference. The samples were placed on a glass microscope cover slide, secured by a 1 mm thick silicone insole with an 8 mm diameter hole, and then covered with another glass slide. The samples were then placed into light-tight boxes and explored under a

pulsed infrared beam from a Q-switched Ho:Tm:Cr:YAG laser with a wavelength of 2.09 μm. The SHG signals were recorded on an oscilloscope that was connected to the detector.

2.3.8 LDT Measurements

LDT was measured using a 1064 nm Q-switch laser on a ground powder of $MgSiAs_2$ crystals and $AgGaSe_2$ as a reference. The samples were surrounded by a 1 mm thick silicone pad with an 8 mm diameter hole and pressed between two glass slides. They were then fixed in a light-tight box with the plane surface explored under a pulsed laser beam (1064 nm, 10 ns). The pulse energy was raised from 0.2 mJ and stopped when obvious damage was discovered under a microscope after the irradiation.

2.4 Results and Discussion

2.4.1 Synthesis

The synthesis of $MgSiAs_2$ is challenging due to the low reactivity of Si versus the high reactivities and vapor pressure of Mg and As at elevated temperatures. Originally, a small red single crystal of $MgSiAs_2$ was detected as a product of a reaction of Mg, Ge, and As in CsCl flux performed in a silica tube. Reduction of SiO_2 with Mg is hypothesized to be the source of Si. Single phase powder of $MgSiAs_2$ was then synthesized by repeatedly annealing and grinding stoichiometric amounts of the elements with a 20% molar excess of Mg to account for its evaporation and reaction with the silica ampoule (see the Experimental Section for details). The $MgSiAs_2$ sample appeared to be a single phase after final acid treatment to remove traces of Mg_3As_2.

Similar to the discovery of $MgSiAs_2$, red single crystals of $Mg_3Si_6As_8$ were initially found as a minor product during the optimization of the synthesis of a Cs-Ni-Si-As compound using Mg and CsCl flux. Large crystals of the compound can be grown from Bi flux together with side products of elemental Si along with binary admixtures. For the

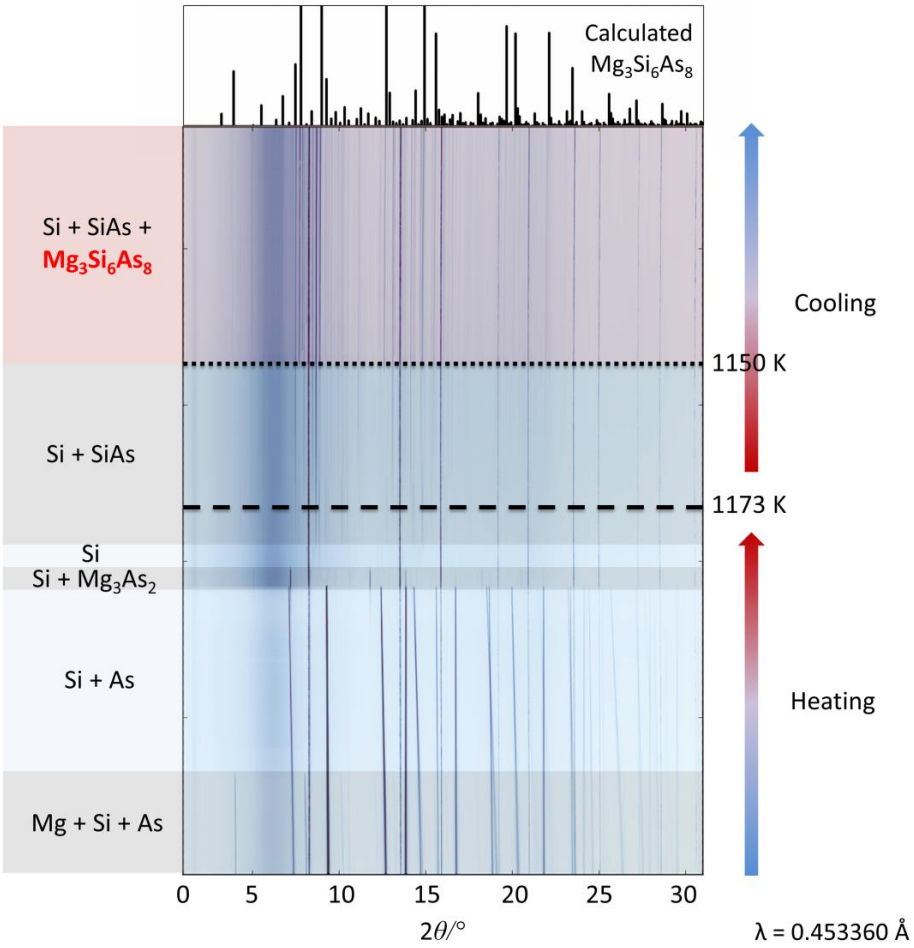

Figure 2.2 *In situ powder XRD of the formation of $Mg_3Si_6As_8$. The results of phase analysis are shown on the left for each region.*

optimization of the reaction conditions for stoichiometric synthesis from elements, in situ powder XRD was applied. It revealed the formation of $Mg_3Si_6As_8$ at 1150 K upon cooling of the melt (Figure 2.2). A competing phase, SiAs, formed at higher temperatures during cooling, and elemental Si remained in the sample throughout the experiment. The temperature of formation of $Mg_3Si_6As_8$ as detected by in situ powder XRD, 1150 K, is lower than the formation onset detected by DSC experiments, 1240 K. This discrepancy was observed for other pnictide containing systems [17]. The best quality sample of $Mg_3Si_6As_8$ was synthesized by repeatedly annealing and grinding stoichiometric amounts of the

elements with a 33% molar excess of Mg (see the Experimental Section for details). Small admixtures of Si and SiAs remained in the sample, and further grindings and annealing were ineffective to increase phase purity. Adding more than 33% of Mg after the first annealing caused the reduction of $Mg_3Si_6As_8$ into Si and SiAs as well as the appearance of Mg_3As_2.

2.4.2 Thermal Stability

Differential scanning calorimetry experiments revealed that $MgSiAs_2$ decomposed at 1140 K (Figure 2.3), which was confirmed by annealing $MgSiAs_2$ at 1200 K. The annealing resulted in a mixture of Mg_3As_2 and $SiAs_2$. $Mg_3Si_6As_8$ demonstrates higher thermal stability than $MgSiAs_2$, as it melts or decomposes at 1240 K (Figure 2.3). Powder XRD performed on the sample after the DSC run revealed that $Mg_3Si_6As_8$ had partially degraded into a mixture of SiAs, $SiAs_2$, As, and $MgSiAs_2$.

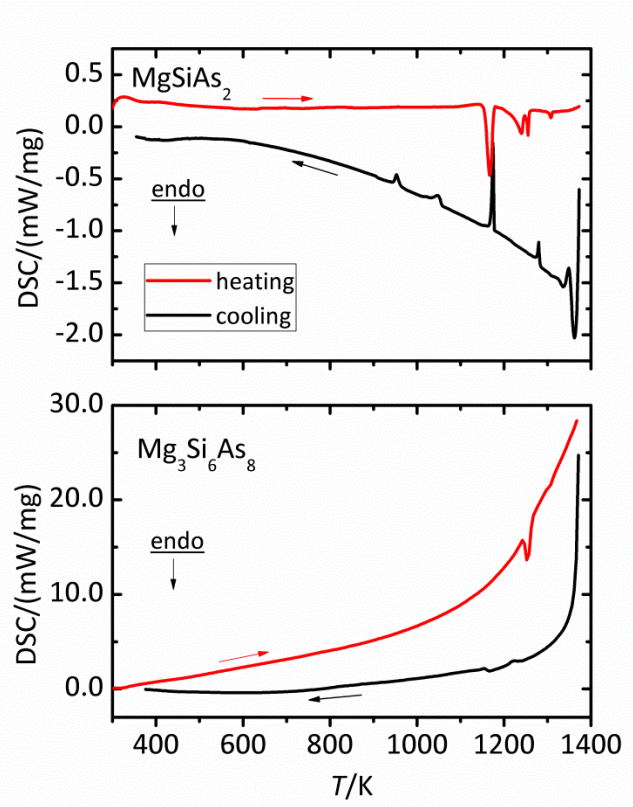

Figure 2.3 *DSC curves for $MgSiAs_2$ (top) and $Mg_3Si_6As_8$ (bottom).*

2.4.3 Chemical Stability

Both $MgSiAs_2$ and $Mg_3Si_6As_8$ can be left in air for a week without degradation, however several weeks exposure resulted in partial decomposition. A change in color was not evident in $MgSiAs_2$ while single crystals of $Mg_3Si_6As_8$ eventually lost their red clarity and attained a dull iridescent sheen. Powder XRD did not reveal any significant chemical change to $Mg_3Si_6As_8$, suggesting slow surface oxidation occurred. $MgSiAs_2$ was resistant to a 1 HCl:1 H_2O treatment for 2 h. No change was observed for $Mg_3Si_6As_8$ after overnight exposure to concentrated HCl and HNO_3. When bathed in fresh aqua regia (1 HNO_3:3 HCl) overnight, $Mg_3Si_6As_8$ single crystals retained their shape, though a surface oxidation reaction may have occurred causing the crystal to visibly lose color from outside in. The resulting outer clear portion of the crystals was found to be amorphous and did not diffract X-rays.

2.4.4 Crystal Structure

Following the trend of other II-IV-V_2 compounds, $MgSiAs_2$ crystallizes in the tetragonal space group *I*-42*d* (No. 122) in a chalcopyrite structure type (Figure 2.4a). In this compound, all atoms are tetrahedrally coordinated and each element has one unique position in the unit cell. Si is bonded to four As atoms, which are in turn bonded to two Si atoms and two Mg atoms. The As atoms form a distorted tetrahedron around Mg. Tetragonal distortion is very common among ternary chalcopyrite compounds and can be evaluated by the deviation of the lattice parameter ratio *c*/*a* from 2. In the case of $MgSiAs_2$, the *c*/*a* ratio is 1.79, making the distortion comparable to that of $AgGaS_2$ [6].

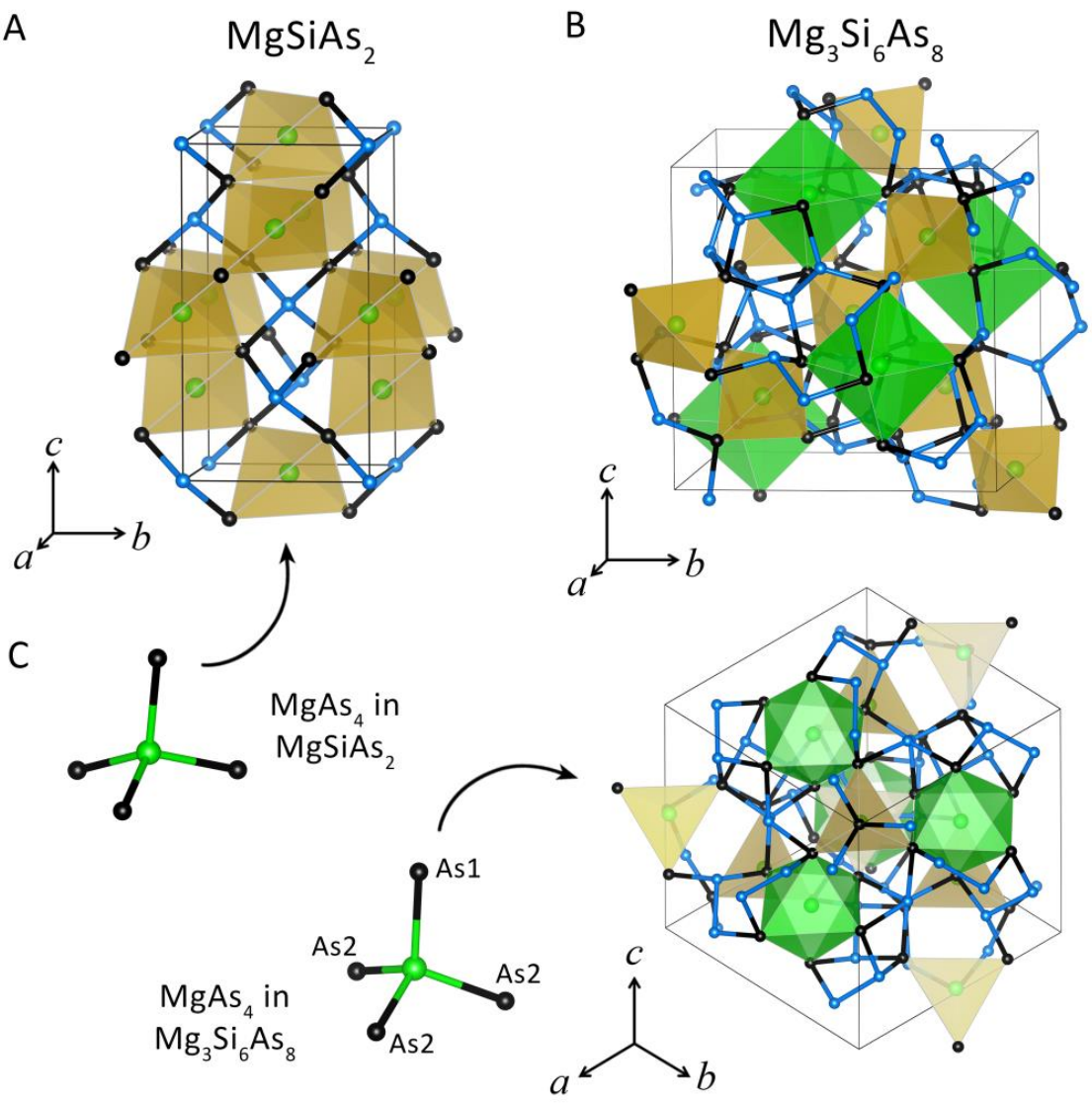

Figure 2.4 *Crystal structure of A) $MgSiAs_2$ and B) M $g_3Si_6As_8$ (face and body diagonal) with C) ball-and-stick models of $MgAs_4$ from both compounds. Mg@As_4 tetrahedra are shown in gold and Mg@As_6 octahedra are shown in green. Mg: green, Si: blue, As: black.*

$Mg_3Si_6As_8$ crystallizes in the non-centrosymmetric cubic space group $P4_332$ (No. 207), Pearson symbol *cP*68 with Wyckoff sequence e^2c^2a. This space group/sequence combination is not yet listed in the Inorganic Crystal Structure Database (ICSD), indicating that this is a new structure type. The structure consists of a complex Si-As framework with Mg cations interspersed within (Figure 2.4b). Mg has two distinct environments, surrounded

by As in either a tetrahedral or an octahedral arrangement, which is also observed in $R_2Mg_3SiAs_6$ (R = La, Ce) [18]. In the crystal structure of $Mg_3Si_6As_8$, the Mg-centered polyhedra spiral along the 4_3 screw axes down the cardinal directions through the center of each face.

While both crystal structures of Mg-Si-As compounds contain distorted Mg@As_4 tetrahedra (Figure 2.4c), the Mg@As_4 unit in $MgSiAs_2$ is distorted through their bond angles, deviating 4°–10° from the ideal tetrahedral bond angle of 109.5° (Table 2.3). In contrast, the distortion in $Mg_3Si_6As_8$ is mainly due to the varied Mg-As bond distances of 2.690(1) and 2.5791(6) Å (Table 2.3). The bond distances in these tetrahedra average out to the average Mg-As bond length found in Mg_3As_2 (2.64 Å) [19]. The distances in the Mg@As_6 octahedra, 2.8541(4) Å, are much longer than those in the tetrahedra, but are comparable to distances in inorganic magnesium arsenides such as $MgAs_4$ (2.71–2.92 Å) [20], KMgAs (2.84 Å) [21], $Mg_4Ir_7As_6$ (2.90 Å) [22], $R_2Mg_3SiAs_6$ (2.69–2.86 Å) [18], and KMg_4As_3 [23].

Table 2.2 *Atomic coordinates and displacement parameters for $MgSiAs_2$ and $Mg_3Si_6As_8$*

Atom	***Wyckoff***	***x/a***	***y/b***	***z/c***	U_{eq} (Å^2)
			$MgSiAs_2$		
As1	8*d*	0.21308(7)	¼	⅛	0.0041(2)
Si1	4*a*	0	0	0	0.0045(4)
Mg1	4*b*	0	0	½	0.0065(5)
			$Mg_3Si_6As_8$		
As1	8*c*	0.39431(1)	0.60569(1)	0.10569(1)	0.00416(6)
As2	24*e*	0.61625(1)	0.36053(1)	0.12046(1)	0.00429(5)
Si1	24*e*	0.94939(4)	0.82057(4)	0.08177(4)	0.00466(9)
Mg1	8*c*	0.51044(5)	0.98956(5)	0.01044(5)	0.0063(2)
Mg2	4*a*	⅛	⅛	⅛	0.0070(3)

Table 2.3 *Bond distances and Mg polyhedra bond angles in $MgSiAs_2$ and $Mg_3Si_6As_8$*

Atoms	Bond distance (Å)	Atoms	Bond angle (°)
	$MgSiAs_2$		
Mg1 – As1	2.6096(3) ×4	∠ As1 – Mg1 – As1	118.973(9)
Si1 – As1	2.3498(3) ×4	∠ As1 – Mg1 – As1	104.939(4)
	$Mg_3Si_6As_8$		
Mg1 – As1	2.690(1)	∠ As1 – Mg1 – As2	110.94(2)
Mg1 – As2	2.5791(5) ×3	∠ As2 – Mg1 – As2	107.96(2)
Mg2 – As2	2.8541(4) ×6	∠ As2 – Mg2 – As2	91.447(4)
Si1 – Si1	2.306(1)	∠ As2 – Mg2 – As2	94.268(6)
Si1 – As1	2.4225(6)	∠ As2 – Mg2 – As2	83.336(6)
Si1 – As2	2.3423(6)		
Si1 – As2	2.3429(6)		

The Si-As framework in $Mg_3Si_6As_8$ is similar to that in the binary SiAs compound. In both cases, Si-Si dumbbells are surrounded by six As atoms. A 3D rhombus grid pattern of the $Si_2@As_6$ octahedra is created in the structure of $Mg_3Si_6As_8$ (Figure 2.5a), while in the crystal structure of SiAs such octahedra form 2D layers (Figure 2.5b). Each Si atom is four-coordinated to three As atoms and another Si, while As is coordinated to either three or two Si atoms.

Unlike $MgSiAs_2$ and $Mg_3Si_6As_8$, $Mg_3Si_3As_8$ and its Zn-doped variant crystallizes in the centrosymmetric space group *Pnma* (No. 62), Pearson symbol *oP*56 with Wyckoff sequence d^4c^6. This compound shares the Wyckoff sequence with B_4F_6-PF_3 [24] and α-P_4S_3 but exhibits different bonding connectivity [25]. Similar to $Mg_3Si_6As_8$, $Mg_3Si_3As_8$ has Mg in both distorted tetrahedral and octahedral environments (Figure 2.6a). These distortions are mainly through bond angles. The crystal structure of $Mg_3Si_3As_8$ can be derived from the structure of $MgSiAs_2$ by breaking the tetrahedral connectivity via insertion of As atoms to form As-As dumbbells (Figure 2.6b). All Si atoms in the structure of $Mg_3Si_3As_8$ are

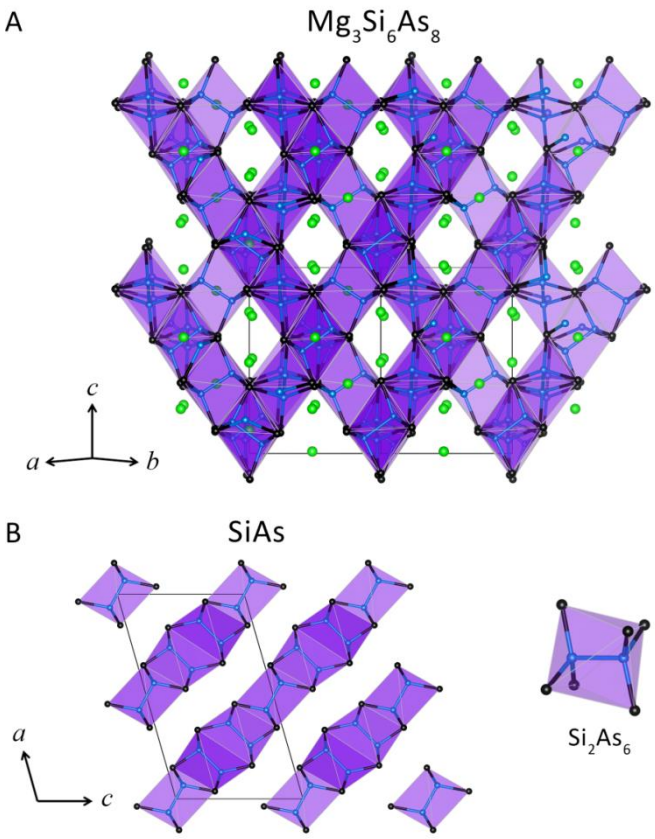

Figure 2.5 *Crystal structure of the Si-As framework in A) $Mg_3Si_6As_8$ and B) SiAs with $Si_2@As_6$ shown as purple octahedra. Mg: green, Si: blue, As: black.*

tetrahedrally coordinated by As. $Si@As_4$ tetrahedra share corners with three other $Si@As_4$ to form corrugated layers stacked along [001]. A part of the As-As dumbbells connects the layers together, while another part of the As-As dumbbells point towards open channels running along [010] where Mg atoms are situated. As such, there are effectively three types of As atoms: As within the layers that are two-coordinated to a Si and As atom, As connecting the layers that are three-coordinated to a Si and two other As atoms, and hanging As in the open channels that are single-coordinated to another As atom. The isostructural Zn-doped quaternary compound was also observed as described in the experimental section with Zn atoms partially occupying the tetrahedral Mg sites.

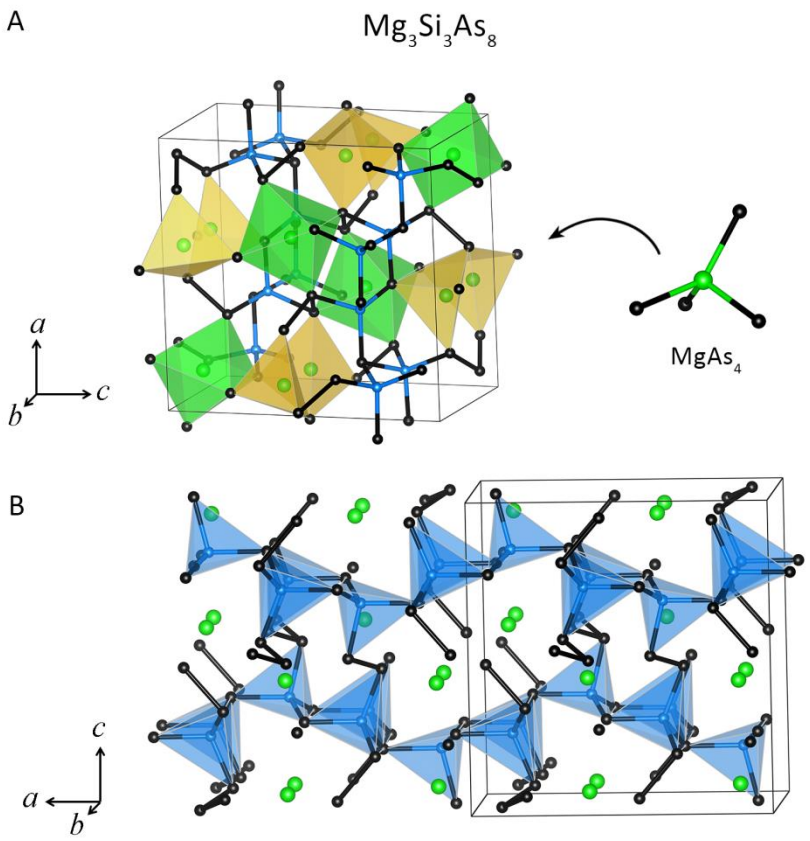

Figure 2.6 *Crystal structure of $Mg_3Si_3As_8$ showing A) polyhedra around Mg sites and B) polyhedra highlighting the Si-As framework. $Mg@As_4$: gold tetrahedra, $Mg@As_6$: green octahedra, $Si@As_4$: blue tetrahedra, Mg: green, Si: blue, As: black.*

2.4.5 Electronic and Optical Properties

According to electronic structure calculations, $MgSiAs_2$ and $Mg_3Si_6As_8$ are predicted to be direct or pseudo-direct bandgap semiconductors with 1.0 and 1.5 eV bandgaps, correspondingly (Figure 2.7 and Figure 2.8). The valence band of $Mg_3Si_6As_8$ has four maxima of the same energy: two in Γ-R, one in Γ-X, and one in Γ-M regions. The conduction band has a clear single minimum at the R point. The energy difference between direct and indirect transitions is very small, 0.03 eV, which makes the compound a pseudo-direct bandgap semiconductor. For $MgSiAs_2$ this prediction agrees with the bandgap energy calculated by Kocak et al. using the LDA method [9]. Another computational work using the

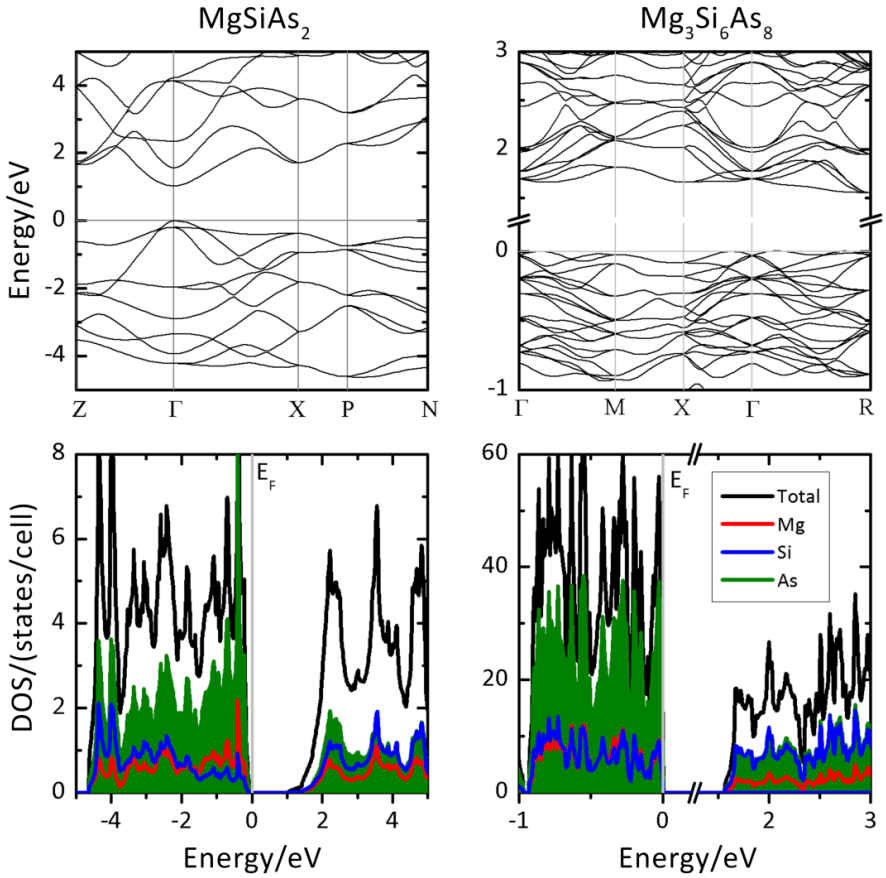

Figure 2.7 *Band structure (top) and density of states (bottom) for $MgSiAs_2$ and $Mg_3Si_6As_8$. Partial contribution of each element is shown in color: Mg: red; Si: blue, As: green.*

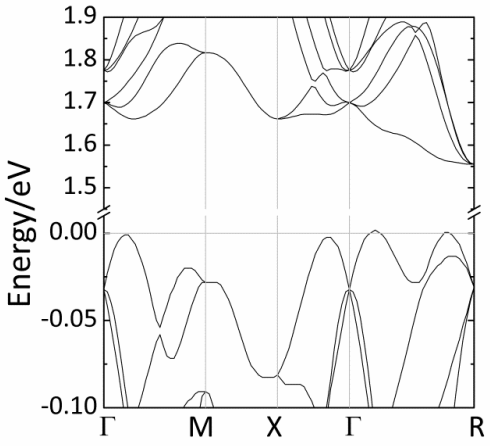

Figure 2.8 *High resolution band structure of $Mg_3Si_6As_8$ emphasizing valence band maxima and conduction band minima.*

modified Beck Johnson potential (mBJ) predicts $MgSiAs_2$ to be a direct semiconductor with a larger bandgap of 1.95 eV [8]. For both compounds, As provides the highest contribution to the states in the top of the valence band, while the contributions of Mg and Si are comparable. The steep slopes of DOS at the Fermi level resembles Sb-containing thermoelectrics with high thermopower [26]. Doping with a metal such as lithium may shift the compound into a heavily doped semiconductor state, which will be useful for an effective thermoelectric material.

Crystal orbital Hamilton population (COHP) is a computational tool for analysis of chemical bonding in solids with respect to the bonding and antibonding character of the electrons in their DOS. COHP partitions band-structure energy into orbital–pair interactions to estimate bond strengths [27]. COHP calculations show that the interactions in $MgSiAs_2$ and $Mg_3Si_6As_8$ are optimized with bonding states below the Fermi level and antibonding states above the Fermi level (Figure 2.9). Si-As and Si-Si interactions are the strongest as compared to Mg-As interactions in both compounds (Table 2.4). Bonding within the $Mg@As_4$ tetrahedra is stronger in $Mg_3Si_6As_8$ as given by its larger integrated COHP (-ICOHP) value of 4.71 eV/polyhedron compared to that in $MgSiAs_2$ with 3.41 eV/polyhedron. Within the $Mg@As_4$ tetrahedron in $Mg_3Si_6As_8$, the longer Mg1-As1 bond (2.69 Å) has an expected weaker orbital overlap, 1.19 eV/bond, as compared to the three other Mg1-As2 bonds in the tetrahedron, 1.76 eV/bond for the distance of 2.58 Å. The latter distance and orbital overlap are comparable to those in the $Mg@As_4$ tetrahedron in $MgSiAs_2$, 1.71 eV/bond for the distance of 2.61 Å. The increase of Mg-As distances in the $Mg@As_6$ octahedron to 2.85 Å leads to an expected weakening of the orbital overlap down to 0.87 eV/bond (Figure 2.9, Table 2.4).

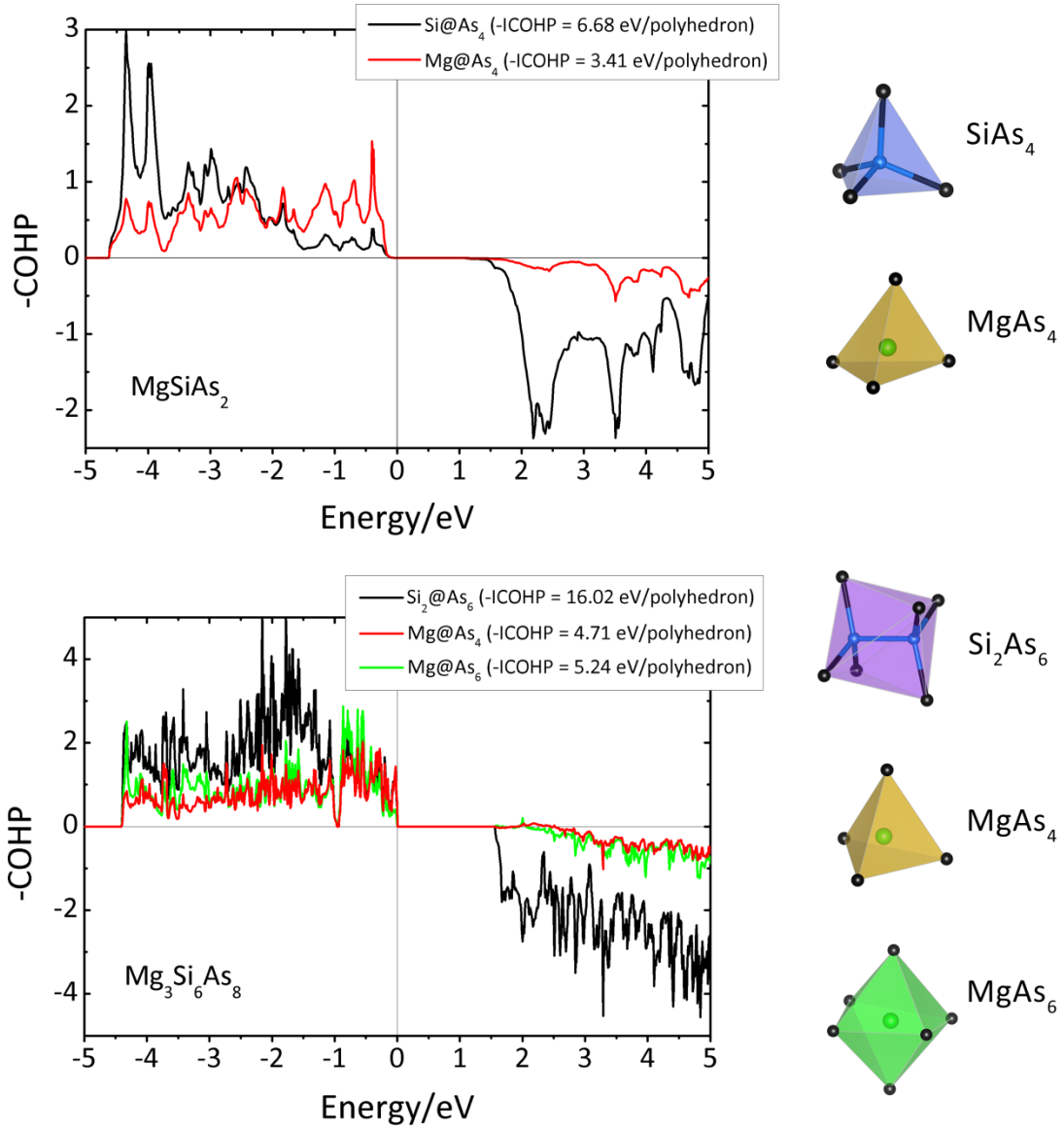

Figure 2.9 *COHP plots of Si and Mg interactions with As in $MgSiAs_2$ (top) and in $Mg_3Si_6As_8$ (bottom). Corresponding crystal structure polyhedra are shown.*

Table 2.4 *Integrated COHP energies for individual bond interactions*

Atoms	-ICOHP	Bond length (Å)
	$MgSiAs_2$	
Si1-As1	3.34 eV/bond	2.3500(3)
Mg1-As1	1.71 eV/bond	2.6096(3)
	$Mg_3Si_6As_8$	
Si1-Si1	2.77 eV/bond	2.306(1)
Si1-As1	2.35 eV/bond	2.4225(7)
Si1-As2	2.89 eV/bond	2.3423(7)
Si1-As2	2.84 eV/bond	2.3429(7)
Mg1-As1	1.19 eV/bond	2.690(1)
Mg1-As2	1.76 eV/bond	2.5791(6)
Mg2-As2	0.87 eV/bond	2.8541(4)

To characterize the optical bandgap, solid-state UV–vis spectroscopy was performed (Figure 2.10). Tauc plots generated from the Kubelka–Munk data revealed a direct bandgap of 1.83(5) eV for $MgSiAs_2$ and 2.02(8) eV for $Mg_3Si_6As_8$, which corresponds to the red color of both compounds. Several measurements on different batches of $Mg_3Si_6As_8$ were attempted, and all were of similar quality (Figures 2.11 and 2.12). The experimental bandgap values are higher than the calculated ones, though it is common for LDA calculation techniques to underestimate the actual value of the bandgap. The trend predicted by the electronic structure calculations was experimentally confirmed in which the bandgap for $MgSiAs_2$ is smaller than that for $Mg_3Si_6As_8$. Indirect bandgap values cannot be accurately determined probably due to significant contribution from defect scattering as observed by large Urbach tails.

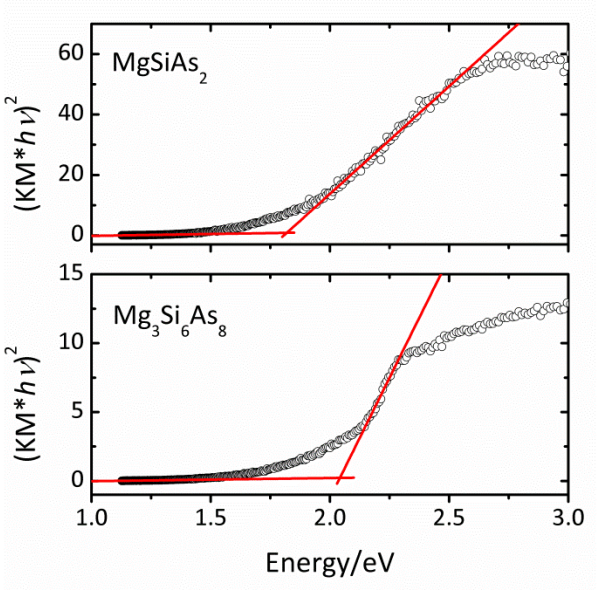

Figure 2.10 *Solid state UV–vis direct bandgap Tauc plots for $MgSiAs_2$ and $Mg_3Si_6As_8$.*

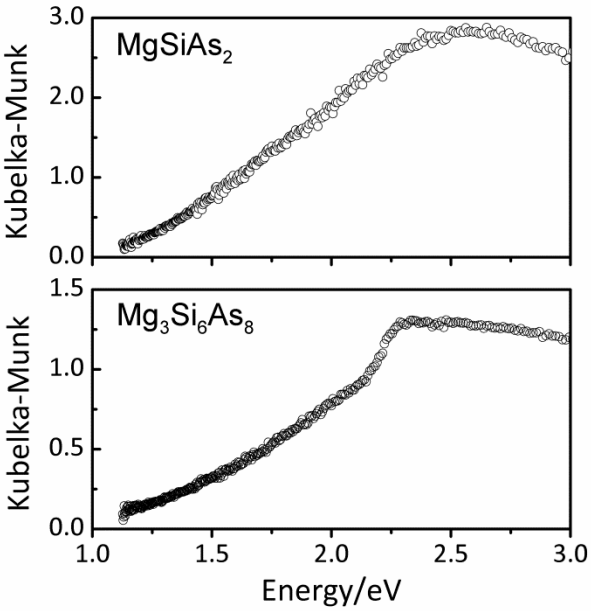

Figure 2.11 *Diffuse reflectance spectrum of $MgSiAs_2$ (top) and $Mg_3Si_6As_8$ (bottom) with Kubelka-Munk conversion measured with a Thermo Scientific Evolution 220 Spectrometer.*

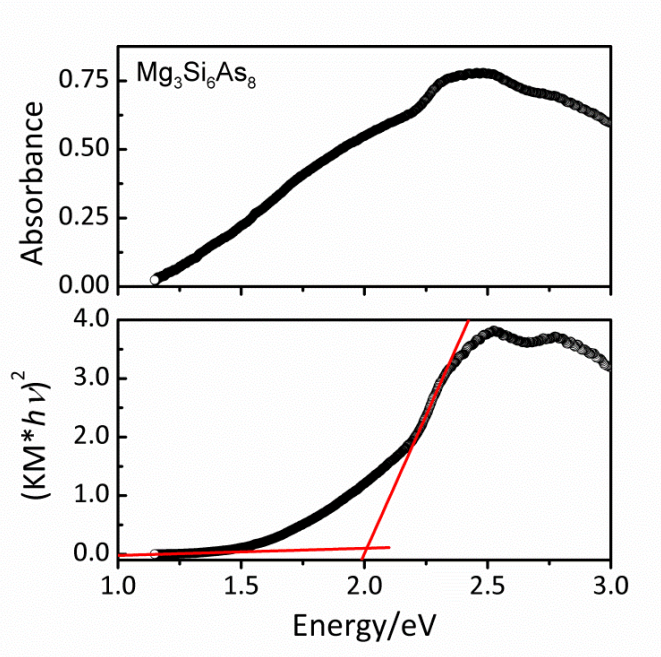

Figure 2.12 *Absorbance spectrum (top) and direct band gap Tauc plot (bottom) of $Mg_3Si_6As_8$ measured with a BLACK-Comet C-SR-100 spectrometer.*

2.4.6 Second Harmonic Generation and Laser Damage Threshold

By means of the Kurtz and Perry method, a strong powder SHG response from $MgSiAs_2$ was detected on the level of 0.6 times that of benchmark IR-SHG material, $AgGaS_2$ (Figure 2.13) under a 2.09 μm primary source. Note that the $MgSiAs_2$ powder SHG response may be seriously weakened by its narrow optical bandgap (1.83 eV) and long shortwave absorption edge (up to 1 μm). We believe that the precise SHG effect may be obtained by a long wavelength laser (e.g., carbon dioxide laser) for $MgSiAs_2$ similar to how $CdGeAs_2$ exhibits large NLO efficiency (236 pm V^{-1}) when exposed to a longer excitation wavelength (>2.5 μm) [28]. Thus, we consider $MgSiAs_2$ to be a promising IR-NLO material given a suitable pump source.

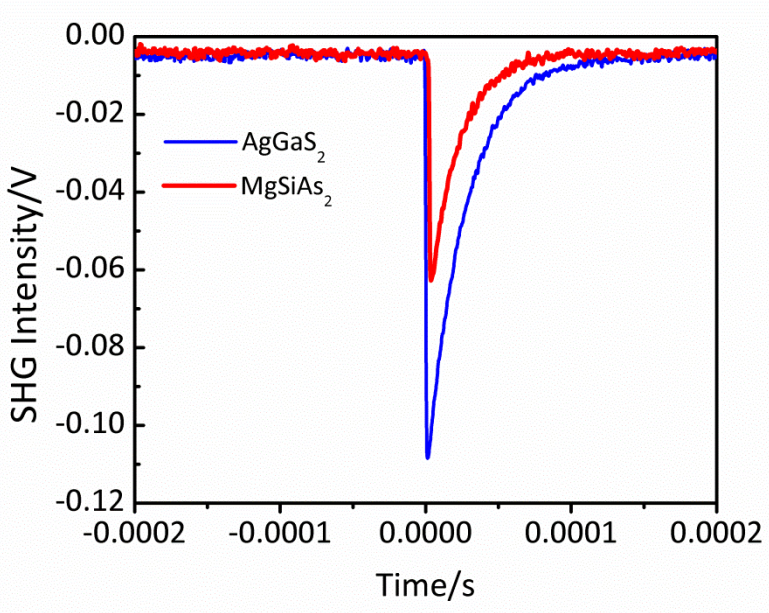

Figure 2.13 *Comparison of SHG intensity of $MgSiAs_2$ and $AgGaS_2$ at 55–88 μm particle size.*

The LDT of $MgSiAs_2$ was evaluated by adjusting the laser output energy and looking for color change using an optical microscope. Results show that $MgSiAs_2$ exhibits comparable LDT (33.2 MW cm^{-2}) with that of $AgGaS_2$ (29.6 MW cm^{-2}) (Table 2.5) as well as those of other typical IR-NLO crystals, such as $AgGaSe_2$ or $ZnGeP_2$. In order to further evaluate the application prospect for $MgSiAs_2$, a growth of large single crystal and properties evaluations at different excitation wavelength are underway.

Table 2.5 *LDTs of $MgSiAs_2$ and $AgGaS_2$ (as the reference)*

Compound	**Damage Energy (mJ)**	**Spot Diameter (mm)**	**LDT (MW/cm^2)**
$AgGaS_2$	0.58	0.5	29.6
$MgSiAs_2$	0.65	0.5	33.2

Ground crystals of $Mg_3Si_6As_8$ were also measured, but no SHG signal was detected as expected for the compound crystallizing in the 432 crystal class. This crystal class exhibits

optical activity, but it is the only non-centrosymmetric crystal class that does not exhibit SHG [29]. Trace Bi may have remained on the surface of the crystals despite multiple acid etches, but its presence is not expected to alter the results.

2.5 Conclusion

As an unexplored ternary system, Mg-Si-As exhibits a high tendency of forming NCS crystal structures, which is interesting for crystallographic study and NLO applications. $MgSiAs_2$ belongs to the well-known II-IV-VI_2 NLO structure type, while $Mg_3Si_6As_8$ crystallizes in a new non-centrosymmetric crystal structure type. Computational and optical investigations revealed direct bandgap semiconductor properties for $MgSiAs_2$, 1.83(5) eV, and $Mg_3Si_6As_8$, 2.02(8) eV. Notably, $MgSiAs_2$ presents a good balance between the SHG coefficient and laser damage threshold. While $Mg_3Si_6As_8$ does not show nonlinear optical activity, as expected due to its 432 Laue class, $MgSiAs_2$ exhibits a strong SHG response that is 0.6 times that of state-of-the-art $AgGaS_2$. $MgSiAs_2$ also exhibits a higher LDT compared to that of $AgGaS_2$, 33.2 MW cm^{-2} versus 29.6 MW cm^{-2}. Single crystal growth is important for further evaluation of its NLO application and is an undergoing study. We have also engaged in efforts to increase the bandgap of the Mg-Si-As system, such as replacing Mg with more electropositive cations, to create novel NCS compounds. Although $Mg_3Si_6As_8$ cannot be used for second harmonic generation devices, electronic structure calculations indicate it may become a viable thermoelectric material upon p-type doping.

2.6 Acknowledgements

K.E.W. and J.W. contributed equally to this work. The authors thank Dr. Frank Osterloh (UC Davis) for access to the solid-state UV–vis spectrometer, Dr. Wenqian Xu and Dr. Andrey Yakovenko (APS ANL) for assistance in synchrotron data collections, Bryan Rosales and Dr. Javier Vela (Iowa State University) for access to and assistance on using

their UV–vis spectrometer, and Dr. Weiguo Zhang and Dr. Shiv Halasyamani (University of Houston) for preliminary SHG measurements of $Mg_3Si_6As_8$. This research was supported by the ACS Petroleum Research Fund, Grant No. 55036-DNI10. Use of the Advanced Photon Source at Argonne National Laboratory was supported by the U.S. Department of Energy, Office of Science, Office of Basic Energy Sciences, under Contract No. DE-AC02-06CH11357.

2.7 References

[1] a) D. Cyranoski, *Nature* **2009**, *457*, 953; b) P. Becker, *Adv. Mater.* **1998**, *10*, 979; c) H.-Y. Chang, S.-H. Kim, P. S. Halasyamani, K. M. Ok, *J. Am. Chem. Soc.* **2009**, *131*, 2426; d) M. D. Donakowski, R. Gautier, J. Yeon, D. T. Moore, J. C. Nino, P. S. Halasyamani, K. R. Poeppelmeier, *J. Am. Chem. Soc.* **2012**, *134*, 7679; e) S. Y. Song, D. W. Lee, K. M. Ok, *Inorg. Chem.* **2014**, *53*, 7040; f) S. Wang, N. Ye, W. Li, D. Zhao, *J. Am. Chem. Soc.* **2010**, *132*, 8779; g) H. Huppertz, B. von der Eltz, *J. Am. Chem. Soc.* **2002**, *124*, 9376; h) S. Zhao, P. Gong, L. Bai, X. Xu, S. Zhang, Z. Sun, Z. Lin, Z. Hong, C. Chen, J. Luo, *Nat. Commun.* **2014**, *5*, 4019; i) P. Yu, L.-M. Wu, L.-J. Zhou, L. Chen, *J. Am. Chem. Soc.* **2014**, *136*, 480; j) X. Xu, C.-L. Hu, B.-X. Li, B.-P. Yang, J.-G. Mao, *Chem. Mater.* **2014**, *26*, 3219; k) T. K. Bera, J-H. Song, A. J. Freeman, J. I. Jang, J. B. Ketterson, M. G. Kanatzidis, *Angew. Chem.* **2008**, *120*, 7946; *Angew. Chem. Int. Ed.* **2008**, *47*, 7828; l) L. Li, G. Li, Y. Wang, F. Liao, J. Lin, *Chem. Mater.* **2005**, *17*, 4174.

[2] a) V. A. Serebryakov, É. V. Boĭko, N. N. Petrishchev, A. V. Yan, *J. Opt. Technol.* **2010**, *77*; b) P. F. Bordui, M. M. Fejer, *Annu. Rev. Mater. Sci.* **1993**, *23*, 321; c) M. B. Pushkarsky, M. E. Webber, T. Macdonald, C. K. N. Patel, *Appl. Phys. Lett.* **2006**, *88*, 044103; d) J. Zhou, J.-W. Zhao, Q. Wei, J. Zhang, G.-Y. Yang, *J. Amer. Chem. Soc.* **2014**, *136*, 5065; e) L. Geng, W.-D. Cheng, C.-S. Lin, W.-L. Zhang, H. Zhang, Z.-Z. H, *Inorg. Chem.* **2011**, *50*, 5679; f) X.-M. Jiang, M.-J. Zhang, H.-Y. Zeng, G.-C. Guo, J.-S. Huang, *J. Amer. Chem. Soc.* **2011**, *133*, 3410; g) P. Yu, L.-J. Zhou, L. Chen, *J. Am. Chem. Soc.* **2012**, *134*, 2227; h) W. Zhang, P. S. Halasyamani, *Cryst. Growth Des.* **2011**, *11*, 3636.

[3] a) R. S. Feigelson, R. K. Route, *Opt. Eng.* **1987**, *26*, 262113; b) H. Kildal, J. C. Mikkelsen, *Opt. Commun.* **1973**, *9*, 315; c) V. G. Dmitriev, G. G. Gurzadyan, D. N. Nikogosyan, *Handbook of Nonlinear Optical Crystals, 3rd ed.*, Springer, New York, NY, USA **1999**; d) A. G. Jackson, M. C. Ohmer, S. R. LeClair, *Infrared Phys. Technol.* **1997**, *38*, 233.

[4] a) G. D. Boyd, E. Buehler, *Appl. Phys. Lett.* **1971**, *18*, 301; b) G. Zhang, X. Tao, S. Wang, Q. Shi, H. Ruan, L. Chen, *J. Cryst. Growth* **2012**, *352*, 67.

[5] a) H. Zhang, M. Zhang, S. Pan, X. Dong, Z. Yang, X. Hou, Z. Wang, K. B. Chang, K. R. Poeppelmeier, *J. Amer. Chem. Soc.* **2015**, *137*, 8360; b) L. Kang, M. Zhou, J. Yao, Z. Lin, Y.

Wu, C. Chen, *J. Amer. Chem. Soc.* **2015**, *137*, 13049.

[6] a) A. J. Springthorpe, J. G. Harrison, *Nature* **1969**, *222*, 977; b) H. Pfister, *Acta Crystallogr.* **1958**, *11*, 221; c) H. Hahn, G. Frank, W. Klinger, A. D. Meyer, G. Stoerger, *Z. Anorg. Allg. Chem.* **1953**, *271*, 153.

[7] a) S. C. Abrahams, J. L. Bernstein, *J. Chem. Phys.* **1970**, *52*, 5607; b) S. C. Abrahams, J. L. Bernstein, *J. Chem. Phys.* **1971**, *55*, 796.

[8] a) V. L. Shaposhnikov, A. V. Krivosheeva, V. E. Borisenko, J.-L. Lazzari, F. Arnaud d'Avitaya, *Phys. Rev. B* **2012**, *85*, 205201; b) A. D. Martinez, A. N. Fioretti, E. S. Toberer, A. C. Tamboli, *J. Mater. Chem. A*, **2017**, *5*, 11418; c) V. S. Bhadram, L. Krishna, E. S. Toberer, R. Hrubiak, E. Greenberg, V. B. Prakapenka, T. A. Strobel, *Appl. Phys. Lett.* **2017**, *110*, 182106; d) A. D. Martinez, E. L. Warren, P. Gorai, K. A. Borup, D. Kuciauskas, P. C. Dippo, B. R. Ortiz, R. T. Macaluso, S. D. Nguyen, A. L. Greenaway, S. W. Boettcher, A. G. Norman, V. Stevanović, E. S. Toberer, A. C. Tamboli, *Energy Environ. Sci.* **2016**, *9*, 1031; e) J. L. Shay, J. H. Wernick, *Ternary Chalcopyrite Semiconductors: Growth, Electronic Properties, and Applications*, Pergamon Press, Elmsford, New York, USA **1975**.

[9] a) L. Shi, J. Hu, Y. Qin, Y. Duan, L. Wu, X. Yang, G. Tang, *J. Alloys Compd.* **2014**, *611*, 210; b) F. Chiker, Z. Kebbab, R. Miloua, N. Benramdane, *Solid State Commun.* **2011**, *151*, 1568; c) B. Kocak, Y. O. Ciftci, G. Surucu, *J. Electron. Mater.* **2017**, *46*, 247; d) V. Kumar, S. K. Tripathy, V. Jha, B. P. Singh, *Phys. Lett. A* **2014**, *378*, 519; e) F. Boukabrine, F. Chiker, R. Miloua, Z. Kebbab, R. Khenata, D. Prakash, S. Bin Omran, K. D. Verma, *Opt. Mater.* **2016**, *54*, 200; f) V. Kumar, A. Sinha, B. P. Singh, A. P. Sinha, V. Jha, *Chin. Phys. Lett.* **2015**, *32*, 127701; g) M. Ibrahim, H. Ullah, S. U. Jan, M. Ali, M. G. Ashiq, *Surf. Rev. Lett.* **2018**, *25*, 1850108.

[10] B. H. Toby, R. B. Von Dreele, *J. Appl. Crystallogr.* **2013**, *46*, 544.

[11] Bruker (2008). *APEX2, APEX3*. Bruker AXS Inc., Madison, Wisconsin, USA.

[12] G. M. Sheldrick, *Acta Crystallogr., Sect. C: Struct. Chem.* **2015**, *71*, 3.

[13] K. Momma, F. Izumi, *J. Appl Crystallogr.* **2011**, *44*, 1272.

[14] O. Jepsen, O. K. Andersen. *The Stuttgart TB-LMTO program.* (2000). Stuttgart, Germany: Max-Planck- Institut für Festkörperforschung.

[15] U. von Barth, L. Hedin, *J. Phys. C: Solid State Phys.* **1972**, *5*, 1629.

[16] S. K. Kurtz, T. T. Perry, *J. Appl. Phys.* **1968**, *39*, 3798.

[17] J. Dolyniuk, J. V. Zaikina, D. C. Kaseman, S. Sen, K. Kovnir, *Angew. Chem.* **2017**, *129*, 2458; *Angew. Chem. Int. Ed.* **2017**, *56*, 2418.

[18] J. Wang, J. T. Greenfield, K. Kovnir, *Inorg. Chem.* **2017**, *56*, 8348.

[19] E. Zintl, E. Husemann, *Z. Phys. Chem. B* **1933**, *21*, 138.

[20] R. Gerardin, J. Aubry, *Acta Crystallogr. B* **1977**, *33*, 2091.

[21] R. Vogel, H. U. Schuster, *Z. Naturforsch., B* **1979**, *34*, 1719.

[22] A. Wurth, A. Loehken, A. Mewis, *Z. Anorg. Allg. Chem.* **2001**, *627*, 1213.

[23] J. Wang, L.-L. Wang, K. Kovnir, *J. Mater. Chem. A* **2018**, *6*, 4759.

[24] B. G. de Boer, A. Zalkin, D. H. Templeton, *Inorg. Chem.* **1969**, *8*, 836.

[25] T. K. Chattopadhyay, W. May, H. G. von Schnering, G. S. Pawley, *Z. Kristallogr.* **1983**, *165*, 47.

[26] a) Y. Hu, J. Wang, A. Kawamura, K. Kovnir, S. M. Kauzlarich, *Chem. Mater.* **2015**, *27*, 343; b) J. Wang, K. Lee, K. Kovnir, *J. Mater. Chem. C* **2015**, *3*, 9811; c) J. Wang, K. Kovnir, *J. Amer. Chem. Soc.* **2015**, *137*, 12474.

[27] a) R. Dronskowski, P. E. Bloechl, *J. Phys. Chem.* **1993**, *97*, 8617; b) R. Dronskowski, *Computational Chemistry of Solid State Materials: A Guide for Materials Scientists, Chemists, Physicists and Others*, Wiley-VCH, Weinheim, Germany **2005**.

[28] R.L. Byer, H. Kildal, *Appl. Phys. Lett.* **1971**, *19*, 237.

[29] a) P. S. Halasyamani, K. R. Poeppelmeier, *Chem. Mater.* **1998**, *10*, 2753; b) A. M. Glazer, K. Stadnicka, *Acta Crystallogr. A* **1989**, *45*, 234; c) J. F. Nye, *Physical Properties of Crystals*, Oxford University Press, Oxford, UK **1957**; d) J. A. Armstrong, N. Bloembergen, J. Ducuing, P. S. Pershan, *Phys. Rev.* **1962**, *127*, 1918.

CHAPTER 3. SUPERSEDING VAN DER WAALS WITH ELECTROSTATIC INTERACTIONS: INTERCALACTION OF Cs INTO THE INTERLAYER SPACE OF $SiAs_2$

The contents of this chapter have been modified from the manuscript Woo, K. E.; Dolyniuk, J.-A..; Kovnir, K. Superseding Van der Waals with Electrostatic Interactions: Intercalation of Cs Into the Interlayer Space of $SiAs_2$. (Unpublished)

3.1 Introduction

In the past twenty years, there has been increased interest in low dimensional materials. Graphene, which was first isolated in 2004 by Novoselov et al., has been found to have many unique properties such as optical absorption, high tensile strength and rigidity, anisotropic thermal conductivity, and high intrinsic electron mobility [1]. The characterization of this compound inspired further development and research of more 2D materials. A few examples of these compounds include h-BN, black phosphorus, transition metal dichalcogenides, Xenes, MXenes, and FeSe, which cover a broad spectrum of interesting properties related to magnetism, conductivity (from insulators to superconductors), carrier mobility, and more [2].

One of the intriguing aspects of 2D materials is their intrinsic low thermal conductivity, which has been attributed to the record high thermoelectric figure of merit of SnSe [3]. The addition of cations between the layers is expected to increase the anharmonicity found in these 2D structures, thus contributing to an even lower thermal conductivity than the base framework, similar to how the lattice thermal conductivity of the filled skutterudite, $CeFe_4Sb_{12}$, is almost a full magnitude lower than that of the unfilled skutterudite, $CoSb_3$ [4]. With 2D materials, electrical conductivity is expected to be preserved due to the covalent bonding within the layers, therefore having the material act like

a Phonon Glass-Electron Crystal [5]. This has been demonstrated on the example of layered $NaCo_2O_4$, which exhibited a low thermal conductivity while its electrical resistivity displayed metallic behavior [6].

Our group has been working on binary 2D tetrel pnictides {Si,Ge}-{P,As}, where the repulsion of the electron lone pair located on the pnicogen atoms generates layered structures [7]. Strongly anisotropic and fascinating properties were predicted computationally for this class of materials and their individual layers [8]. Experimentally, anisotropic transport properties have been demonstrated for GeAs [9]. In the current work we explored how tetrel pnictides may accommodate the alkali cation, Cs, in the interlayer space. We have synthesized a new family of compounds with Cs cations situated between $M_xSi_{1-x}As_2$ (M = Cu, Zn, Ga) layers, which are isostructural to $SiAs_2$ layers. The substituting metal works in tandem with the intercalated Cs cations to electron balance the compound. We report in this paper on the synthesis, structure, and properties of $Cs_{0.16}M_xSi_{1-x}As_2$ (M = Cu, Zn, Ga).

3.2 Experimental

3.2.1 Synthesis

Magnesium turnings (Alfa Aesar, 99.98%), silicon powder (Alfa Aesar, 99.99%), polycrystalline arsenic lump (Alfa Aesar, 99.99999+%), copper powder (Alfa Aesar, 99.9%), zinc granules (Alfa Aesar, 99.8%), gallium ingots (Alfa Aesar, 99.9999%), and cesium chloride (Sigma Aldrich, 99.99%) were all used as received.

Single crystals were synthesized by loading stoichiometric ratios of Si, As, and *M* (*M* = Cu, Zn, Ga) when necessary, with 0.5 molar Mg and 1.2-2 molar CsCl flux in a silica ampoule, assuming final compositions of $Cs_{0.16}SiAs_{1.95}$, $Cs_{0.16}Cu_{0.06}Si_{0.94}As_2$, $Cs_{0.16}Zn_{0.08}Si_{0.92}As_2$, and $Cs_{0.16}Ga_{0.16}Si_{0.84}As_2$. The ampoules were evacuated (~10^{-2} mbar) and flame sealed with a hydrogen-oxygen torch. The ampoules were then heated up to 1123

K over 17 h and annealed for 144 h. Once opened to air, the products were washed for 15-20 min in water and then filtered using a glass Buchner funnel with a coarse frit. The target phase crystallized as thin silver needles. Samples were stored in an argon-filled glovebox.

Almost pure-phase samples for the Zn and Ga variants were synthesized using a similar method as described above. To minimize Mg_2SiO_4 as a side phase, the ampoule was carefully broken at the site of the product to recover the middle part of the sample and to discard the ingot surface where Mg and the silica ampoule had reacted. Using tweezers to manipulate the sample, the ingot was soaked in water while being gently tapped against the side of the beaker to remove the brown Mg_2SiO_4 shell. Once the shell was removed, the chunk was placed in clean water to dissolve any remaining CsCl. After filtering and drying, the products were ground using an agate mortar and pestle, and fresh CsCl and Mg of the original amounts were added. The sample was annealed a total of three times using the same heating profile and with washing and grinding in between.

3.2.2 Powder and Single Crystal X-Ray Diffraction (XRD)

Powder XRD experiments were done using a Rigaku 600 Miniflex diffractometer using Cu-K_α radiation and a Ni-K_β filter. Data for single crystals of $Cs_{0.16}M_xSi_{1-x}As_2$ (M = Cu, Zn, Ga) and $Cs_{0.15}SiAs_{1.97}$ were collected on a Bruker AXS SMART diffractometer with Mo-K_α radiation and an APEX-II CCD area detector. The data sets were collected at 90 K in a nitrogen gas atmosphere. The Bruker SAINT software was used to integrate the raw data, and multiscan absorption corrections were applied. Crystal structure solution and refinement was performed using the SHELX suite [10]. Data collection and unit cell parameters are summarized in Table 3.1. Upon solving the Zn-containing structure, the positions of Si and As atoms were located by direct methods. Further refinement revealed two electron density

peaks in the interlayer space with very high interatomic distances >3 Å to neighboring As atoms. Those peaks were refined as Cs, which resulted in enormously high atomic displacement parameters (ADPs). The occupancy of Cs sites was refined, which resulted in reasonable ADPs. Further analysis of the obtained model revealed that Si positions have significantly smaller ADPs as compared to As sites, and those positions were refined as mixed occupancies by Si and Zn with constrains of 100% total occupancy, identical positions, and equal ADPs, resulting in the final structural model reported here. This resulted in a significant decrease of the R-values. In the final refinement, all framework atoms were refined anisotropically, while Cs atoms were kept isotropic due to the disordered nature of Cs sites. Solutions of Cu- and Ga-containing structures were performed in an analogous manner. For the structure with low Ga content, one As position had an unusually high ADP. The occupancy of this site was refined and resulted in the meaningful occupancy of 0.953(6)%. During the refinement of the crystal structure of the ternary Cs-Si-As compound, both Si sites and two out of four As sites had similar ADPs, while two other As sites had significantly higher ADPs. The occupancy for those two As sites was refined resulting in 0.931(3)% and 0.968(3)% occupancies and a drop in the R-values. Additionally, this crystal structure is best described with three partially occupied Cs positions instead of two. The third Cs position has unreasonable short distance to one of partially occupied As atoms, but the occupancy of this Cs site, 2.1(1)%, is lower than to the As position vacancies concentration, 3.2(3)%. Crystal structure images were generated using VESTA [11]. Further details of the crystal structure investigations given in Table 3.1 may be obtained from the Fachinformationszentrum Karlsruhe, 76344 Eggenstein-Leopoldshafen (Germany), on quoting the depository numbers CSD-434632, CSD-434633, CSD-434634, CSD-434635, and

CSD-434636. In addition, the data were deposited to The Cambridge Crystallographic Data Centre, CCDC Nos. 1846410-1846414.

3.2.3 In Situ Powder Synchrotron XRD

Slices of Mg was cut from a piece of Mg turning and pushed to the bottom of silica capillaries (0.5 mm ID × 0.7 mm OD, Friedrich & Dimmock, Inc.). About 10 mg of finely ground and homogenous mixtures of 0.6 Cu:0.94 Si, 0.1 Zn:0.9 Si, and 0.2 Ga:0.8 Si with 1.5 CsCl and 2 As molar ratios each were then added. The capillaries were evacuated and flame sealed. Beamline 17-BM-B at the Advanced Photon Source at Argonne National Lab was used. The sample was loaded onto a flow cell equipped with electric heaters and exposed to synchrotron radiation (λ = 0.45336 Å). Data was collected as the samples were heated at 15 K/min until 1123 K, dwelled for 15-20 min at that temperature, and then cooled at 15-50 K/min to 300-325 K. Analysis of data was performed using GSAS-II [12].

3.2.4 Scanning Electron Microscopy (SEM) and Energy Dispersive X-Ray Spectroscopy (EDS)

Elemental compositions for $Cs_{0.16}M_xSi_{1-x}As_2$ (M = Cu, Zn) was analyzed using a Hitachi S4100T SEM with Oxford INCA energy dispersive X-ray spectroscopy (EDS). $Cs_{0.16}Ga_{0.16}Si_{0.84}As_2$, $Cs_{0.16}SiAs_{1.97}$, and $Cs_{0.11}Zn_{0.05}Si_{0.95}As$ were measured with an FEI Quanta 250 FE-SEM equipped with an Oxfords X-Max 80 detector. As preparation, single crystals of $Cs_{0.16}M_xSi_{1-x}As_2$ (M = Cu, Zn) and $Cs_{0.11}Zn_{0.05}Si_{0.95}As$ were applied to carbon tape. Single crystals of $Cs_{0.16}Ga_{0.16}Si_{0.84}As_2$ and $Cs_{0.16}SiAs_{1.97}$ were placed in graphite dies, which were filled with a two part epoxy and then polished until smooth. The puck was then coated with conductive carbon.

Table 3.1 *Data collection and unit cell parameters*

Composition	$Cs_{0.148(2)}Si_1As_{1.950(2)}$	$Cs_{0.170(4)}Cu_{0.058(4)}Si_{0.943}As_2$	$Cs_{0.164(3)}Zn_{0.080(3)}Si_{0.920}As_2$	$Cs_{0.149(5)}Ga_{0.103(5)}Si_{0.898}As_{1.977(3)}$	$Cs_{0.19(1)}Ga_{0.201(8)}Si_{0.80}As_2$
Formula weight (g/mol)	194.63	202.82	202.17	200.19	211.23
Temperature (K)	90(2)				
Radiation, λ	Mo-K$_a$, 0.71073 Å				
Crystal system	Orthorhombic				
Space group	*Pnma* (No. 62)				
***a* (Å)**	10.310(1)	10.277(2)	10.308(2)	10.324(2)	10.293(3)
***b* (Å)**	3.6597(4)	3.6461(8)	3.6607(7)	3.6638(8)	3.662(1)
***c* (Å)**	16.602(2)	16.771(4)	16.756(3)	16.682(4)	16.715(6)
***V* (Å^3)**	626.4(1)	628.5(2)	632.3(2)	631.0(2)	629.9(4)
Z	8				
ρ_{calc} (g cm^{-3})	4.13	4.29	4.25	4.21	4.45
μ (mm^{-1})	22.68	23.65	23.58	23.50	25.02
Data/param.	1200/52	951/49	956/48	840/49	648/48
R_1	0.023	0.036	0.030	0.042	0.049
wR_2	0.046	0.059	0.068	0.116	0.124
Goodness-of-fit	1.11	1.08	1.12	1.08	1.14
Diff. peak/hole (e/Å^3)	1.90/-0.85	1.16/-1.23	1.14/-1.02	1.98/-1.71	2.26/-1.73

3.2.5 Differential Scanning Calorimetry (DSC)

DSC measurement was executed on a sample of $Cs_{0.16}Zn_{0.08}Si_{0.92}As_2$ (10 mg) using a Netzsch STA 449 F3 Jupiter Differential Scanning Calorimeter. Finely ground powder was sealed in an evacuated silica ampoule, which was then heated to 1273 K and cooled to 323 K at a rate of 5 K min^{-1}.

3.2.6 Sintering

Pellets were made by loading 84 mg of finely ground powder of almost phase-pure $Cs_{0.16}Ga_{0.16}Si_{0.84}As_2$ into a graphite die (5 mm ID × 20 mm OD) with 5 mm diameter WC plungers that was then encased by an outer graphite die (20 mm ID × 47 mm OD) and 20 mm diameter graphite plungers. 76 MPa of pressure was applied at room temperature under vacuum using a spark plasma sintering machine. After holding for 10 min, pressure was instantly released. A geometric density of 50.7% compared to calculated X-ray densities was achieved.

3.2.7 Transport Properties

Transport properties were characterized using the commercial Physical Properties Measurement System (PPMS, Quantum Design). Temperature dependencies of electrical resistivity were measured on single crystals of $Cs_{0.16}M_xSi_{1-x}As_2$ (M = Cu, Zn, Ga) by a 4-point *ac* technique to exclude resistance of the leads. Temperature dependencies of thermal conductivity were measured on a $Cs_{0.16}Ga_{0.16}Si_{0.84}As_2$ pellet using the Thermal Transport Option.

3.3 Results and Discussion

Individual Cu-, Zn-, and Ga-containing compounds will be referred to by their nominal compositions.

3.3.1 Synthesis

Using CsCl as a cesium source eliminates many difficulties associated with handling Cs metal, such as high cost, necessity to work in an inert environment, and high reactivity of Cs towards the ampoule or crucible materials such as silica, carbon, or alumina. In our reactions, Cs was generated in situ due to the reaction of Mg with the CsCl melt. $MgCl_2$ and CsCl by-products were removed by water wash. Powder XRD was used to characterize the products, and side products such as SiAs were commonly observed. Due to reaction with the silica vessel, Mg_2SiO_4 was sometimes detected mainly at the outer part of the reaction ingot. Mechanical separation aided in minimizing Mg_2SiO_4 as a side product. Carbonizing the ampoule did not help with preventing the formation of Mg_2SiO_4 or with overall purification. While almost-pure phase samples of the Zn and Ga compounds could be attained when using a repeated grinding-annealing method, SiAs remained as a prominent side product in all synthesis variations for the Cu compound. Varying *M*:Si starting ratios also did not result in pure phase products.

Due to difficulties in purification of the samples, the reactions were monitored by in situ powder X-ray diffraction experiments. All starting materials except a trace of Si went into a melt around 873 K for the Cu compound, 993 K for the Zn compound, and 913 K for the Ga compound. During cooling, $Cs_{0.16}Cu_{0.06}Si_{0.94}As_2$ began to crystallize at around 1081 K, $Cs_{0.16}Zn_{0.08}Si_{0.92}As_2$ at 1058 K, and $Cs_{0.16}Ga_{0.16}Si_{0.84}As_2$ at 1033 K. Based on this data, a new heating profile was assessed, in which the reaction was quenched in ice water after holding at 1123 K for 48 h. While the target compounds were detected from powder XRD, side phases such as SiAs were still prominent in the samples. A similar reaction was also performed in which the Cu compound was cooled to 973 K in three hours before quenching, but the results were the same as when quenching at 1123 K.

Regardless of the aforementioned purification complications, $Cs_{0.16}M_xSi_{1-x}As_2$ crystals are easily synthesized in all studied samples, including those without the loading of elemental Si. In fact, $Cs_{0.16}M_xSi_{1-x}As_2$ was detected when only the silica ampoule was provided as the source of Si, though various side phases remained present.

Table 3.2 *Data collection and unit cell parameters of* $Cs_{0.11}Zn_{0.05}Si_{0.95}As$

Composition	**$Cs_{0.11}Zn_{0.05}Si_{0.95}As$**
Formula weight (g/mol)	119.39
Temperature (K)	100(2)
Radiation, λ	Mo-K$_\alpha$, 0.71073 Å
Crystal system	Monoclinic
Space group	*C*2/*m* (No. 12)
***a* (Å)**	35.201(3)
***b* (Å)**	3.6649(3)
***c* (Å)**	9.9848(9)
β (°)	91.863(2)
***V* (Å^3)**	1287.4(2)
Z	24
ρ_{calc} (g cm^{-3})	3.696
μ (mm^{-1})	18.24
Data/param.	1947/85
R_1	0.0392
wR_2	0.0627
Goodness-of-fit	1.11
Diff. peak/hole (e/Å^3)	1.77/-1.87

The synthesis of $Cs_{0.16}Zn_{0.08}Si_{0.92}As_2$ with Cs metal (Alfa Aesar, 99.8%) was attempted by loading stoichiometric ratios of the starting elements in a Nb ampoule that was arc welded shut. The Nb ampoule was then sealed in an evacuated secondary silica jacket to prevent oxidation of the vessel. The same heating profile identical to that described in the experimental section for single crystal growth was used. This method of synthesis proved to be less successful as the main products turned out to be Nb_3As and $ZnSiAs_2$, together with

traces of another quaternary Cs-Zn-Si-As compound, $Cs_{0.11}Zn_{0.05}Si_{0.95}As$, instead of the target $Cs_{0.16}Zn_{0.08}Si_{0.92}As_2$ phase. This new phase also synthesizes as black needles. Further crystallographic data can be found in Table 3.2.

3.3.2 Crystal Structure

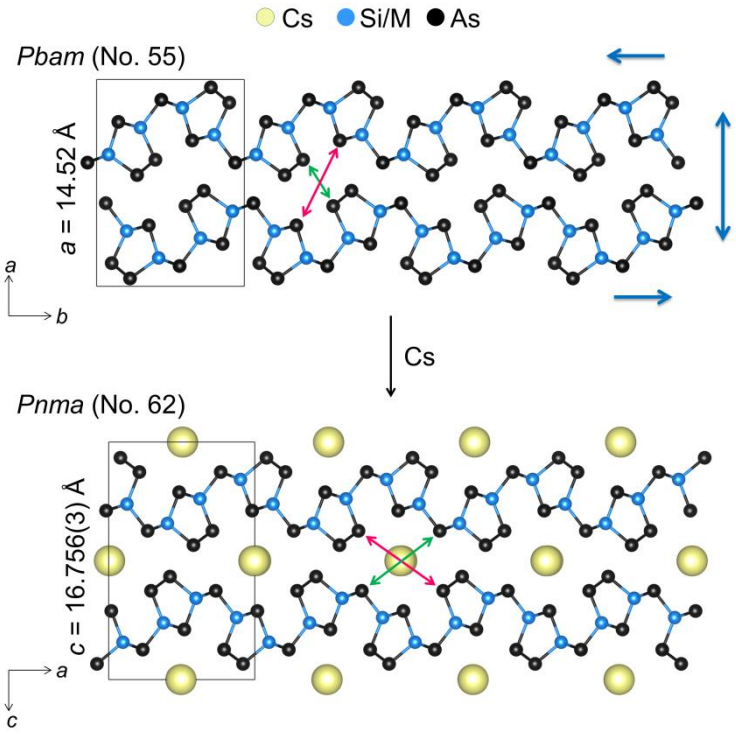

Figure 3.1 *Projection of crystal structure of $SiAs_2$ (top) and its rearrangement into $Cs_{0.16}Zn_{0.08}Si_{0.92}As_2$ (bottom) through translational motion, as depicted by the blue arrows. Cs: yellow; Si and Zn: blue, As: black. Unit cells are shown as gray rectangles.*

$Cs_{0.16}M_xSi_{1-x}As_2$ (M = Cu, Zn, Ga) is composed of $SiAs_2$ layers with Cs atoms interspersed between. Each individual layer is similar to that found in binary $SiAs_2$ [13]. Each layer consists of Si coordinated to four As atoms and As either coordinated to three other Si atoms or two As and one Si atom. Minimal distortions in bond angles occur from the transition of the $SiAs_2$ crystal structure to $Cs_{0.16}M_xSi_{1-x}As_2$. The channels in which Cs atoms reside can be made with simple translational movement of the Si-As layers (as indicated by the blue arrows in Figure 3.1), causing the unit cell parameter perpendicular to the layers to

increase from 14.52 Å in $SiAs_2$ to 16.756(3) Å in the Zn-containing compound. The lattice parameters parallel to the layers are largely unchanged with b = 10.37 Å and c = 3.636 Å in $SiAs_2$ and a = 10.308(2) Å and b = 3.6607(7) Å in $Cs_{0.16}Zn_{0.08}Si_{0.92}As_2$. Sliding the $SiAs_2$ layers cause an increase in the shortest interlayer As-As distance from 3.882 Å (in $SiAs_2$) to 7.176(2) Å in the Zn-containing compound as depicted by the green arrows in Figure 3.1. The second interlayer As-As distance, given by the pink arrows in Figure 3.1, also increases from 6.692 Å to 7.548(2) Å, respectively. These As-As distances across the Cs channels in the Zn-containing compound are comparable to the As-As distances across the clathrate cages in $Cs_8Zn_{18}As_{28}$, which ranges from 6.86 Å to 7.14 Å in the smaller cage and 7.29 Å to 8.20 Å in the larger cage [14].

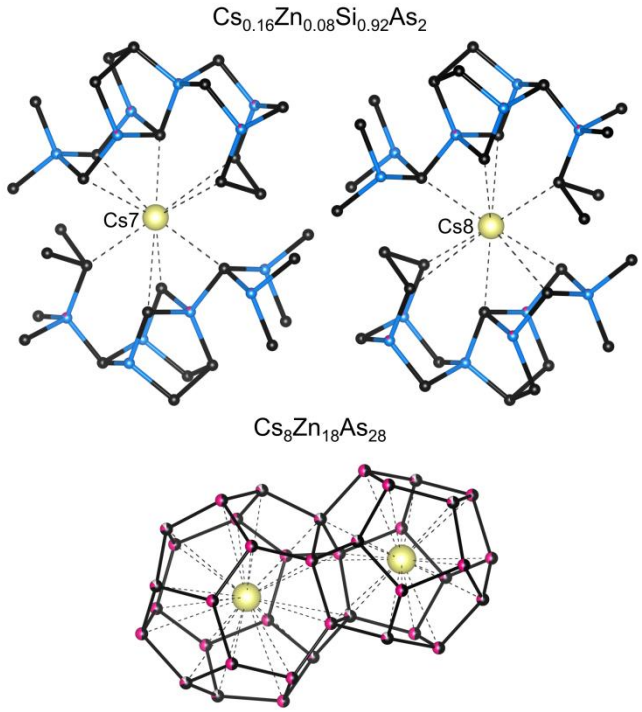

Figure 3.2 *Coordination of both Cs positions to As in $Cs_{0.16}Zn_{0.08}Si_{0.92}As_2$ (top) and $Cs_8Zn_{18}As_{28}$ (bottom). Cs: yellow, Si: blue, Zn: pink, As: black, vacancies: white. Mixed/partial site occupancies are shown as colored fractions.*

The two Cs positions in $Cs_{0.16}M_xSi_{1-x}As_2$ (M = Cu, Zn, Ga) are both coordinated to nine As atoms (Figure 3.2), though Cs7-As distances in the Zn-containing compound range from 3.529(3)-4.144(3) Å and Cs8-As distances are slightly longer at 3.549(4)-4.401(5) Å. These distances are comparable with the Cs-As distances in the large cage of the $Cs_8Zn_{18}As_{28}$ clathrate, where they range from 3.626-4.149 Å. The distances in the smaller clathrate cage (without considering the partial split As position) are shorter at 3.430 Å and 3.568 Å.

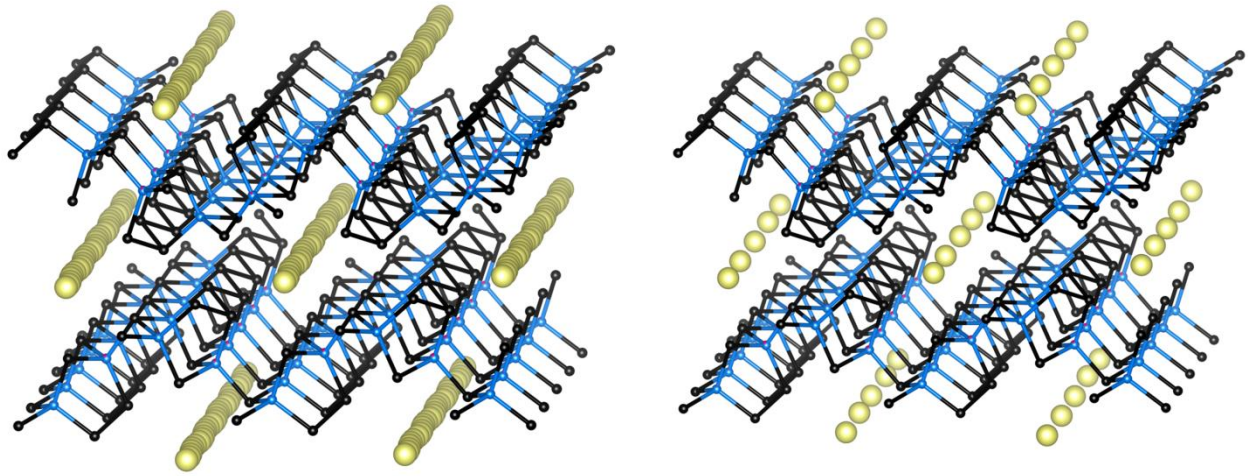

Figure 3.3 *Cs disorder between Si/Zn-As layers with all possible positions displayed (left) and potential Cs ordering (right). Cs: yellow, Si: blue, Zn: pink, As: black.*

Prominent Cs disorder is apparent from single crystal diffraction experiments, which is conducive to low thermal conductivity in the sample (Figure 3.3). There are two Cs positions with fractional occupancies of 16% and 8% in the Zn-containing compound. The shortest distances between those positions are physically impossible, ranging from 0.56 Å to 3.1 Å. The shortest reported Cs-Cs distances in ambient pressure ordered compounds are 3.24 Å in Cs_5Te_3, 3.31 Å in CsV_5S_8, and 3.36 Å in $CsCaH_3$ [15]. High-pressure modifications of elemental Cs and CsI were reported to have shorter distances in the range of 3.00-3.10 Å [16]. We assumed that in $Cs_{0.16}M_xSi_{1-x}As_2$, the Cs-Cs separations exceed 3.1 Å and instead have more reasonable distances of 3.66-4.36 Å, which was used to generate the

ordered model in Figure 3.3 right. Further local scale experimentation is required to observe trends in actual Cs-Cs distances within the compound.

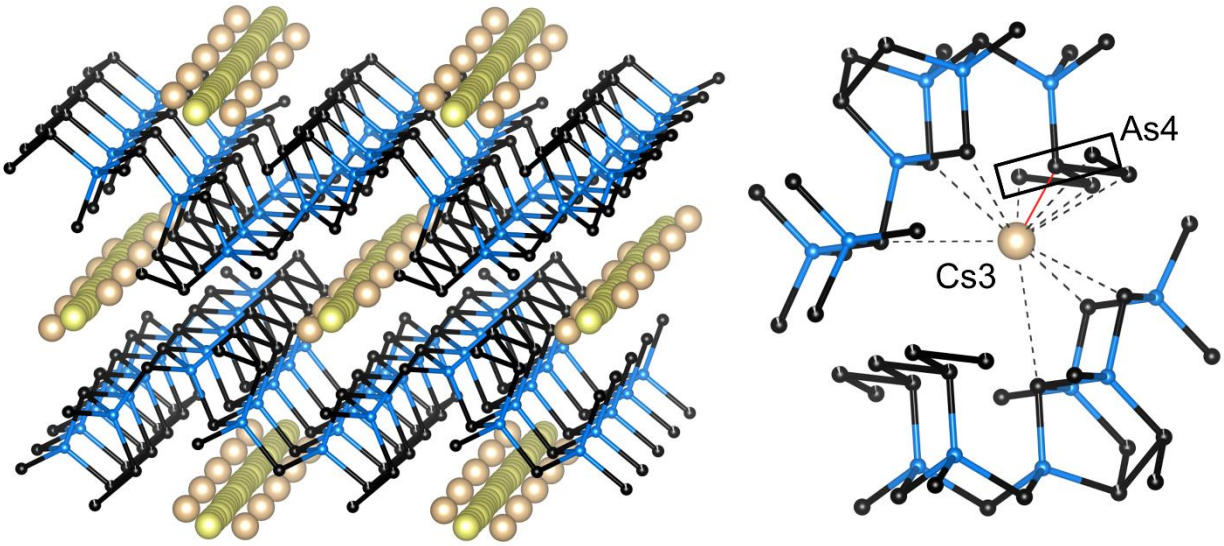

Figure 3.4 *All possible Cs positions in $Cs_{0.16}SiAs_{1.95}$ (left) and coordination of Cs3 to As (right). Cs1 and Cs2: yellow, Cs3: beige, Si: blue, As: black, vacancies: white.*

Two of the three Cs atoms in $Cs_{0.16}SiAs_{1.95}$ have similar coordination and distances to the compounds with metal substitution. The third Cs atom lays distinctly off-center within the channel (Figure 3.4). The Cs3-As4 distance of 2.49(1) Å (shown in red in Figure 3.4 right) is improbable as the shortest reported Cs-As distance is 3.073 Å in Cs_6NbAs_5 [17]. The concentration of vacancies in the As4 site exceed the occupancy of Cs3 site as described in the experimental section. It is likely that there is a vacancy in the As4 position when Cs3 is present. Assuming this vacancy, Cs3 is then coordinated to 8 As atoms with distances ranging from 3.61(1)-4.22(1) Å.

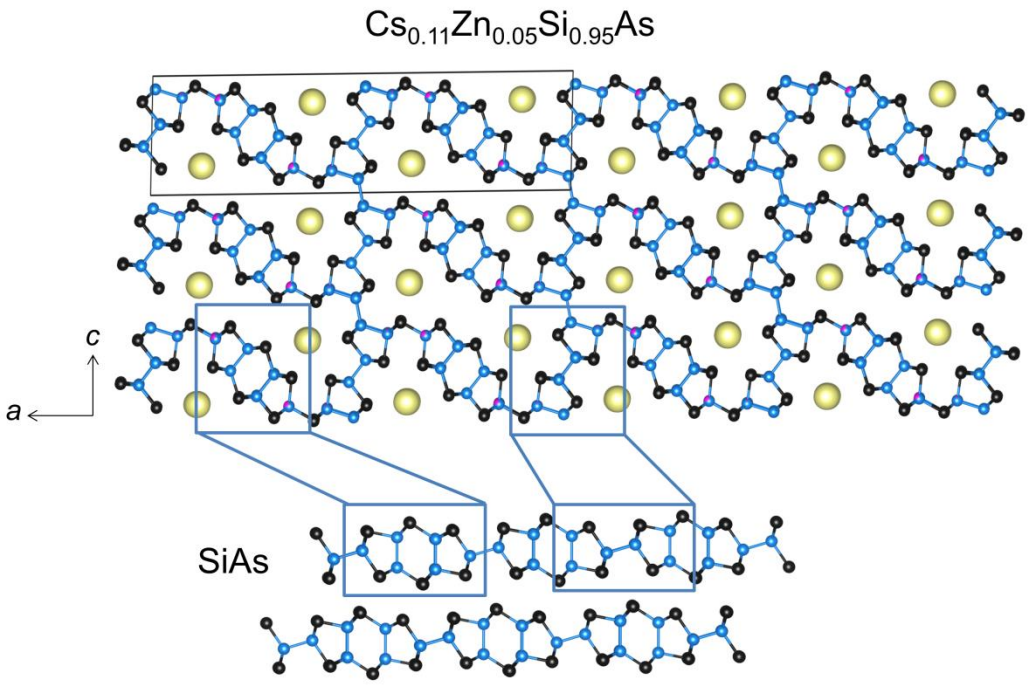

Figure 3.5 *Crystal structure of $Cs_{0.11}Zn_{0.05}Si_{0.95}As$ in comparison with SiAs. Unit cell is marked by a black box. Cs: yellow, Si: blue, Zn: pink, As: black.*

While the framework of $Cs_{0.16}M_xSi_{1-x}As_2$ (M = Cu, Zn, Ga) is essentially isostructural to $SiAs_2$, $Cs_{0.11}Zn_{0.05}Si_{0.95}As$ synthesized from Cs metal has a framework composed of "deconstructed" SiAs with Cs atoms sitting within each channel (Figure 3.5). This new compound has lower symmetry, crystallizing in the same space group as SiAs, *C*2/*m* [18]. Its *b* and *c* unit cell parameters are very close to those of SiAs, being 3.6659(3) Å and 9.9849(8) Å compared to 3.668 Å and 9.529 Å, respectively. However, the *a* unit cell length is more than doubled at 35.201(3) Å compared to 15.979 Å in SiAs. Along the *a* axis, the framework consists of the three-ring component of SiAs, as shown with the left blue box in Figure 3.5. Along the *c* axis are 5 membered Si-As rings and a connecting Si-Si dumbbell, which correspond to the section of SiAs that have Si-Si dumbbells that alternate parallel and perpendicular to the layer. This is highlighted by the right blue box in Figure 3.5. As a result of the tetrahedral coordination of Si running along both the *a* and *c* axes, $Cs_{0.11}Zn_{0.05}Si_{0.95}As$

loses the 2D layered nature found in binary SiAs and is instead a 3D compound. This compound has a new structure type with the Wyckoff sequence j^2i^{12}. Although layers are no longer present, channels along the *b* axis are formed. Similar to $Cs_{0.16}M_xSi_{1-x}As_2$ (M = Cu, Zn, Ga), Cs disorder within these channels is evident from single crystal XRD. The presence and amount of Zn was confirmed by EDS.

3.3.3 Metal Substitution Content in $Cs_{0.16}M_xSi_{1-x}As_2$ (M = Cu, Zn, Ga)

Using Zintl counting, the expected amount of metal substitution in the Si position can be predicted given the amount of Cs intercalated into the structure. $SiAs_2$ is an electron-balanced semiconductor, because each Si and As atom forms 4 and 3 covalent bonds respectively. Intercalation of Cs generates an excess of electrons, which can be compensated by the partial replacement of Si atoms by a metal containing fewer valence electrons. This mechanism works well for semiconducting clathrates [19]. For instance, 0.16 Cs atoms donate 0.16 extra electrons. For Si/Zn substitution, each substituting Zn atom has two valence electrons and would therefore require two more to form four bonds. This leads to the predicted electron-balanced composition $Cs_{0.16}Zn_{0.08}Si_{0.92}As_2$. In general, we observe a good agreement of the predicted and experimentally determined compositions (Table 3.3). EDS data were averaged across multiple crystals within a sample, excluding crystals that showed very low metal content. Slight variability in the amounts of Cs and *M* has been observed. Approximately 0.16 Cs per $SiAs_2$ unit and corresponding *M* substitution values appear to be the optimal amount. An excess of metal substituent during synthesis tended to form side phases of that metal, such as $ZnSiAs_2$ or GaAs, rather than being inserted into the Si-As framework.

In clathrates, the formation of vacancies is an alternative way to compensate for extra electrons. For example, clathrates with a Sn-pnictide framework and iodine guest atoms have

vacancies that can form in either the tin or pnicogen positions as in $Sn_{20.5}\square_{3.5}As_{22}I_8$ and $Sn_{24}P_{19.3}\square_{2.7}I_8$ ($\square$ = vacancy) [20], or the extra electrons are compensated by substituting Sn with Cu or Zn as in $Sn_{17}Zn_7P_{22}I_8$ and $Sn_{19.3}Cu_{4.7}As_{22}I_8$ [21]. Similarly, for the investigated layered compounds, an absence of an electron-accepting metal causes vacancies in the As positions. The removal of one arsenic atom results in the formation of 3 dangling bonds, each requiring 1 electron. Thus, the total amount of As vacancies is 0.16/3 = 0.053, given 0.16 Cs, which is close to the experimental composition (Table 3.3). The amount of As vacancies given by EDS data for $Cs_{0.16}SiAs_2$ is larger than predicted, though this may be due to a poor conductive carbon coating and lack of an internal standard.

In clathrates, both mechanisms for extra electron compensation may coexist. For example, in $Sn_{20}Zn_4P_{20.8}\square_{1.2}I_8$, both Zn/Sn substitutions and P-vacancies are present. Similarly, in the reported structure of $Cs_{0.16}Ga_{0.1}Si_{0.9}As_{1.98}\square_{0.02}$, Ga atoms take 0.10 of the extra electrons, while the remaining 0.06 electrons are compensated by As vacancies. Based on this observation, we hypothesized that a similar mechanism may be at work for the other substituting metals but is hard to detect due to very small vacancy concentrations.

Table 3.3 *Compositions of* $Cs_yM_xSi_{1-x}As_2$.

	$Cs_ySiAs_{2-z}\square_z$ *		**$Cs_yCu_xSi_{1-x}As_2$**		**$Cs_yZn_xSi_{1-x}As_2$**		**$Cs_yGa_xSi_{1-x}As_{2-z}$***		
	y	*z = y/3*	*y*	*x = y/3*	*y*	*x = y/2*	*y*	*x = y (if z = 0)*	*z = (y-x)/3*
Zintl count	0.16	0.053	0.16	0.053	0.16	0.08	0.16	0.10	0.02
EDS	0.10(1)	0.09(4)	0.20(4)	0.08(2)	0.17(4)	0.10(3)	0.14(2)	0.09(1)	0.03(6)
Single crystal	0.148(2)	0.050(2)	0.170(4)	0.058(4)	0.164(3)	0.080(3)	0.149(5)	0.103(5)	0.023(3)

*EDS and SCXRD values obtained from different samples

3.3.4 Transport Properties

Electrical resistivity measurements were performed on selected single crystals. Reproducibility was checked by measuring at least two different crystals of each composition due to potential problems with crystal exfoliation, crystal breakage, poor adhesion to the silver paste, or poor Pt wire contacts. All measurements revealed semiconducting behavior (Figure 3.6). For the copper- and Zn-containing compounds, the activation energies were calculated to be 0.18(2) eV and 0.25(5) eV, respectively. The activation energy values for the Ga-containing compound had a much larger difference, 0.17 eV (crystal 1) and 0.51 eV (crystal 2). Assuming the measured crystals are representative of the possible variations in Ga and vacancies content we cannot draw a defined conclusion regarding the activation energy. For cationic clathrates, it was shown that vacancies in the framework may play a crucial role in states near the Fermi level and may strongly affect the resistivity [20].

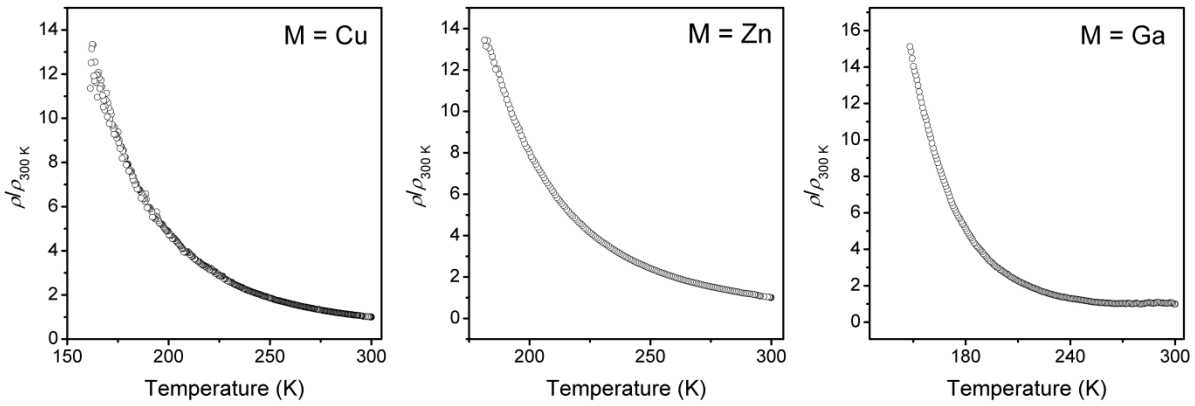

Figure 3.6 *Normalized resistivity measurements for selected crystals of each substituting metal, M, in* $Cs_{0.16}M_xSi_{1-x}As_2$.

Measuring transport properties proved to be difficult as $Cs_{0.16}M_xSi_{1-x}As_2$ cannot withstand high pressures or temperatures at dynamic conditions. Though $Cs_{0.16}Zn_{0.08}Si_{0.92}As_2$ did not appear to decompose by 1273 K as measured by DSC, powder XRD detected the presence of a new phase that may have been As_2O_3 after the DSC experiment. During the

optimization of SPS conditions for $Cs_{0.16}M_xSi_{1-x}As_2$ (M = Zn, Ga), we discovered that heating to temperatures above 573 K in dynamic vacuum caused As to leach out of the sample, and the sample began to lose crystallinity above 76 MPa. PPMS measurements revealed ultra-low thermal conductivity (~0.1 W/m-K at 300 K) for a $Cs_{0.16}Ga_{0.16}Si_{0.84}As_2$ pellet pressed at ambient temperature. With a final pellet density of 51% of the theoretical X-ray density, the extremely low thermal conductivity values cannot be relied upon explicitly.

3.4 Conclusion

We have demonstrated the flexibility of 2D $SiAs_2$ layers with the insertion of the largest non-radioactive cation between the layers as well as partial metal substitution in the Si site without any major distortion to the actual $SiAs_2$ framework. $Cs_{0.16}M_xSi_{1-x}As_2$ (M = Cu, Zn, Ga) is technically a solid solution, with variability in metal substitution, arsenic vacancies, or a combination of both to balance the electron excess brought in by the interstitial Cs atoms. This family has Cs disorder in the channels as detected by single crystal XRD. This Cs disorder, along with the innate anharmonicity of the 2D structure, causes the compound to have low thermal conductivity. Using an advanced local technique such as time-domain thermoreflectance is required to confirm the proposed low thermal conductivity. Resistivity measurements on selected single crystals revealed $Cs_{0.16}M_xSi_{1-x}As_2$ (M = Cu, Zn, Ga) to be narrow bandgap semiconductors.

Our preliminary studies indicate that alkali cations other than Cs can also be incorporated in between $SiAs_2$ or $GeAs_2$ layers. In combination with variability attained by means of substituting a metal into the Si site, these preliminary studies point to a large family of compounds with tunable frameworks and intercalated cation sublattices. This resembles the family of inorganic pnictide clathrates, where tuning of the bonding in the clathrate

framework and guest cation sublattice allows for drastic modifications of transport properties [22]. As such, more exploration into this family is warranted.

3.5 Acknowledgments

We would like to thank Dr. W. Xu and Dr. A. Yakovenko at 17-BM beamline at the APS ANL for assistance with in situ powder XRD. Thank you to Prof. J. Zaikina for use of the SPS machine and arc welder. We would also like to thank S. Lee for preparing the selected samples for EDS measurements. Use of the Advanced Photon Source at Argonne National Laboratory was supported by the U.S. Department of Energy, Office of Science, Office of Basic Energy Sciences, under Contract No. DE-AC0206CH11357.

3.6 References

[1] a) K.S. Novoselov, A.K. Geim, S.V. Morozov, D. Jian, Y. Zhang, S.V. Dubonos, I.V. Grigorieva, A.A. Firsov. *Science* **2004**, *306*, 666; b) R.R. Nair, P. Blake, A.N. Grigorenko, K.S. Novoselov, T.J. Booth, T. Stauber, N.M.R. Peres, A.K. Greim. *Science* **2008**, *320*, 1308; c) C. Lee, X. Wei, J. W. Kysar, J. Hone. *Science* **2008**, *321*, 385; d) G. Tsoukleri, J. Parthenios, K. Papagelis, R. Jalil, A.C. Ferrari, A.K. Geim, K.S. Novoselov, C. Galiotis. *Small* **2009**, *5*, 2397; e) E. Pop, V. Varshney, A.K. Roy. *MRS Bulletin* **2012**, *37*, 1273; f) Z. Fan, L.F.C. Pereira, P. Hirvonen, M.M. Ervasti, K.R. Elder, D. Donadio, T. Ala-Nissila, A. Harju. *Phys. Rev. B* **2017**, *95*, 144309; g) T. Ramanathan, A.A. Abdala, S. Stankovich, D.A. Dikin, M. Herrera-Alonso, R.D. Piner, D.H. Adamson, H.C. Schniepp, X. Chen, R.S. Ruoff, S.T. Nguyen, I.A. Aksay, R.K. Prud'Homme, L.C. Brinson. *Nat. Nanotechnol.* **2008**, *3*, 327.

[2] a) J. Greim, K.A. Schwetz. *Ullman's Encyclopedia of Industrial Chemistry*, Wiley-VCH, Weinheim, Germany **2006**; b) S.Z. Butler, S.M. Hollen, L. Cao, Y. Cui, J.A. Gupta, H.R. Gutiérrez, T.F. Heinz, S.S. Hong, J. Huang, A.F. Ismach, E. Johnston-Halperin, M. Kuno, V.V. Plashnitsa, R.D. Robinson, R.S. Ruoff, S. Salahuddin, J. Shan, L. Shi, M.G. Spencer, M. Terrones, W. Windl, J.E. Goldberger. *ACS Nano* **2013**, *7*, 2898; c) L. Song, L. Ci, H. Lu, P.B. Sorokin, C. Jin, J. Ni, A.G. Kvashnin, D. Kvashnin, J. Lou, B.I. Yakobson, P.M. Ajayan. *Nano Lett.* **2010**, *10*, 3209; d) L. Li, Y. Yu, G.J. Ye, Q. Ge, X. Ou, H. Wu, D. Feng, X.H. Chen, Y. Zhang. *Nat. Nanotechnol.* **2014**, *9*, 372; e) F. Xia, H. Wang, Y. Jia. *Nat. Commun.* **2014**, *5*, 4458; f) J. Qiao, X. Kong, Z.-H. Hu, F. Yang, W. Ji. *Nat. Commun.* **2014**, *5*, 4475; g) Y.-C. Lin, W. Zhang, J.K. Huang, K.K. Liu, Y.H. Lee, C.T. Liang, C.W. Chu, L.J. Li. *Nanoscale* **2012**, *4*, 6637; h) A. Pakdel, C. Zhi, Y. Bando, D. Golberg. *Mater. Today* **2012**, *15*, 256; i) C.N.R. Rao, H.S.S. Ramakrishna Matte, U. Maitra. *Angew. Chem. Int. Ed.* **2013**, *52*, 13162; j) M. Zeraati, S.M.V. Allaei, I.A. Sarsari, M. Pourfath, D. Donadio. *Phys. Rev. B* **2016**, *93*, 085424; k) A. Molle, J. Goldberger, M. Houssa, Y. Xu, S.-C. Zhang, D. Akinwande. *Nat. Mater.* **2017**, *16*, 163; l) E. Bianco, S. Butler, S. Jiang, O.D. Restrepo, W. Windl, J.E. Goldberger. *ACS Nano* **2013**, *7*, 4414; m) F.-C. Hsu, J.-Y. Luo, K.-W. Yeh, T.-K.

Chen, T.-W. Huang, P.M. Wu, Y.-C. Lee, Y.-L. Huang, Y.-Y. Chu, D.-C. Yan, M.-K. Wu. *Proc. Natl. Acad. Sci. U.S.A.* **2008**, *105*, 14262; n) J.T. Greenfield, S. Kamali, K. Lee, K. Kovnir. *Chem. Mater.* **2015**, *27*, 588; o) J.-F. Ge, Z.-L. Liu, C. Liu, C.-L. Gao, D. Qian, Q.-K. Xue, Y. Liu, J.-F. Jia. *Nat. Mater.* **2015**, *14*, 285.

[3] a) L.-D. Zhao, S.-H. Lo, Y. Zhang, H. Sun, G. Tan, C. Uher, C. Wolverton, V.P. Dravid, M.G. Kanatzidis. *Nature* **2014**, *508*, 373; b) L.-D. Zhao, G. Tan, S. Hao, J. He, Y. Pei, H. Chi, H. Wang, S. Gong, H. Xu, V.P. Dravid, C. Uher, G.J. Snyder, C. Wolverton, M.G. Kanatzidis. *Science* **2015**, aad3749; c) K. Peng, X. Lu, H. Zhan, S. Hui, X. Tang, G. Wang, J. Dai, C. Uher, G. Wang, X. Zhou. *Energy Environ. Sci.* **2016**, *9*, 454; d) C. Chang, M. Wu, D. He, Y. Pei, C.F. Wu, X. Wu, H. Yu, F. Zhu, K. Wang, Y. Chen, L. Huang. *Science* **2018**, *360*, 778.

[4] a) D.T. Morelli, G.P. Meisner. *J. Appl. Phys*. **1995**, *77*, 3777; b) A. Zevalkink, D.M. Smiadak, J.L. Blackburn, A.J. Ferguson, M.L. Chabinyc, O. Delaire, J. Wang, K. Kovnir, J. Martin, L.T. Schelhas, T.D. Sparks, S.D. Kang, M.T. Dylla, G.J. Snyder, B.R. Ortiz, E.S. Toberer. *Appl. Phys. Rev.* **2018**, *5*, 021303.

[5] G.A. Slack. *CRC Handbook of Thermoelectrics*, CRC Press, Boca Raton, U.S.A. **1995**.

[6] a) W. Koshibae, K. Tsutsui, S. Maekawa. *Phys. Rev. B* **2000**, *62*, 6869; b) T. Tanaka, S. Nakamura, S. Iida. *Jpn. J. Appl. Phys.* **1994**, *33*, L581; c) I. Terasaki. *Physica B* **2003**, *328*, 63.

[7] a) T. Wadsten. *Acta Chem. Scand.* **1967**, *21*, 1374; b) K. Lee, S. Synnestvedt, M. Bellard, K. Kovnir. *J. Solid State Chem.* **2015**, *224*, 62.

[8] a) L. Zhou, Y. Guo, J. Zhao. *Physica E* **2018**, *95*, 149; b) F. Shojaei, H.S. Kang. *Phys. Chem. Chem. Phys.* **2016**, *18*, 32458; c) F.Q. Wang, Y. Guo, Q. Wang, Y. Kawazoe, P. Jena. *Chem. Mater.* **2017**, *29*, 9300; d) T. Zhao, Y. Sun, Z. Shuai, D. Wang. *Chem. Mater.* **2017**, *29*, 6261; e) S.K. Matta, C. Zhang, Y. Jiao, A. O'Mullane, A. Du. *Beilstein J. Nanotechnol.* **2018**, *9*, 1247; f) P. Wu, M. Huang. *Phys. Status Solidi* **2016**, *253*, 862; g) F. Shojaei, J.R. Hahn, H.S. Kang. *J. Mater. Chem. A* **2017**, *5*, 22146.

[9] a) K. Lee, S. Kkamali, T. Ericsson, M. Bellard, K. Kovnir. *Chem. Mater.* **2016**, *28*, 2776; b) J. Guo, Y. Liu, Y. Ma, E. Zhu, S. Lee, Z. Lu, Z. Zhao, C. Xu,S.-J. Lee, H. Wu, K. Kovnir, Y. Huang, X. Duan. *Adv. Mater.* **2018**, *30*, 1705934.

[10] G. M. Sheldrick, *Acta Crystallogr., Sect. C: Struct. Chem.* **2015**, *71*, 3.

[11] K. Momma, F. Izumi, *J. Appl Crystallogr.* **2011**, *44*, 1272.

[12] B. H. Toby, R. B. Von Dreele, *J. Appl. Crystallogr.* **2013**, *46*, 544.

[13] T. Wadsten. *Acta Chem. Scand.* **1967**, *21*, 593.

[14] H. He, A. Zevalkink, Z.M. Gibbs, G.J. Snyder, S. Bobev. *Chem. Mater.* **2012**, *24*, 3596.

[15] a) I.S.Miller, P. Boettcher. *Z. Kristallogr. Cryst. Mater.* **1991**, *196*, 137; b) T. Ohtani, Y. Sano, K. Kodama, S. Onoue, H. Nishihara. *Mat. Res. Bull.* **1993**, *28*, 501; c) H.H. Park, M. Pezat, B. Darriet. *Rev. Chim. Miner.* **1986**, *23*, 323.

[16] a) K. Takemura, K. Syassen. *Phys. Rev. B* **1985**, *32*, 2213; b) Y. Xu, J.S. Tse, A.R. Oganov, T.A. Cui, H. Wang, Y.M. Ma, Z.G. Tian. *Phys. Rev. B* **2009**, *79*, 144110.

[17] F. Gascoin, S.C. Sevov. *Inorg. Chem.* **2002**, *41*, 2820.

[18] T. Wadsten. *Acta. Chem. Scand.* **1965**, *19*, 1232.

[19] J.-A. Dolyniuk, B. Owens-Baird, J. Wang, J.V. Zaikina, J.V, K. Kovnir. *Mater. Sci. Eng. R Rep.* **2016**, *108*, 1.

[20] a) M.M. Shatruk, K. Kovnir, A.V. Shevelkov, I.A. Presniakov, B.A. Popovkin. *Inorg. Chem.* **1999**, *38*, 3455; b) J.V. Zaikina, K. Kovnir, A.V. Sobolev, I.A. Presniakov, Y. Prots, M. Baitinger, W. Schnelle, A.V. Olenev, O.I. Lebedev, G. Van Tendeloo, Y. Grin, A.V. Shevelkov. *Chem. Europ. J.* **2007**, *13*, 5090.

[21] a) K. Kovnir, M.M. Shatruk, L.N. Reshetova, I.A. Presniakov, E.V. Dikarev, M. Baitinger, F. Haarmann, W. Schnelle, M. Baenitz, Y. Grin, A.V. Shevelkov. *Solid State Sci.* **2005,** *7*, 957; b) K. Kovnir, A.V. Sobolev, I.A. Presniakov, O.I. Lebedev, G. Van Tendeloo, W. Schnelle, Y. Grin, A.V. Shevelkov. *Inorg. Chem.* **2005,** *44*, 8786.

[22] a) J. Wang, Y. He, N.E. Mordvinova, O.I. Lebedev, K. Kovnir. *Chem* **2018**, *4*, 1465; b) J.-A. Dolyniuk, J. Wang, M. Marple, S. Sen, Y. Cheng, A.J. Ramirez-Cuesta, K. Kovnir. *Chem. Mater.* **2018**, *30*, 3419; c) J. Wang, L.-L. Wang, K. Kovnir. *J. Mater. Chem. A* **2018**, *6*, 4759; d) J. Wang, J.-A. Dolyniuk, K. Kovnir. *Acc. Chem. Res.* **2018**, *51*, 31; e) J. Wang, O.I. Lebedev, K. Lee, J.-A. Dolyniuk, P. Klavins, S. Bux, K. Kovnir. *Chem. Sci.* **2017**, *8*, 8030; f) J.-A. Dolyniuk, P.S. Whitfield, K. Lee, O.I. Lebedev, K. Kovnir. *Chem. Sci.* **2017**, *8*, 3650; g) J.-A. Dolyniuk, J.V. Zaikina, D.C. Kaseman, S. Sen, K. Kovnir. *Angew. Chem. Int. Ed.* **2017**, *56*, 2418; h) J. Wang, D.C. Kaseman, K. Lee, S. Sen, K. Kovnir. *Chem. Mater.* **2016**, *28*, 4741; i) J.-A. Dolyniuk, J. Wang, K. Lee, K. Kovnir. *Chem. Mater.* **2015**, *27*, 4476; j) J. Fulmer, O.I. Lebedev, V.V. Roddatis, D.C. Kaseman, S. Sen, J.-A. Dolyniuk, K. Lee, A.V. Olenev, K. Kovnir. *J. Amer. Chem. Soc.* **2013**, *135*, 12313.

CHAPTER 4. BP: SYNTHESIS AND PROPERTIES OF BORON PHOSPHIDE

The contents of this chapter have been published in Materials Research Express. Woo, K.; Lee, K.; Kovnir, K. Mater. Res. Expr. ***2016,*** *3, 074003.*

4.1 Introduction

Boron phosphide (BP) exhibits unique properties that make it a possible contender for many practical applications. BP has a cubic zinc-blende structure, with boron and phosphorus tetrahedrally coordinated to each other. In this compound, typical properties of borides, such as high chemical inertness and a hardness that is roughly the same as that of SiC, are combined with semiconducting properties found in other III–V binary compounds [1]. A wide band gap of 2.1 eV in the optical region of the electromagnetic spectrum [2] and a flat band potential of −0.43 V versus SHE (standard hydrogen electrode) in water make BP a candidate for oxygen generation through water splitting [3]. BP is also a very efficient heat conductor with a room temperature thermal conductivity of 400 W (m K) $^{-1}$ [4].

In spite of its potentially versatile technological uses, BP is not a common material due to synthetic challenges. While phosphorus is a very reactive element capable of reacting with noble metals at elevated temperatures, boron is highly inert, requiring temperatures of at least 1200 K to react when amorphous and temperatures >2300 K to melt crystalline boron. At such high temperatures, the high vapor pressure of phosphorus leads to the depletion of P from the reaction mixture and the formation of non-homogeneous, multiphase samples. The vast difference in the reactivities of these elements makes the synthesis of BP challenging. Previous methods of synthesizing BP include reduction of PBI_2 by H_2 gas [5], decomposition of BBr_3PH_3 [6], chemical vapor deposition [7], gas phase reactions [8], molten nickel or nickel phosphide reactions [9, 10], and high pressure methods [4, 11, 12]. Herein, we present

a comprehensive comparison of three synthetic methods for synthesizing BP: a traditional solid-state route, Sn flux synthesis, and a metathesis reaction route.

4.2 Methods

4.2.1 Powder X-Ray Diffraction (XRD)

Produced samples were characterized by powder XRD using a Rigaku Miniflex 600 diffractometer with Cu–K_α radiation with a Ni–K_β filter. The samples were finely ground and analyzed at room temperature on Si zero background holders. Unit cell refinements were performed with WinCSD [13] using NIST Si 640d as a standard.

4.2.2 Synchrotron XRD

Finely pulverized samples synthesized from each method were sieved through 325 mesh and transferred to a Kapton capillary. The samples were analyzed at beamline 11-BM at the Advanced Photon Source at the Argonne National Laboratory using a radiation wavelength of 0.414160 Å. Unit cell refinement of the data was performed with WinCSD [13].

4.2.3 Raman Spectroscopy

Raman spectroscopy was performed using a Renishaw RM1000 Laser Microscope (λ = 514 nm) with a motorized stage. Samples were prepared by sprinkling the material onto Kapton tape on a glass microscope slide.

4.2.4 Solid-State UV-Vis Spectroscopy

UV–vis diffuse reflectance spectra were obtained using a Thermo Scientific Evolution 220 Spectrometer and converted to the Kubelka–Munk function. To prepare the samples, ground material was sonicated in water and drop cast onto white filter paper backed with Teflon tape.

4.2.5 Scanning Electron Microscopy and Energy Dispersive X-Ray Spectroscopy

Analysis of the elemental composition was carried out on a Hitachi S-4100T scanning electron microscope (SEM) with Oxford INCA Energy Dispersive X-ray Spectroscopy (EDS). BP samples were sprinkled onto carbon tape and analyzed at 20 keV.

4.3 Synthesis

Three methods of synthesizing BP were explored. All starting materials, boron (Alfa Aesar, amorphous and crystalline, 99%), boron triiodide (Sigma Aldrich, 95%), red phosphorus (Alfa Aesar, 99%), and tin shot (Alfa Aesar, 99.8%) were used as received. Because of the high vapor pressure of phosphorus, the ratio of phosphorus mass to ampoule volume was taken into consideration to prevent the ampoule from exploding when a flux was not used. A phosphorus mass to ampoule volume ratio not exceeding 50 mg:1 cm^3 was deemed safe.

4.3.1 High-Temperature Solid-State Synthesis from Elements

To synthesize BP from elements, a B:P ratio of 1:1.2 with a total weight of 200 mg was loaded in a silica ampoule with an inner diameter of 9 mm and an outer diameter of 11 mm. The ampoule was evacuated and sealed such that the resulting ampoule length was 140 mm. The ampoule was heated over 4 h to 1323 K in a tube furnace and annealed for ten days. After this, excess phosphorus was removed by applying a temperature gradient with one end of the ampoule heated to 673 K and the other end kept at room temperature for 24 h, which resulted in sublimed phosphorus deposited at the cold end. The product of this synthesis is further denoted as BP-E.

4.3.2 Sn Flux Synthesis

For reactions made from Sn flux, a B:P:Sn ratio of 1:1:2 with a 500 mg total weight of B and P was sealed in an evacuated silica ampoule with silica wool placed at the top part

of the ampoule. The ampoule was placed in a muffle furnace, pre-annealed at 673 K for 24 h, ramped over 12 h to 1073 K, and annealed at this temperature for 24 h. At the end of annealing, the flux was removed by high temperature centrifugation at 1073 K. Any remaining Sn was removed by washing in a 1:1 H_2O:HCl bath. After an overnight acid treatment, the material was filtered, rinsed with water, and dried in air. The product of this synthesis is further denoted as BP-F.

4.3.3 Solid-State Metathesis Synthesis

A solid-state metathesis synthesis was performed by loading a BI_3:P molar ratio of 2:5 with a total weight of 500 mg into a silica ampoule. The ampoule was evacuated and flame sealed. The ampoule's inner diameter was 14 mm, outer diameter was 16 mm, and length was 120 mm. Handling of the starting materials was performed inside an argon-filled glovebox with the O_2 level below 0.5 ppm. The ampoule was placed in a tube furnace and heated over 5 h so that the reactants were at 1173 K and the other end of the ampoule was at 1113 K. The sample was annealed at this temperature gradient for 18 h. The temperature of the reactant end was then lowered to 673 K and annealed for 4 h to convert any remaining white phosphorus into red phosphorus. The colder end of the ampoule was found to only contain fibrous phosphorus and was discarded. The other end of the silica ampoule was rinsed with water to remove the product from the walls as well as to dissolve the P_2I_4 side product. The product was filtered and then dried in a vacuum oven at 423 K for 2 h. Afterwards, red phosphorus was removed by sublimation at 673 K for one day. In order to improve crystallinity, the sample was reannealed at 1273 K for three days inside an evacuated silica ampoule. The product of this synthesis is further denoted as BP-SSM.

4.4 Results and Discussion

4.4.1 Synthesis

BP was synthesized via three reaction methods: from elements, tin flux, and using a metathesis route. The formation of BP through the reaction of elemental B and P was first reported by Popper and Ingles in 1957 [14]. As mentioned above, the phosphorus vapor pressure must be taken into account when using the traditional solid-state method, therefore limiting the scale of the reaction. Due to the low reactivity of boron, a high temperature of at least 1273 K and a long reaction time is required. Typical boron as a starting material is a mixture of amorphous and crystalline boron, in which the former dominates. The product of the reaction using said starting material with phosphorus was always contaminated with unreacted crystalline boron.

The second synthesis method is through the use of a Sn flux. Previous methods to synthesize BP involving a flux include single crystal growth from nickel phosphide melts [10], a combination of high pressure and a nickel phosphide melt [15], and flowing phosphorus gas over boron dissolved in a nickel metal solvent [9]. While these methods can produce single crystals, they require temperatures above 1273 K and up to three weeks of reaction time. With the Sn flux method reported herein, both the reaction temperature and time are greatly reduced. The problem of high phosphorus vapor pressure is also eliminated as phosphorus dissolves in the Sn flux, therefore allowing large quantities of BP to be produced. However, any crystalline boron in the starting material remained as an admixture, and it was found that Sn is able to partially incorporate into the BP structure.

The final method is based on solid-state metathesis, in which boron triiodide reacts with phosphorus to form BP and phosphorus iodide byproducts. Previously reported methods using boron halides or phosphorus halides required the use of reducing agent, usually H_2 gas

[8] or Na [16]. Using a boron compound as a boron source eliminates the problem of a crystalline boron admixture. Because the reaction is driven by the formation of the stable B–P bond, the reaction can be completed in hours rather than days and does not require the high temperatures needed for elemental synthesis. Our studies indicated that BP can be produced through metathesis reactions with only an hour annealing at a temperature as low as 973 K. Crystallinity of the product improved with extended annealing time or upon reannealing. The scale of the reaction is limited by the vapor pressures of both starting materials as they react in the gas phase. However, the calculated yield based on boron was 65%, which is reasonable considering the natural loss of product through washing and vessel transfer.

4.4.2 Powder XRD

All synthetic methods produced BP as a dark red-brown polycrystalline powder. After washing and subliming to remove admixtures, BP-SSM samples appeared to be a single crystalline phase according to laboratory powder XRD patterns (Figure 4.1). BP-E and BP-F had traces of unreacted crystalline boron from the starting material, which is apparent from the set of powder XRD peaks from 10–30° 2θ as seen in the inset of Figure 4.1 and the shoulder on the most intense BP peak. The overall relative intensities of crystalline boron admixture peaks do not exceed 5%. Note that most commercially available amorphous boron sources contain some amount of crystalline boron. The diffraction peaks for BP-F samples were found to have a slight shift towards smaller diffraction angles when compared to BP-E or BP-SSM, indicating the possibility of Sn doping from the flux. The unit cell parameter for the BP-F sample, a = 4.5398(1) Å, was calculated to be significantly higher than the unit cells of samples produced from elements, a = 4.5375(3) Å, or by metathesis reaction, a = 4.5379(1) Å. The increase in the unit cell may be caused by the incorporation of larger Sn

atoms into the crystal structure of BP. The peaks for BP-F were found to be broader than those of BP-E, indicating lower crystallinity, which may stem from defects caused by doping.

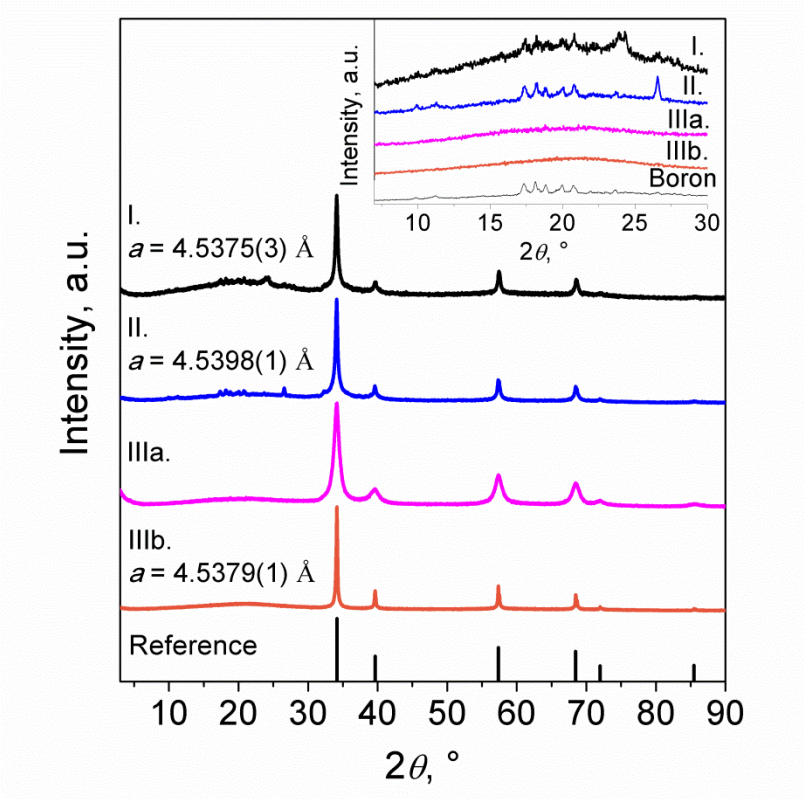

Figure 4.1 *Normalized powder x-ray diffraction patterns for BP-E (I, black), BP-F (II, blue), BP-SSM before reannealing (IIIa, magenta) and BP-SSM after reannealing (IIIb, orange) along with the reference pattern. Inset shows the low angle region, indicating the presence of crystalline boron starting material in BP-E and BP-F. Calculated unit cell parameters are given on the left.*

4.4.3 Synchrotron XRD

To clarify the unit cells for the BP-E and BP-F samples, high-resolution synchrotron powder diffraction experiments were performed. This revealed a drastic difference between the two samples: while BP-E was confirmed to be single phase cubic BP, BP-F appeared to be a mixture of two phases with slightly different unit cells, both of them larger than the unit cell for BP-E (Figure 4.2). The inset in Figure 4.2 shows the typical shape of the diffraction

peaks of the BP-F sample. This is not due to structural distortion or symmetry lowering since all peaks have identical shapes, including peaks of (*hhh*) type, such as (222) and (333).

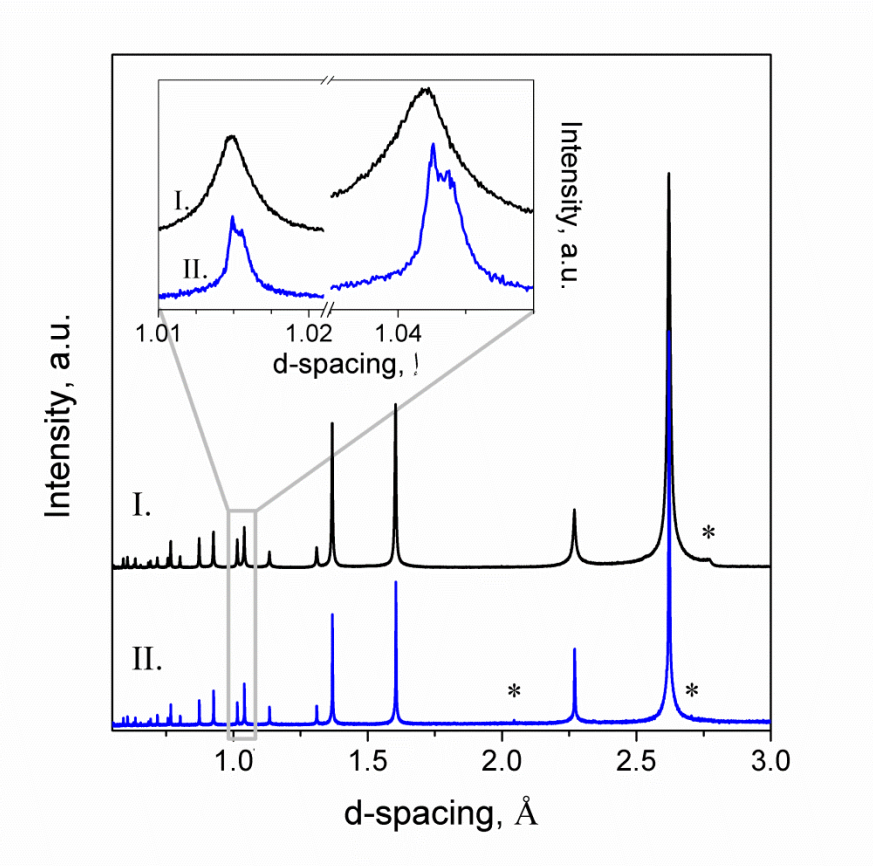

Figure 4.2 *Normalized synchrotron powder x-ray diffraction patterns of BP-E (I, black) and BP-F (II, blue). Asterisks indicate unreacted crystalline boron. Inset shows enlarged 1.01–1.0475 Å range.*

The refined lattice parameter from synchrotron data for BP-E was 4.5370(1) Å, which is in good agreement with the cell determined from laboratory powder XRD data where *a* = 4.5375(3) Å. Synchrotron data revealed BP-F is a mixture of BP phases with lattice parameters 4.54155(8) Å and 4.53862(4) Å. The average of these two parameters is close to the unit cell determined by the lower resolution laboratory powder XRD method, *a* = 4.5398(1) Å. Since the calculated unit cell parameters for both phases in BP-F are larger than those of pristine BP, we assume that flux synthesis results in two phases that contain Sn

incorporations into the crystal structure. This assumption was further supported by Raman and EDS studies.

4.4.4 Raman Spectroscopy

Raman investigations revealed drastic differences between BP-F and the other two samples (Figure 4.3). The Raman spectra for the BP-E and BP-SSM samples are in good agreement with literature data. Both exhibit a major peak at 825 cm^{-1}, which is close to the reported and calculated longitudinal optical phonon peak of BP at 829 cm^{-1} [17, 18]. BP-F samples exhibit a similar major peak at 825 cm^{-1}, however the large drop in band intensity and significant increase in peak width indicates low crystallinity or a high concentration of strain and defects. This may be caused by the incorporation of Sn into the BP structure.

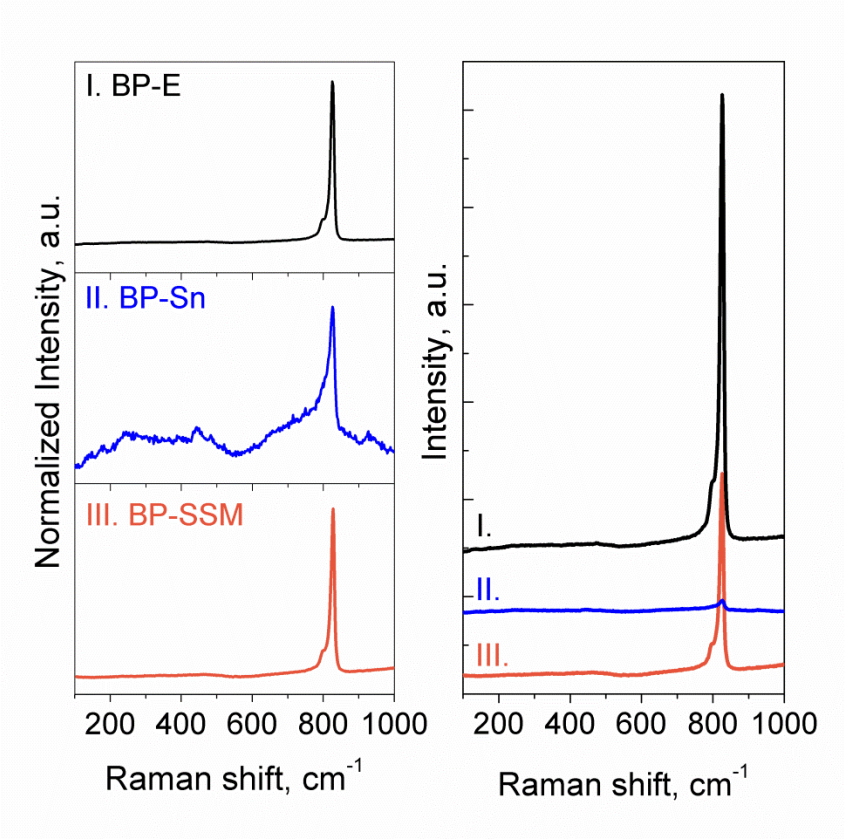

Figure 4.3 *Left: normalized Raman spectra of BP-E (I, black), BP-F (II, blue), and BP-SSM (III, orange). Right: each Raman spectrum true to scale.*

4.4.5 Elemental Analysis

To determine whether Sn or I was present in BP-F and BP-SSM respectively, the compounds were analyzed with SEM-EDS (Figure 4.4). Boron is difficult to detect and quantify using EDS due to the low intensity of boron peaks and the overlap of peak positions with C and O peaks. Carbon and oxygen are present in all spectra due to the carbon tape used to mount the samples and from adsorption of atmospheric species. Unlike boron, P, Sn, and I can be quantitatively detected using EDS. No elements other than P were detected in samples BP-E and BP-SSM, including iodine, for which peaks at 0.50 and 3.94 keV would be expected.

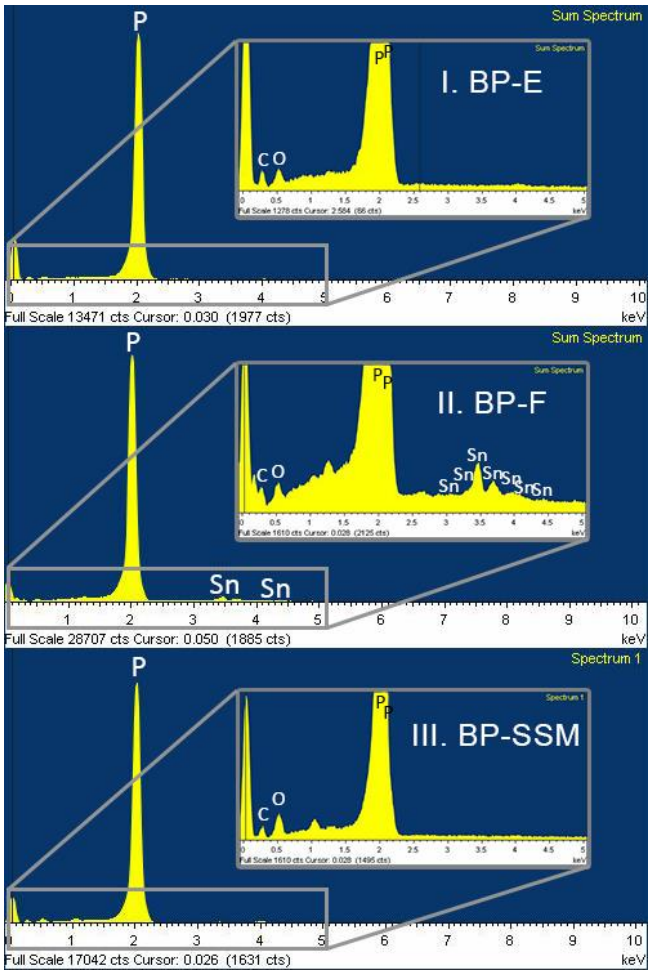

Figure 4.4 *Energy dispersive x-ray spectra for BP-E (I), BP-F (II), and BP-SSM (III). Insets show a magnified region from 0–5 keV in which Sn or I peaks would appear.*

For the BP-F sample, even after extensive acid washes, Sn was consistently found to be present in the sample. This suggests that Sn is not simply a surface contamination but present in the bulk sample. This observation is in line with the results from XRD and Raman characterizations. Sn has a covalent radius of 1.4 Å, which is substantially larger than either B or P, which have covalent radii of 0.85 Å and 1.1 Å, respectively. Incorporation of even a small amount of Sn would lead to significant structural distortions, which were detected by Raman spectroscopy. With an average Sn:P atomic ratio of 1.7(5):98.3(5), we calculated the average composition of a new ternary phase as $Sn_{0.017(5)}B_{0.983}P_1$, assuming that Sn substitutes boron. We assume that Sn will prefer to form Sn–P bonds rather than Sn–B bonds due to the fact that many extended solids with Sn coordinated to P have been reported, and no examples of extended solids containing Sn–B bonds were reported [19–21]. Sn–B bonds are mainly found in molecular derivatives of stanna-*closo*-dodecaborate [22]. Detailed single crystal XRD structural analysis is required to support our assumption.

To verify the assumption of Sn doping into B sublattice, the products of each reaction were annealed in open alumina crucibles or open silica tubes in air at 1273 K for up to 2 days. Powder XRD analysis of the completely oxidized samples revealed that the BP-SSM sample was converted to single phase BPO_4 as expected of the oxidation of BP. However, oxidation of the BP-F sample resulted in a mixture of BPO_4 and SnP_2O_7. The absence of tin borates or tin oxides in the products indicates that the composition of the Sn-containing phase is indeed $Sn_xB_{1-x}P_1$. Finally, the oxidation of the BP-E sample resulted in a mixture of BPO_4 and B_2O_3, confirming the presence of excess boron in the BP-E sample.

4.4.6 Optical Properties

The currently accepted indirect bandgap of BP is ~2.1 eV, which corresponds to the compound's reddish brown color, though a range of colors from black to colorless has been

reported. Contrary to the reported value, each sample synthesized had non-zero absorption at 1.1 eV, which is the instrument's lowest detection energy (left panel in Figure 4.5). The low energy absorption of <1.1 eV is hypothesized to be from amorphous impurities rather than due to the indirect bandgap of the synthesized BP. Boron and phosphorus starting materials were analyzed to see whether they were contributing to the experimental low bandgap value. However, both did not exhibit absorptions less than 1.1 eV.

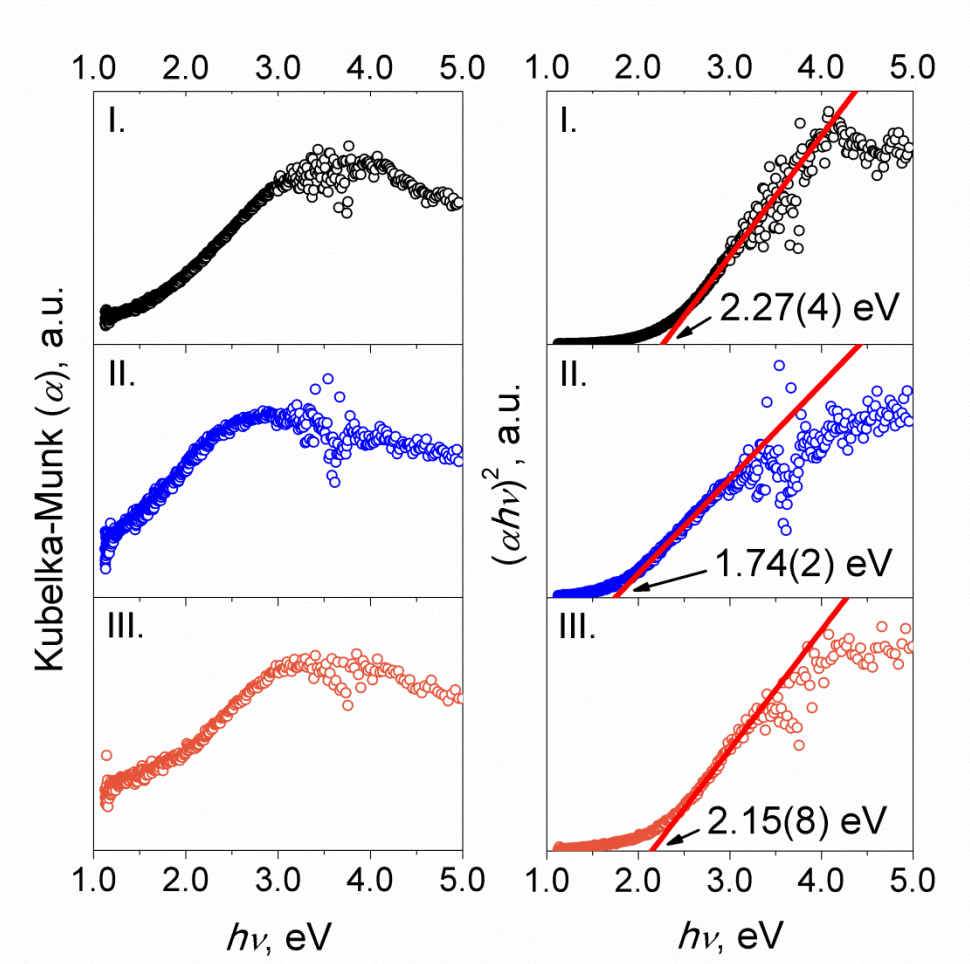

Figure 4.5 *Left: Kubelka–Munk converted spectra for BP-E (I, black), BP-F (II, blue), and BP-SSM (III, orange). Right:* $(\alpha h\nu)^2$ vs. *energy plots.*

The main absorption for all three spectra in Figure 4.5 occurs at energies close to 2 eV. To suppress the admixture contribution, $(\alpha h\nu)^2$ versus $h\nu$ plots were calculated, where α

is the Kubelka–Munk function (right panel in Figure 4.5). Resulting bandgaps for B-E and BP-SSM were 2.27(4) eV and 2.15(8) eV respectively, which are within three standard deviations from each other and are similar to reported literature values of the indirect band gap of BP. The bandgap for BP-F was much lower at 1.74(2) eV, which is expected since the incorporation of Sn should result in the formation of dopant states in the bandgap, thus reducing the overall bandgap value.

4.4.7 Chemical Stability

BP synthesized by all three methods was found to be stable in strong acids, bases, and oxidizers. About 30 mg of each BP sample was placed in baths of concentrated hydrochloric acid, saturated sodium hydroxide, and fresh *aqua regia* (1 part nitric acid and 3 parts hydrochloric acid) for several days. No degradation of crystallinity, reduction of particle size, or changes in unit cell parameters were observed by powder XRD and SEM.

4.4.8 Sn-Doped BP

Although utilizing Sn flux does not produce pristine BP, the Sn-doped compound piques interest as a metal borophosphide. Currently, only nine inorganic compounds that contain the B–P bond are known, not including the two binary compounds, BP and $B_{12}P_2$. Two of the eight ternary compounds are halides, PB_4F_9 and $P_2B_4Cl_4$ [23, 24], and five are isostructural compounds, A_3BP_2 (A = Na, Na/K, K, Rb, Cs) [25–29]. The eighth compound, B-doped $AlPSi_3$, was discovered 20 years after the discovery of the previous metal borophosphides [30]. However, the incidence of the B–P bond is very low as B only substitutes 4%–6% of the Al atoms. Another recently reported compound, $Li(P_xC_{1-x})_2B_{12}$, is composed of B_{12} icosahedral clusters connected into three-dimensional framework via exohedral B–B bonds and disordered (P/C)–(P/C) dumbbells [31]. As such, Sn-doped BP is a rare example of a new metal borophosphide.

4.5 Conclusion

Three methods were tested for synthesizing cubic BP. Reaction from elements produced clean samples aside from unreacted crystalline boron, although the scale of reaction was restricted by the phosphorus vapor pressure. The use of Sn flux allowed for a larger scale reaction, a reaction temperature under 1273 K, and a shorter reaction time. However, the product was not pristine BP due to the incorporation of Sn into the BP structure, and a novel ternary Sn-doped BP compound was formed. Synchrotron powder XRD revealed that the product was actually a mixture of BP-like phases with different unit cell parameters. Unreacted crystalline boron also remained as a product of this synthetic method. Solid state metathesis, an extremely fast method, produced clean BP with highly improved crystallinity after re-annealing. This is the cleanest and fastest synthetic route, although the scale of reaction is restricted due to the vapor pressures of both phosphorus and boron triiodide.

4.6 Acknowledgements

We thank Dr. Frank Osterloh for access to the solid state UV–vis spectrometer, Dr. Joshua Greenfield for his assistance in synchrotron data refinement, and Dr. Andrei Olenev for preliminary Sn flux syntheses. This research is supported by the UC Davis and ACS Petroleum Research Fund, grant 55036-DNI10. Use of the Advanced Photon Source at Argonne National Laboratory was supported by the US Department of Energy, Office of Science, Office of Basic Energy Sciences, under Contract No. DE-AC02-06CH11357.

4.7 References

[1] B. Stone, D. Hill. *Phys. Rev. Lett*. **1960**, *4*, 282.

[2] R.J. Archer, R.Y. Koyama, E.E. Loebner, R.C. Lucas. *Phys. Rev. Lett*. **1964**, *12*, 538.

[3] A. Goossens, E.M. Kelder, J. Schoonman. *Ber. Bunsenges. Phys. Chem.* **1989**, *93*, 1109.

[4] Y. Kumashiro, T. Mitsuhashi, S. Okaya, F. Muta, T. Koshiro, Y. Takahashi, M. Mirabayashi. *J. Appl. Phys*. **1989**, *65*, 2147.

[5] H. Moissan. *C. R. Acad. Sci*. **1891**, *113*, 726.

[6] M. Besson. *C. R. Acad. Sci*. **1891,** *113*, 78.

[7] Y. Kumashiro, Y. Okada. *Appl. Phys. Lett*. **1985**, *47*, 64.

[8] F.V. Williams, R.A. Ruehrwein. *J. Amer. Chem. Sci*. **1960**, *82*, 1330.

[9] U. Nwagwu, *Flux Growth and Characteristics of Cubic Boron Phosphide*, Kansas State University, **2013**.

[10] T.L. Chu, J.M. Jackson, R.K. Smeltzer. *J. Electrochem. Soc*. **1973**, *120*, 802.

[11] K. Ananthanarayanan, C. Mohanty, P. Gielisse. *J. Cryst. Growth* **1973**, *20*, 63.

[12] V.A. Mukhanov, P.S. Sokolov, Y.L. Godec, V.L. Solozhenko. *J. Superhard Mater*. **2013**, *35*, 415.

[13] L. Akselrud, Y. Grin. WinCSD:Software Package for Crystallographic Calculations (Version 4). *J. Appl. Crystallogr*. **2014**, *47*, 803.

[14] P. Popper, T.A. Ingles. *Nature*. **1957**, *179*, 1075.

[15] Y. Kumashiro. *J. Mater. Res*. **1990**, *5*, 2933.

[16] X. Feng, L.-Y. Shi, J.-Z. Hang, J.-P. Zhang, J.-H. Fang, Q.-D. Zhong. *Mater. Lett*. **2005**, *59*, 865.

[17] O. Brafman, G. Lengyel, S. Mitra, P. Gielisse, J. Plendl, L. Mansur. *Solid State Commun*. **1968**, *6*, 523.

[18] J.A. Sanjurjo, E. López-Cruz, P. Vogl, M. Cardona. *Phys. Rev. B* **1983**, *28*, 4579.

[19] K. Kovnir, Y.V. Kolen'Ko, S. Ray, J. Li, T. Watanabe, M. Itoh, M. Yoshimura, A.V. Shevelkov. *J. Solid State Chem*. **2006**, *179*, 3756.

[20] J.V. Zaikina, K. Kovnir, A.N. Sobolev, I.A. Presniakov, V.G. Kytin, V.A. Kulbachinskii, A.V. Olenev, O.I. Lebedev, G.V. Tendeloo, E.V. Dikarev, A.V. Shevelkov. *Chem. Mater*. **2008**, *20*, 2476.

[21] J. Gullman. *J. Solid State Chem*. **1990**, *87*, 202.

[22] M. Kirchmann, K. Eichele, L. Wesemann. *Inorg. Chem*. **2008**, *47*, 5988.

[23] B.G. de Boer, A. Zalkin, D.H. Templeton. *Inorg. Chem*. **1969**, *8*, 836.

[24] W. Haubold, W. Keller, G. Sawitzki. *Angew. Chem.* **1988**, *100*, 958.

[25] M. Somer, M. Hartweg, K. Peters, H.G. von Schnering. *Z. Kristallogr*. **1990**, *191*, 311.

[26] M. Somer, K. Peters, H.G. von Schnering. *Z. Kristallogr*. **1990**, *194*, 133.

[27] M. Somer, T. Popp, K. Peters, H.G. von Schnering. *Z. Kristallogr*. **1990**, *193*, 281.

[28] M. Somer, W.C. Cabrera, E.M. Peters, K. Peters, H.G. von Schnering. *Z. Kristallogr*. **1995**, *210*, 779.

[29] M. Somer, T. Popp, K. Peters, H.G. von Schnering. *Z. Kristallogr*. **1990**, *193*, 297.

[30] P. Sims, T. Aoki, R. Favaro, P. Wallace, A. White, C. Xu, J. Menendez, J. Kouvetakis. *Chem. Mater*. **2015**, *27*, 3030.

[31] N. Vojteer, V. Sagawe, J. Stauffer, M. Schroeder, H. Hillebrecht. *Chem. Eur. J*. **2011**, *17*, 3128.

CHAPTER 5. SYNTHESIS OF METAL BORIDES USING BI_3 AS A BORON SOURCE

The contents of this chapter have been modified from the manuscript
Woo, K. E.; Chang, J.; Kovnir, K. Synthesis of Metal Borides Using BI_3 as a Boron Source. (Unpublished)

5.1 Introduction

Metal borides have found use in a wide variety of applications, including Fe_2B coatings [1], Co-B and Mo-B catalysts for H_2 generation [2], LaB_6 as a hot cathode [3], and VB_2 anodes for primary batteries [4] to name a few. However, simple solid state synthesis of metal borides is hindered by the inertness of boron and oftentimes the metal as well. Traditional methods to make metal borides are high-temperature reactions of the elements by arc-welding, borothermic reduction of metal oxides, or use of metal fluxes [5]. These all require high temperatures over 1273 K and often require further purification due to oxygen or other contamination from a flux or the reaction vessel.

Known low temperature (<1273 K) synthesis methods include the use of a metal flux or a solid state metathesis reaction. Fokwa et al. were able to use a Sn flux to synthesize OsB and TiB_2 powders at 1173 K [6] as well as a larger variety of metal borides by pressing and annealing a combination of a metal chloride, elemental boron, and tin powder [7]. The use of a metathesis reaction to form early transition metal borides was discussed by Rao et al. in 1995 [8]. However, this study was restricted to the synthesis of Group 4-6 metal diborides, where metal chloride precursors were reacted with MgB_2 at 1173 K. The syntheses of HfB_2 and tungsten borides were also found to be formed by the reaction of Hf or W metal and a boron halide [9] instead of using a metal halide precursor. Henschel et al. also predicted the formation of other transition metal borides via thermodynamically based calculations.

While mainly the lighter boron halides have been used to synthesize metal borides, BI_3 has the additional benefit of being in solid form, greatly increasing the ease of handling. BI_3 thermally decomposes at a low temperature under reduced pressure, and was shown to transport pure boron via heat gradient. In addition, any unreacted BI_3 can hydrolyze into H_3BO_3 and HI, which can be easily dissolved in water [10]. Herein, we present a more in depth study on the formation of a large variety of metal boride compositions using BI_3.

5.2 Methods

5.2.1 Powder X-Ray Diffraction (XRD)

Powder XRD experiments were done using a Rigaku 600 Miniflex diffractometer using Cu-K_α radiation and a Ni-K_β filter. Samples were ground with an agate mortar and pestle and loaded with grease on a zero-background Si holder to minimize preferred orientation.

5.2.2 In Situ Powder Synchrotron XRD

Ni powder and BI_3 crystals totaling 50 mg were ground together with an agate mortar and pestle. The mixture was then loaded into a silica capillary (0.5 mm ID × 0.7 mm OD, Friedrich & Dimmock, Inc.). The capillary was evacuated and flame sealed. Beamline 17-BM-B at the Advanced Photon Source at Argonne National Lab was used. The sample was loaded onto a flow cell equipped with electric heaters and exposed to synchrotron radiation (λ = 0.24125 Å). Data was collected as the sample was heated at 30 K/min to 573 K, ramped at 10 K/min to 1073 K, immediately cooled 20 K/min to 573 K, and then 50 K/min to 348 K. Temperature correction was performed by heating pure samples of Sn, Ge, and Sb and determining their melting points. A calibration curve was then calculated based on these values. Analysis of data was performed using GSAS-II [11].

5.2.3 Scanning Electron Microscopy (SEM) and Energy Dispersive X-Ray Spectroscopy (EDS)

Presence of iodine and metal content was detected using an FEI Quanta 250 FE-SEM equipped with an Oxfords X-Max 80 detector. Powder samples were loaded into a graphite die, which was then filled with epoxy and polished smooth. A thin conductive carbon film was then deposited on the surface of the puck.

5.3 Synthesis

Boron iodide (Sigma Aldrich, 99.8%) and metals of choice (Ti, Alfa Aesar, 99.9%; Fe, Sigma Aldrich, 99.99%; Co, Alfa Aesar, 99.8%; Ni, Alfa Aesar, 99.996%) were used as received and handled inside an argon glovebox. Reagents were loaded into 17 mm ID x 19 mm OD silica tubes with a 14 mm x 16 mm silica plug for an enclosed length of roughly 9 cm. The amount of BI_3 per reaction was limited to less than 650 mg to prevent any potential explosions due to vapor pressure at reaction temperatures. The tube and reaction materials were cooled in an ice bath as it was evacuated to ~10^{-2} mbar and then flame sealed under static vacuum. Starting ratios of reagents for select borides are shown in Table 5.1. The sealed tube was laid on its side in a muffle furnace to achieve a slight temperature gradient with the reagents pointing to the back of the furnace. The default heating profile for these reactions was a 2 h ramp to 1073 K and annealing at that temperature for 24 h. After annealing, the sample was opened to air (unless specified elsewhere) and washed in deionized water for 2 days. The product was then filtered using a nylon membrane filter and air dried. The Fe reaction was further washed in dilute HCl for a day to remove FeO(OH) side product and then filtered using a polypropylene membrane filter.

Table 5.1 *Starting ratios for select metal borides*

Metal boride	**Metal:BI_3 ratio**
TiB_2	5 Ti:5 BI_3
Fe_2B	7 Fe:2 BI_3
Co_2B	7 Co:2 BI_3
Ni_3B	7 Ni:2 BI_3

5.4 Results and Discussion

5.4.1 Synthesis

We have shown recently that the refractory boride, BP, can be synthesized using BI_3 [12]. In the current work we extended this synthesis to first row transition metals. Similar to solid state metathesis reactions, the main driving force for M + BI_3 reactions is the formation of thermodynamically stable metal iodides. For the selected metals Ti, Fe, Co, and Ni, phase-pure or almost phase-pure polycrystalline metal boride powders can be synthesized using the optimized ratios described in Table 5.1 (Figure 5.1). Co_2B and Fe_2B could be synthesized by a salt balanced reaction stoichiometry, i.e. no excess of metal or halide is expected in the products, 7 Co + 2 BI_3 $\rightarrow$ 2 Co_2B + 3 CoI_2. In turn, Ni_3B and TiB_2 required an excess of BI_3 for a complete reaction. These resulting borides possess high melting points (from 1429 K for Ni_3B to 3498 K for TiB_2), but this method allows them to be synthesized at a moderate temperature. The melting points of the reacting metals alone are well over 1273 K, with Ni melting at 1728 K and Ti melting at 1941 K.

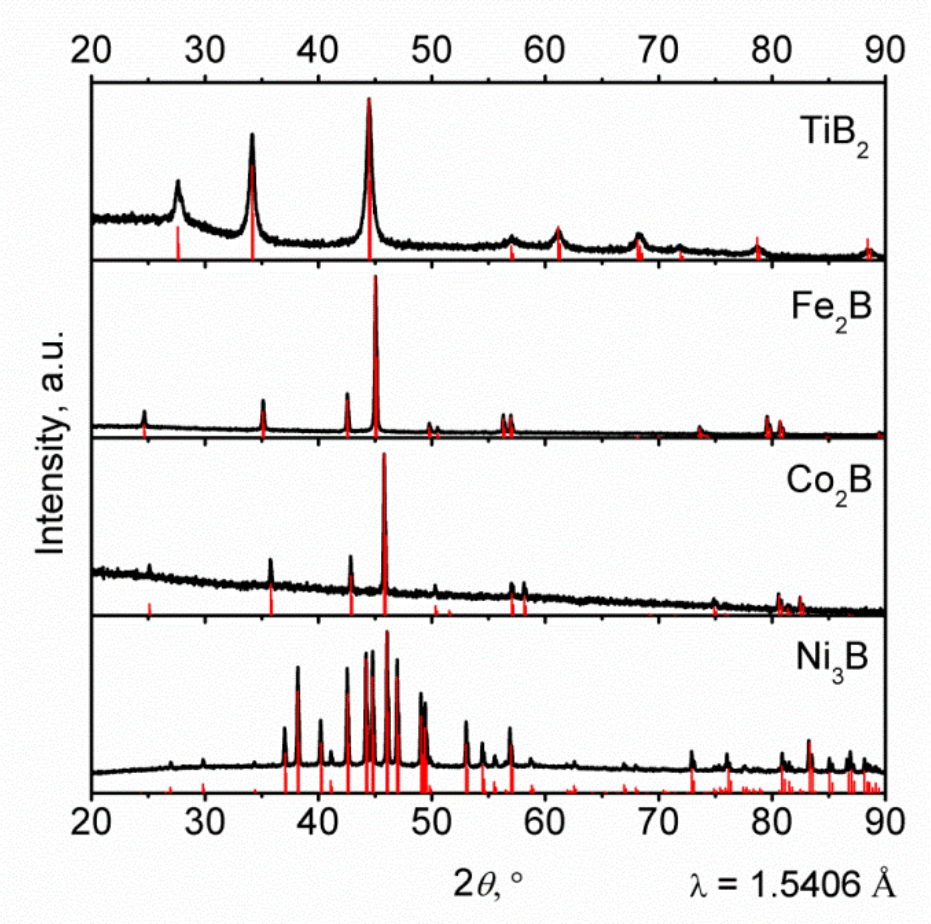

Figure 5.1 *Powder XRD patterns of TiB_2, Fe_2B, Co_2B, and Ni_3B. Red lines correspond to calculated powder patterns.*

A study on adjusting the starting ratios for synthesizing Ni_3B showed that a large excess of BI_3 resulted in the formation of Ni_6BSi_2 (via reaction with the silica tube) and a stoichiometric reaction of 9 Ni:2 BI_3 or reactions with higher Ni content resulted in unreacted Ni as a product. As detailed in Table 5.2, Ni_2B could be synthesized as well, given a slight excess of BI_3, though always with Ni_3B as a side product. An unknown amorphous phase was detected in the reactions producing Ni_6BSi_2, possibly also a result from a reaction with the silica tube.

Table 5.2 *Ratio of Ni:BI_3 starting reagents and corresponding products detected by powder XRD.*

Ni	BI_3	Powder XRD Result (washed)
0.67	2	Ni_6BSi_2
2	2	Ni_6BSi_2 + Ni_3B + Ni_2B
4	2	Ni_3B + Ni_2B
5	2	Ni_3B + Ni_2B
7	2	Ni_3B
9	2	Ni + Ni_3B
11	2	Ni + Ni_3B

*Note: 7 Ni + 2 BI_3 → 2 Ni_2B + 3 NiI_2

Other metals, including the rest of the first row transition metals (Ti-Zn) as well as Mg, Si, Ru, Pt, Au, and La, were investigated using starting ratios for salt balanced reactions (assuming the most stable metal iodide would be the co-produced salt). Crystalline VB_2 could be synthesized with an amorphous side phase, which was revealed to be V_2B_3 after reannealing at 1373 K for 24 h. CrB, Ru_7B_3, and LaB_6 were successfully synthesized using the heating profile (annealing at 1273 K) described in the experimental section, although unreacted metal remained in the product in each case. It may be possible for these borides to be synthesized phase pure or almost phase pure with modifications to the starting ratios, as with the case for Ni_3B and TiB_2. The metals that did not form discernable borides, Mg, Mn, Cu, Zn, Si, Pt, and Au, may require a different heating profile.

5.4.2 In Situ Powder XRD

To better understand the reaction and gain insight as to how the synthesis of other metal borides may be adjusted, in situ experiments were performed on nickel boride (Figure 5.2). By 315 K, BI_3 had decomposed or gone into gas phase, leaving only Ni to be detected by XRD. At 561 K, NiI_2 is formed. Some new peaks briefly appear in the powder patterns

from 734 K to 905 K, which can be assigned to Ni_4B_3. Almost all Ni has been reacted by 840 K, and Ni_2B is detected. At 1086 K, NiI_2 goes into melt and Ni_2B is all that is detected. Surprisingly, Ni_2B was all that was detected by the end of the experiment aside from a small amount of NiI_2, suggesting that it is possible to isolate other boride compounds of the same metal. Given the distribution of materials in the capillary, an increased vapor pressure or possibly the lack of heat gradient may have contributed to the synthesis of pure phase Ni_2B rather than Ni_3B. The small scale of the reaction may have prevented accurate loading ratios of the starting materials, which may have led to the preferred formation of Ni_2B. There is a persistent peak in the powder patterns at around 3.3°, but it is unknown as to which phase it belongs to.

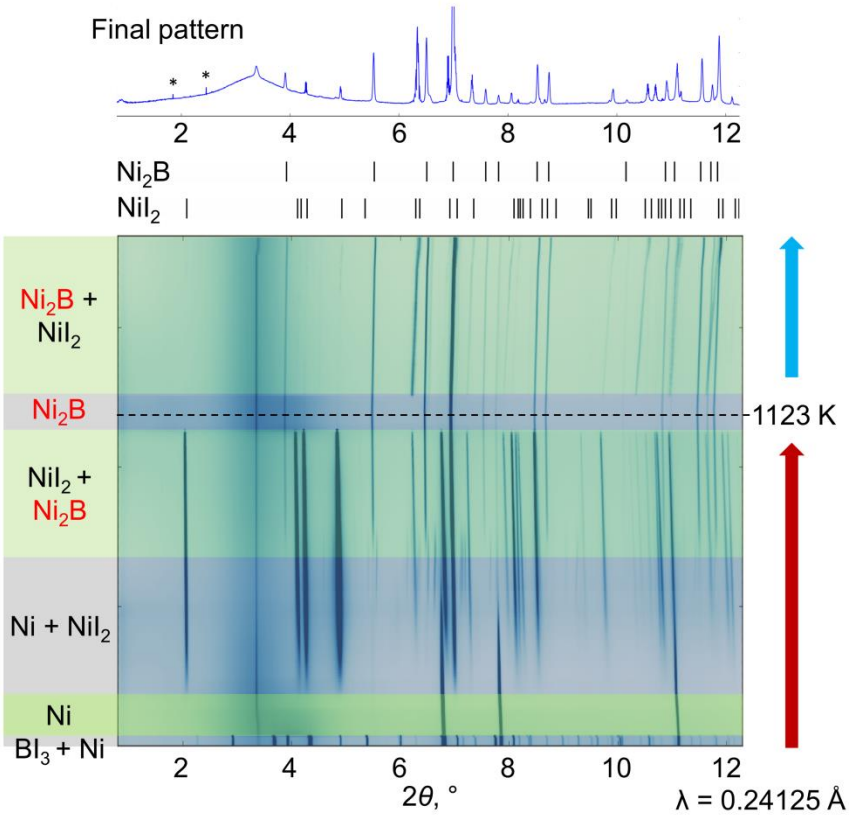

Figure 5.2 *Contour plot of in situ powder XRD patterns upon the reaction of Ni and BI_3. On top is the resulting powder pattern with tic marks corresponding to calculated positions for Ni_2B and NiI_2. Asterisks mark artifacts in the powder pattern.*

5.4.3 Topotactic Reaction

These reactions are ideal for generating metal borides of unique morphologies. A large surface area is well known to be important for catalysts, and so the Ni_3B reaction was repeated using Ni foam (Sigma Aldrich, 95%). Whilst a slight amount of Ni_2B was detected by powder XRD, a predominantly Ni_3B foam was successfully synthesized, albeit brittle (Figure 5.3).

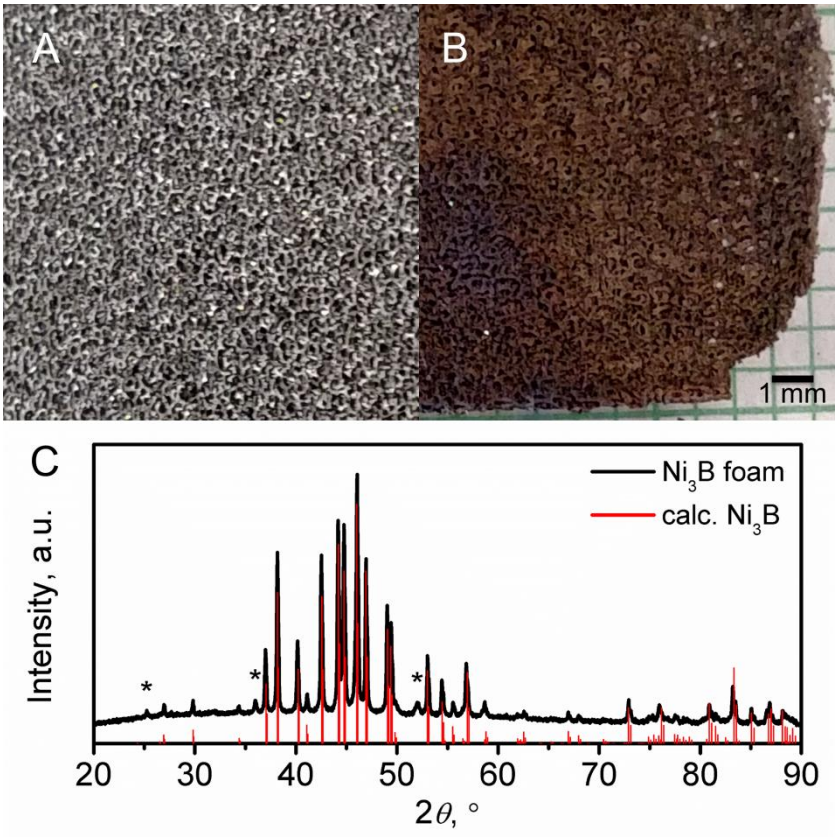

Figure 5.3 *Photos of A) Ni foam, B) Ni_3B foam, and C) a powder XRD pattern of the Ni_3B foam. Asterisks mark peaks of Ni_2B.*

Reacting with less BI_3 (11 Ni:2 BI_3) appeared to reduce the brittleness of the resulting Ni_3B foam. Unreacted Ni was detected as expected. This foam was still stiff and did not retain the flexibility of the original Ni foam.

5.4.4 Ternary Borides

Aside from Ni_6BSi_2 that was due to a reaction with the silica reaction vessel, most initial attempts for ternary borides were unsuccessful. With the additional element in the reaction equation, predicting the co-produced metal iodide and corresponding stoichiometries was more difficult. Mimicking the synthesis of Ni_6BSi_2, La was reacted with a large excess of BI_3 (63 BI_3:7 La in comparison to 6 BI_3:7 La used for synthesis of binary LaB_6) with the hypothesis that Si would be leached from the reaction vessel and a La-Si-B compound would be formed. The reaction tube was opened within a glove box and the products were analyzed via an air-free powder XRD measurement. Surprisingly, LaI_3 was the only compound detected, and no solids were recovered after washing. Additional insight to the reaction of La with BI_3 was revealed in an attempt to synthesize $LaCo_2B_2$. With a starting ratio of 1 La:2 Co:2 BI_3, only pure phase CoB was detected after washing. Compared to reactions in which simple binaries are the target phase, this reaction contained twice the amount of BI_3 for La and 3.5 times the amount for Co. This suggests that a large excess of BI_3 with La only results in LaI_3, and the transported boron reacts instead with whatever alternate venue exists, such as walls of the silica tube or in this case, Co to form CoB.

Another trial to synthesize a ternary metal boride first involved the synthesis of a Ni/Co alloy. This was achieved by grinding a 1:1 molar ratio of Ni and Co powder together, which was then loaded in a silica tube and heated to 1173 K for 72 h. The resulting alloy ingot could not be crushed, and was instead cut into smaller pieces using diagonal cutting pliers. These pieces were loaded in a 7:2 molar ratio of the alloy and BI_3 in accordance with the Ni_3B synthesis. The resulting product was a malleable foil and grey-brown powder. Powder XRD detected the powder to resemble clean Ni_3B or Co_3B, albeit with various peak

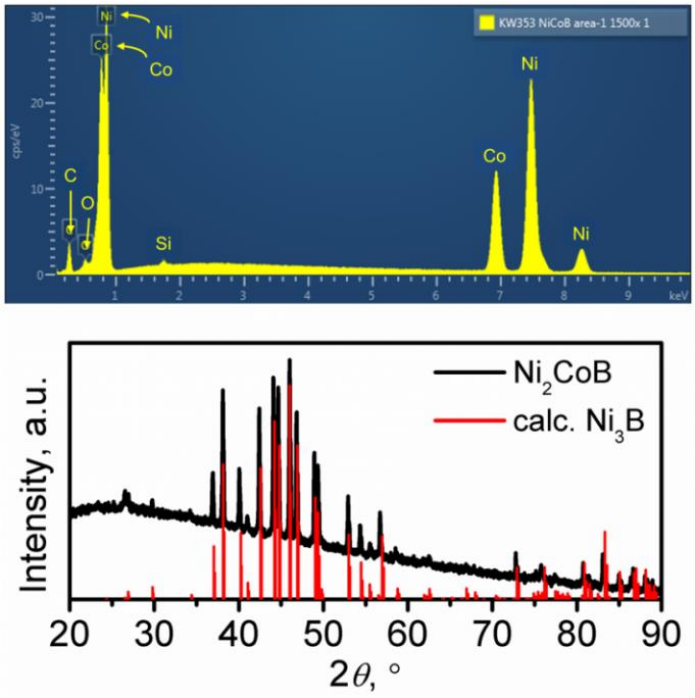

Figure 5.4 *EDS spectrum (top) and powder XRD (bottom) of Ni_2CoB. High background is due to fluorescence contribution from Co.*

shifts (Figure 5.4). Analysis by EDS found the powder to contain Ni and Co in a 70:30(3) ratio. Different areas of the sample were analyzed, and the chemical composition was almost identical for all areas. This gives a final composition of $Ni_{2.1}Co_{0.9(1)}B$, or Ni_2CoB, assuming a 3:1 molar ratio of metals to B, as identified by powder XRD. Less than 1% atomic percent of Si was also detected, possibly due to particles of the silica vessel falling into the sample when the tube was broken open. The foil was most likely unreacted NiCo alloy and was composed of 47.3(3)% Ni and 52.7(6)% Co. Boron is too light to be accurately determined by EDS, and its signal has a high tendency to overlap with C and O signals, which is ubiquitous in all samples. The synthesis of Ni_2CoB suggests that ternary borides may be successfully synthesized when using a compound precursor to react with BI_3, rather than individual metal elements.

5.5 Conclusion

Various metal borides spanning across the transition metal group were successfully synthesized. TiB_2, VB_2, CrB, CrB_2, Fe_2B, Co_2B, Ni_3B, Ru_7B_3, and LaB_6 were all synthesized using BI_3 by a quick 24 h anneal at 1123 K. Evidence exists that other compositions of metal borides can be synthesized using this method provided a few modifications, as was the case for CoB when La was included in the reaction mixture or the preferred formation of Ni_2B in the in situ reaction. Foam Ni_3B was synthesized using Ni foam as a starting reagent. As such, there is a potential for metal borides of various morphologies to be synthesized, which can be useful for various applications such as catalysis. Ternary Ni_2CoB was synthesized by first forming a NiCo alloy. This compound may be interesting to investigate for hydrogen fuel production as a Ni-Co-B catalyst (with a 1:1 Ni:Co ratio as observed by EDS) was found to be effective in $NaBH_4$ solutions [13]. Further experimentation is required to figure out the appropriate starting ratios and heating profile needed to synthesize the metal borides that did not form using the basic strategy described in this work. A larger variety of ternary borides may be synthesized using a metal precursor.

5.6 Acknowledgements

We would like to thank Dr. Wenqian Xu and Dr. Andrey Yakovenko for assistance in synchrotron data collection and Shannon Lee for epoxy preparations for EDS measurements. We would also like to thank Dr. Yuri Kolen'ko for providing the Ni foam. This research is supported by the ACS Petroleum Research Fund, grant 55036-DNI10. Use of the Advanced Photon Source at Argonne National Laboratory was supported by the U. S. Department of Energy, Office of Science, Office of Basic Energy Sciences, under Contract No. DE-AC02-06CH11357.

5.7 References

[1] J. Jiang, Y. Wang, Q. Zhong, Q. Zhou, L. Zhang. *Surf. Coat. Technol.* **2011**, *206*, 473.

[2] a) C. Wu, F. Wu, Y. Bai, B. Yi, H. Zhang. *Mater. Lett.* **2005**, *59*, 1748; b) S.U. Jeong, E.A. Cho, S.W. Nam, I.H. Oh, U.H. Jung, S.H. Kim. *Int. J. Hydrogen Energy* **2007**, *32*, 1749; c) F. Baydaroglu, E. Ozdemir, A. Hasimoglu. *Int. J. Hydrogen Energy* **2014**, *39*, 1516; d) H. Park, A. Encinas, J.P. Scheifers, Y. Zhang, B.P.T. Fokwa. *Angew. Chem. Int. Ed.* **2017**, *56*, 5575; e) P.R. Jothi, Y. Zhang, J.P. Scheifers, H. Park, B.P.T. Fokwa. *Sustainable Energy Fuels* **2017**, *1*, 1928; f) H. Park, Y. Zhang, J.P. Scheifers, P.R. Jothi, A. Encinas, B.P.T. Fokwa. *J. Am. Chem. Soc.* **2017**, *139*, 12915.

[3] P.H. Schmidt, L.D. Longinotti, D.C. Joy, S.D. Ferris, H.J. Learny, Z. Fisk. *J. Vac. Sci. Technol.* **1978**, *15*, 1554.

[4] a) H.X. Yang, Y.D. Wang, X.P. Ai, C.S. Cha. *Electrochem. Solid-State Lett.* **2004**, *7*, A212; b) J. Stuart, M. Lefler, C.P. Rhodes, S. Licht. *J. Electrochem. Soc.* **2015**, *162*, A432.

[5] J. Greim, K.A. Schwetz. *Ullman's Encyclopedia of Industrial Chemistry*, Wiley-VCH, Weinheim, Germany **2006**.

[6] B.P.T. Fokwa, P.R.N. Misse, M. Gilleßen, R. Dronskowski. *J. Alloys Compd.* **2010**, *489*, 339.

[7] P.R. Jothi, K. Yubuta, B.P.T. Fokwa. *Adv. Mater.* **2018**, *30*, 1704181.

[8] L. Rao, E.G. Gillan, R.B. Kaner. *J. Mater. Res.* **1995**, *10*, 353.

[9] a) A. Henschel, M. Binnewies, M. Schmidt, H. Borrmann, Y. Grin. *Chem. Eur. J.* **2017**, *23*, 15869; b) A. Henschel, M. Binnewies, M. Schmidt, R. Köppe, U. Burkhardt, Y. Grin. *Chem. Eur. J.* **2018**, *24*, DOI: 10.1002/chem.201801778.

[10] a) J. Cueilleron, J.C. Viala. *J. Less Common Met.* **1978**, *58*, 123; b) J. Cueilleron, J.C. Viala. *J. Less Common Met.* **1979**, *65*, 167.

[11] B. H. Toby, R. B. Von Dreele, *J. Appl. Crystallogr.* **2013**, *46*, 544.

[12] K.E. Woo, K. Lee, K. Kovnir. *Mater. Res. Express* **2016**, *3*, 074003.

[13] J.C. Ingersoll, N. Mani, J.C. Thenmozhiyal, A. Muthaiah. *J. Power Sources* **2007**, *173*, 450.

CHAPTER 6. EXPLORATION OF NOVEL INORGANIC COMPOUNDS WITH B-P COVALENT BONDS

The contents of this chapter have been modified from the manuscript
Woo, K. E. and Kovnir, K. Exploration of Novel Inorganic Compounds with B-P Covalent Bonds. (Unpublished)

6.1 Introduction

There are very few ternary boron phosphides currently known, largely due to difficulties in boron reactivity. Other Group 13 elements such as Al or Ga easily form ternaries with pnictides, such as $AE_3Al_2Pn_4$ (AE = Ca, Sr, Ba, Eu; Pn = P, As) and $Ba_3Al_3Pn_5$ (Pn = P, As) (as well as their Ga counterparts), by way of a metal or self-reacting flux [1]. Ternary transition metal indium phosphide compounds, such as Cu_5InP_{16}, can be made by a direct reaction of elements [2]. These methods are viable for non-boron Group 13 metals due to their low melting points, ranging from 303 K to 933 K. However, this is not feasible for boron, as its melting point is over 2273 K and requires temperatures over 1273 K for an appreciable amount of boron to dissolve in other metals such as aluminum, copper, or nickel [3]. Boron does not dissolve in fluxes with lower melting points such as Sn, Bi, or Sb [4]. In spite of these challenges, there are hundreds of metal borides that are known. Boron phosphide, a very stable compound with a melting point of 1373 K and resistant to oxidation or corrosion from *aqua regia*, has also been known since 1957 [5].

A detailed analysis of the Cambridge Structural Database (compounds containing a C–H bond) demonstrated that there are over 1200 compounds with the B–P covalent bond. In turn, an analysis of the Inorganic Crystal Structure Database (compounds without a C–H bond) revealed that the amount of known ternary boron phosphide compounds that contain B–P bonds number less than 10 since the discovery of $B_4F_6PF_3$ in 1969 [6] (Figure 6.1).

Nearly 20 years later, $P_2B_4Cl_4$ was found in 1988 [7], but metal boron phosphide compounds weren't discovered until A_3BP_2 (A = Na, Cs, K) in 1990 and Rb_3BP_2 in 1995 [8]. Given the abundance of metals that have been shown to react with boron in spite of difficulties with inertness and the apparent stability of the B–P bond, more metal boron phosphide compounds should exist.

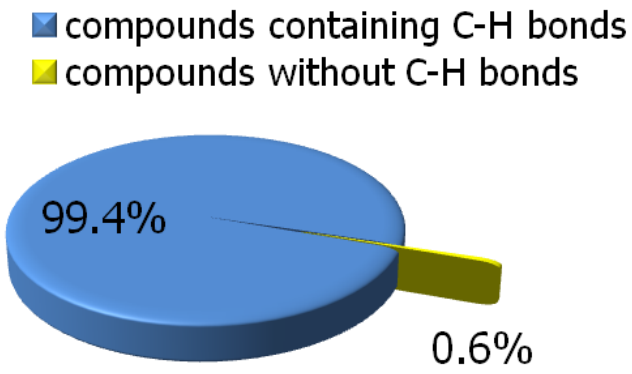

Figure 6.1 *Structurally characterized compounds containing at least one B–P covalent bond.*

Prior attempts to synthesize ternary metal borides in our research group included reactions of amorphous boron, red phosphorus, and a metal, but these resulted in only binaries. As such, solid state metathesis was explored as an alternate venue for synthesizing a new metal boron phosphide. This technique utilizes the intrinsic energy of reagents to form a salt with high reaction enthalpy [9]. Solid state metathesis was shown to be effective in synthesizing new transition metal carbodiimides, some of which were predicted to be thermodynamically unstable, such as MCN_2 (M = Mn, Co, Ni, Fe), $Sm_2(CN_2)_3$, and $LiY(CN_2)_2$ [10]. As such, solid state metathesis was chosen as a main method for investigating the synthesis of new ternary metal boron phosphide compounds. Herein, we present the different attempts on synthesizing metal boron phosphides and the following results with a main focus on copper, as well as a new Na_2BP_2 compound.

6.2 Methods

6.2.1 Synthesis

All handling of chemicals were performed in an argon filled glovebox.

Na_3BP_2 was synthesized by following the method given by von Schnering [1990]. Stoichiometric ratios of Na (Alfa Aesar, 99.95%), B (Sigma Aldrich, >95%), and P (Sigma Aldrich, >97%) were loaded into a Nb ampoule. The Nb ampoule was arc welded shut and flame sealed within an evacuated silica jacket to prevent oxidation of the vessel. The tube was then heated over 12 h to 1100 K in a muffle furnace, annealed at that temperature for 4 h, then slow cooled to room temperature over 40 h. Phase purity was checked with powder XRD.

In solid state metathesis reactions, a ratio of 1:1 Na_3BP_2:metal halide was loaded in a silica tube. Once loaded, the tube was evacuated and flame sealed, and then placed in a muffle furnace. The general heating profile was ramping 1 h to 773 K and then dwelling at that temperature for 1 h. The sample was opened and stored in an argon filled glovebox.

6.2.2 Powder X-Ray Diffraction (XRD)

Powder XRD experiments were done using a Rigaku 600 Miniflex diffractometer using Cu-K_α radiation and a Ni-K_β filter. Samples were ground with an agate mortar and pestle and loaded with grease on modified air-free Si holders with Kapton caps. The Kapton background was manually subtracted from the sample pattern.

6.2.3 In Situ Powder Synchrotron XRD

Na_3BP_2 and CuCl (Alfa Aesar, 99.999%) were ground separately with an agate mortar and pestle and mixed well to avoid premature reaction. Other metal halides were ground together with Na_3BP_2. The mixture was loaded in a silica capillary (0.5 mm ID × 0.7 mm OD, Friedrich & Dimmock, Inc.). The capillary was evacuated and flame sealed.

Beamline 17-BM-B at the Advanced Photon Source at Argonne National Lab was used. The sample was loaded onto a flow cell equipped with electric heaters and exposed to synchrotron radiation. Temperature correction was performed by heating pure samples of Sn, Ge, and Sb and determining their melting points. A calibration curve was then calculated based on these values.

6.2.4 Single Crystal XRD

Table 6.1 *Data collection and unit cell parameters of* Na_2BP_2

Composition	$\mathbf{Na_2B_{1.06(8)}P_{2.00(8)}}$
Formula weight (g/mol)	119.49
Temperature (K)	100(2)
Radiation, λ	Mo-Kα, 0.71073 Å
Crystal system	Orthorhombic
Space group	*Pna*2$_1$ (No. 33)
***a* (Å)**	9.568(1)
***b* (Å)**	6.1044(7)
***c* (Å)**	3.2013(5)
***V* (Å^3)**	186.98(4)
Z	2
ρ_{calc} (g cm^{-3})	2.12
μ (mm^{-1})	1.13
2θ limits, °	3.96-22.97
Data/param.	262/39
R_1	0.052
wR_2	0.120
Goodness-of-fit	1.14
Diff. peak/hole (e/Å^3)	0.63/-0.38

Single crystal data was collected on a Bruker Venture D8 diffractometer with a Mo-ImS microsource and Photon CMOS detector. The data set was collected at 100 K in a nitrogen gas atmosphere. The Bruker SAINT software in the APEX3 package was used to

integrate the raw data, and multiscan absorption corrections were applied [11]. Crystal structure solution and refinement was performed using the SHELX suite [12]. The crystal was refined as a 2-component inversion twin. Data collection and unit cell parameters are summarized in Table 6.1. Crystal structure images were generated using VESTA [13].

6.3 Results & Discussion

6.3.1 Solid State Metathesis

Solid state metathesis using the precursors Na_3BP_2 and a metal halide was the first course of action in attempts to synthesizing new metal boron phosphide compounds. The metal halides used in these reaction attempts included chlorides of the first row transition metals (Ti-Zn), AgCl, $LaCl_3$, and iodides of fifth row main group elements (Sn, Sb, and Te). As Na_3BP_2 already contains B–P bonds in the $[BP_2]^{3-}$ ion, this method would theoretically allow the preservation of the B–P bond while exchanging the metal cation. Given that metathesis reactions tend to occur very quickly due to self-propagation, a 1:1 ratio of Na_3BP_2 and metal halide was first annealed at 773 K for an hour. This generally resulted in the formation of the sodium halide, binary metal phosphides, occasionally the metal itself, and an unknown compound as observed by powder XRD. The unknown compound could not be detected by powder XRD after exposure to water, and low crystallinity BP was detected

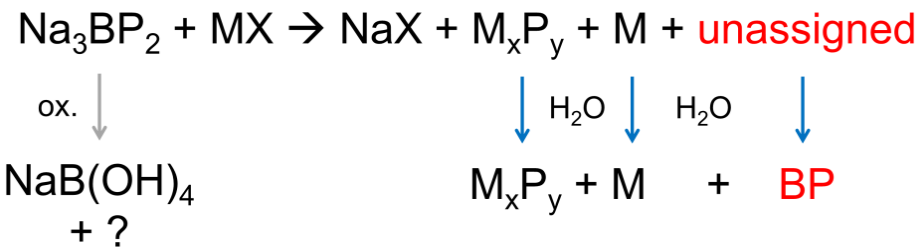

Figure 6.2 *Schematic of the reaction of Na_3BP_2 and a metal halide and resulting products after oxidation or water washing.*

instead (Figure 6.2). This suggests the presence of B-P bonding within the unknown compound. Oxidation was easily observed when the sample was removed from an inert environment, even when covered by a thin layer of paraffin oil applied within the glovebox, indicating a high sensitivity to air. To ensure that these products were not due to the decomposition of Na_3BP_2, powder patterns were taken of Na_3BP_2 after exposure to air and water. $NaB(OH)_4$ was detected after oxidizing Na_3BP_2, as well as unassigned peaks that resembled the diffraction of potassium decanedioate. No solids were recovered after washing with deionized water except for a miniscule amount of NbP due to reaction with the Nb ampoule.

The reaction with CuCl was especially reactive as grinding of the starting materials with an agate mortar and pestle in an argon filled glovebox would cause ignition. This however resulted in incomplete reactions, and so the starting materials were merely shaken for homogeneous mixing prior to annealing by furnace. Unlike the other metal halides that were attempted, the reaction with CuCl only resulted in NaCl and an unknown compound without copper phosphides or Cu (Figure 6.3). As such, a majority of the presented work focused on the copper system.

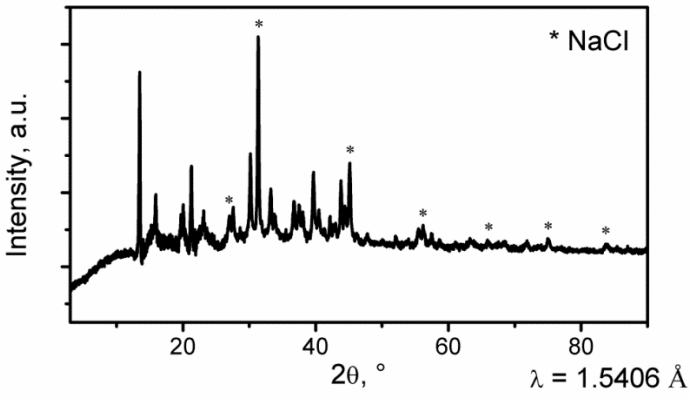

Figure 6.3 *Powder XRD pattern of the product "Na-Cu-B-P" from the reaction of Na_3BP_2 and CuCl.*

To better understand the metathesis reaction between Na_3BP_2 and CuCl, the two starting compounds were loaded in a silica capillary for in situ synchrotron experiments. The sample was heated to 1123 K at a rate of 15 K/min. Once it hit 1123 K, the reaction sat at this temperature for 30 min before rapidly cooling to 323 K. Trace amounts of sodium phosphides were found prior to heating, which may either have been impurities from synthesizing Na_3BP_2 that were undetected by lab powder XRD or degradation of Na_3BP_2 during transport to the beamline. By 645 K, the binary phosphides had gone into melt. At temperatures as low as 442 K, NaCl began to form, thus indicating that the metathesis reaction had begun to occur. Cu metal was also detected at this point, suggesting that CuCl is first reduced during the metathesis reaction. Around the temperature of 773 K, the unknown "Na-Cu-B-P" phase began to form. Raising the temperature to 967 K saw the formation of $NaCu_2P_2$, and partial melt with the formation of Cu_3P was achieved at 1099 K. Cooling after melting only achieved NaCl and Cu_3P (Figure 6.4).

While only Cu_3P and NaCl were detected when the reaction was heated to 1123 K, the isolation of "Na-Cu-B-P" was possible with in situ experiments only going to 773 K (Figure 6.5). Using a ramp rate of 20 K/min, we observed the formation of "Na-Cu-B-P" forming at temperatures as low as 645 K. Cu was still found as an intermediate prior to the formation of "Na-Cu-B-P." The compound remained stable when holding at 805 K for 30 min and was still detected once the reaction cooled. As such, it is apparent that reaching temperatures above the melting point of NaCl is detrimental to this new compound.

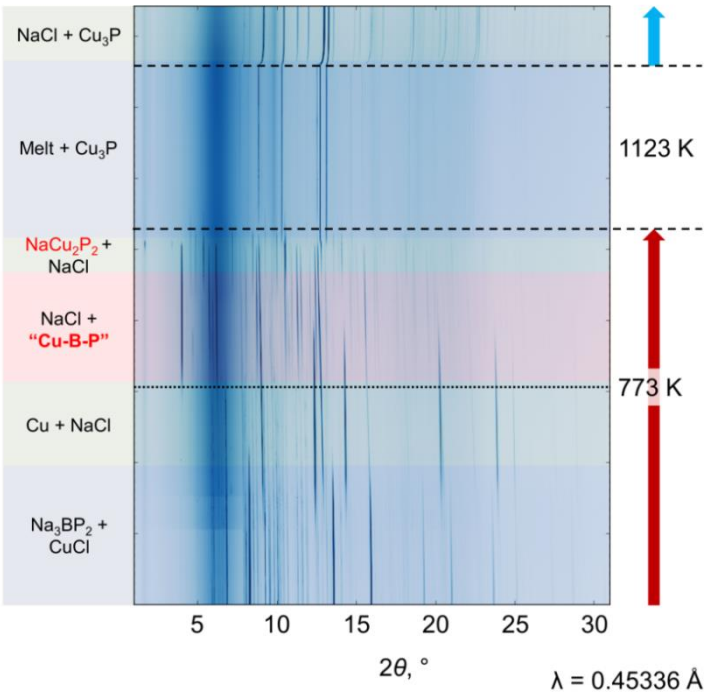

Figure 6.4 *Contour plot of in situ powder synchrotron XRD patterns for "Na-Cu-B-P" heating up to 1123 K.*

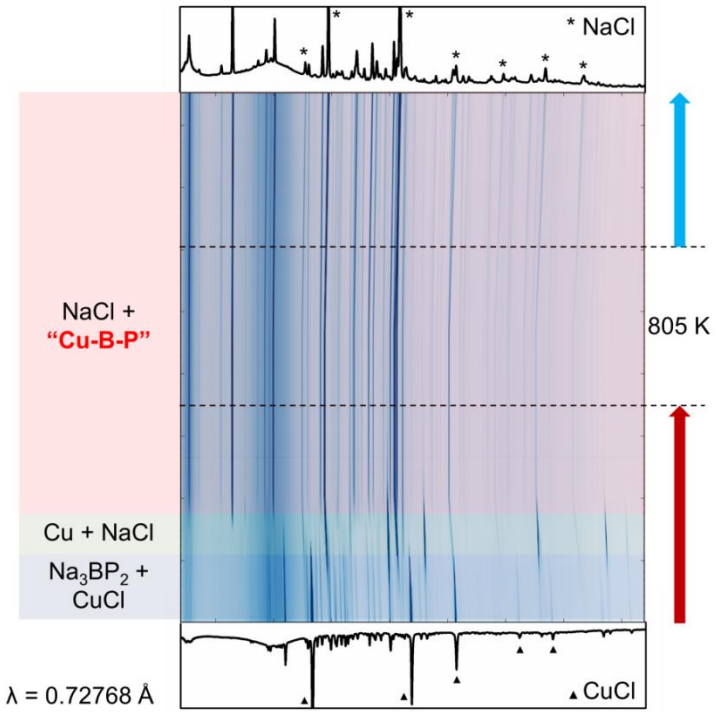

Figure 6.5 *Contour plot of in situ powder synchrotron XRD patterns for "Na-Cu-B-P" heating up to 805 K.*

With the potential of B partially substituting Cu or inserting between the Cu-P layers of $NaCu_2P_2$ (Figure 6.6), the synthesis was repeated while dwelling at 973 K. $NaCu_2P_2$ was detected by powder XRD, but crystals large enough to run single crystal diffraction experiments were not found. Annealing for 120 h at 973 K did not yield larger crystals. This prolonged annealing time was also unsuccessful in producing large crystals for "Na-Cu-B-P."

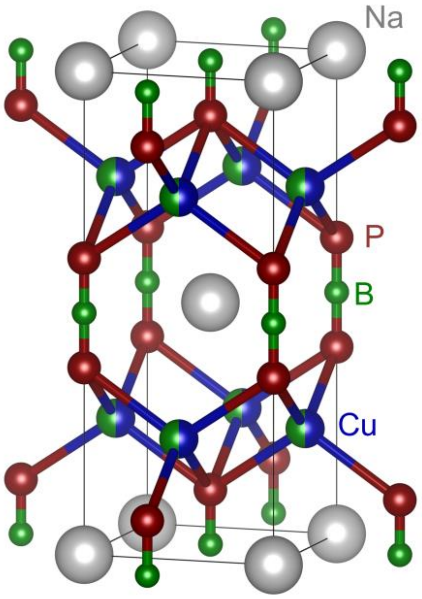

Figure 6.6 *Theoretical B insertion between phosphorus atoms or partial Cu substitution in* $NaCu_2P_2$.

6.3.2 Na_2BP_2

The synthesis of "Na-Cu-B-P" was attempted using a 1 CsI:0.94 NaI flux and a slightly slower ramp of 3 h to 773 K. CuI was also used as a starting material rather than CuCl to lessen the amount of different elements in the reaction. The resulting products were glittery red and black clumps of powder. NaI, Cu, and a new but different than "Na-Cu-B-P" phase were detected by powder XRD. Through single crystal XRD, a small black crystal was found to be $Na_2B_{1.06(8)}P_{2.00(8)}$, which will be referred to as Na_2BP_2. While the calculated

diffraction pattern of Na_2BP_2 did not match the peaks associated with "Na-Cu-B-P," it fit the powder pattern of the unknown product of the CsI/NaI flux reaction.

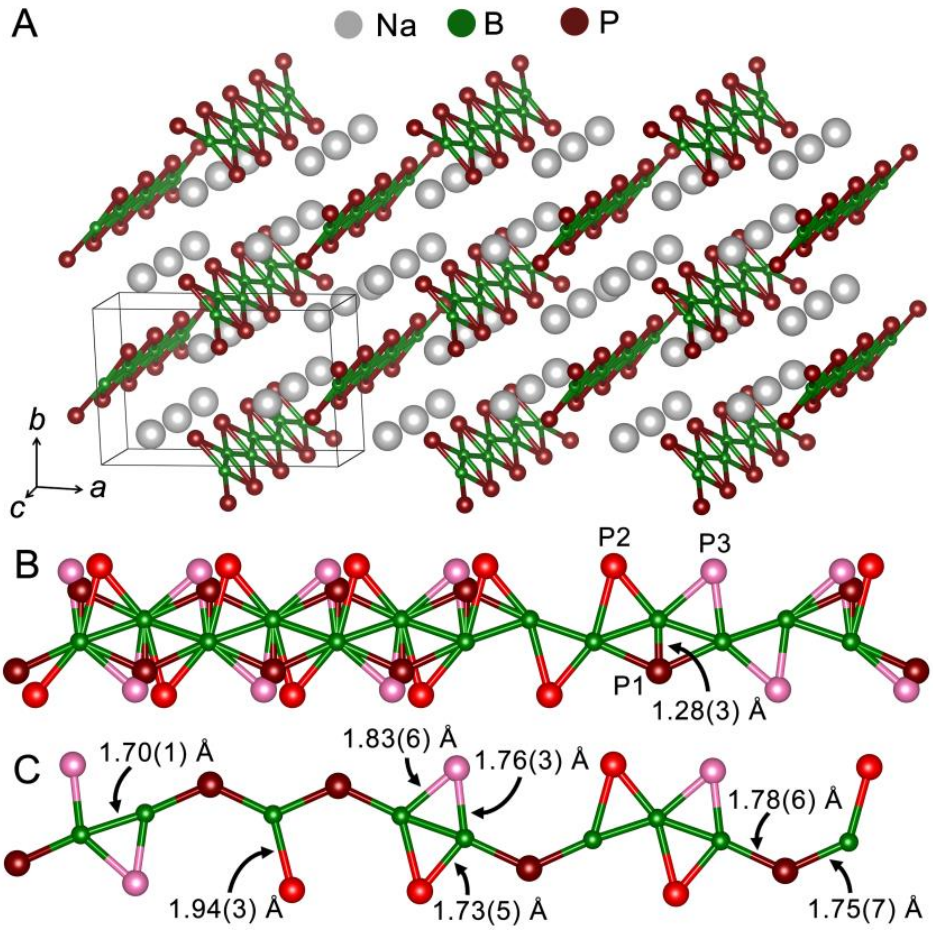

Figure 6.7 *Crystal structure of Na_2BP_2 with A) all boron and average phosphorus positions shown, B) the B-P chain showing all possible positions, and C) a hypothetical B-P chain taking into account reasonable B-P bond distances of 1.7-2.1 Å.*

The formation of Na_2BP_2 can be considered as the product of Na leaching from the starting compound, Na_3BP_2. Oxidation of the linear borophosphide $[BP_2]^{3-}$ anions causes them to condense into one dimensional B-P chains (Figure 6.7A). Focusing on the B-P chains, the one boron site has 53(4)% occupancy, and phosphorus is split into three positions. Solving in the non-centrosymmetric space group of *Pna*2_1 causes the split phosphorus positions to form a scalene triangle (Figure 6.7B). The shortest known multiple B–P bond is

1.767 Å in K_3BP_2 [8a] compared with the 1.965 Å single bond in cubic BP [14]. P1 has a very short distance to B in Figure 6.7B, 1.28(3) Å, and so both atoms cannot exist at the same time. Instead, P1 interrupts the boron chain and acts as a bridging phosphorus atom to connect the next nearest boron atoms together. With the presence of boron, P2 and P3 are positioned further away at more reasonable distances from boron, and B–B bonds can be formed (Figure 6.7C).

6.3.3 Non-Copper In Situ Experiments

The reactions of $MnCl_2$, $FeCl_2$, $CoCl_2$, $ZnCl_2$, and SnI_2 with Na_3BP_2 were also observed via in situ synchrotron XRD. A similar reaction was found in which the metal halide would first be reduced to its elemental form. In all cases, sodium halide successfully formed, and the reaction temperature was brought to above the melting point of the sodium halide.

Table 6.2 *Comparison of lab powder X-ray and in situ synchrotron results of main phosphide compounds. Temperature of lab synthesis and formation in synchrotron experiments is listed after each compound.*

Metal Halide	Lab X-Ray	Synchrotron
$MnCl_2$	MnP + NaMnP (823 K)	MnP (475 K), NaMnP (475 K)
$FeCl_2$	FeP + Fe_2P (773 K)	FeP (354 K), Fe_2P (354 K)
$CoCl_2$	CoP (823 K)	Co_2P (302 K), CoP (443 K)
$ZnCl_2$	NaZnP (623 K)	NaZnP (418 K), $ZnSiP_2$ (1049 K)
SnI_2	NaSnP (823 K)	NaSnP (422 K)

The main phosphide compounds found during the in situ experiments were the same as the compounds produced in reactions performed in the lab, except for the case of $CoCl_2$ (Table 6.2). There appeared to be a tendency for NaMP compounds to form if they were reported to exist, otherwise the reaction would only form binary phosphides. In every case

except for NaSnP, these ternary compounds decomposed or melted by the time the accompanying sodium halide salt melted and were unable to recrystallize. NaSnP recrystallized after melt along with elemental Sn.

6.3.4 BI_3 Transport Reaction

Given the success of synthesizing metal borides and boron phosphide using BI_3 as a boron source [15], BI_3 was used in an attempt to synthesize this elusive "Na-Cu-B-P" compound instead of Na_3BP_2. The method for synthesizing metal borides using BI_3 also uses the highly thermodynamically favored formation of a metal iodide as the driving force. BI_3 also doubles as a transport agent, allowing for high reactivity of boron as it goes into gas phase [16]. When annealed at 1173 K for 4 h, CuI and $Cu_{1.98}P_3I_2$ were detected by powder XRD as well as a set of peaks that could not be assigned to any known compound listed in the crystallographic database. However, this set of peaks differed from the unknown compound found by solid state metathesis. As the main difference between the BI_3 transport and solid state metathesis methods are the presence or absence of Na or I, we hypothesize that "Na-Cu-B-P" formed with Na_3BP_2 in fact incorporates Na atoms into its crystal structure.

Copper boride was not successfully synthesized using the basic synthesis method that was reported in Chapter 5, but Ni_3B can be synthesized phase-pure. As such, another attempt at using BI_3 was used with Ni and P. However, the reaction of 3 BI_3:1 Ni:1 P at 1023 K only resulted in Ni_2P and cubic BP.

6.3.5 Direct Reaction of Elements

Prior attempts to synthesize a ternary B-P compound resulted in binary phosphides and occasionally, borides. Following the hypothesis that Na is contained within the Cu-B-P structure, the same procedure to synthesize Na_3BP_2 was followed, with 1 molar equivalent of

Cu instead of CuCl as a starting material. However, this mainly resulted in the formation of Na_2CuP.

6.4 Conclusions

Many attempts using various techniques were done to synthesize a new metal boron phosphide. Research using copper was emphasized due to its high reactivity in solid state metathesis reactions with Na_3BP_2 and the subsequent absence of binary admixtures in this reaction. An unknown "Na-Cu-B-P" compound appeared to be synthesized at low temperatures of 773 K that was highly instable in air or water. Through in situ synchrotron experiments, $NaCu_2P_2$ was discovered to briefly form as a product of the decomposition or melting of "Na-Cu-B-P". Both "Na-Cu-B-P" and $NaCu_2P_2$ would decompose once the co-produced NaCl went into melt and would not recrystallize upon cooling. Therefore we can conclude that achieving melt is detrimental to the synthesis of these compounds. Using a CsI/NaI flux, a new Na_2BP_2 compound was discovered. Although it does not contain a transition metal, loss of Na compared to Na_3BP_2 creates a new structure containing a B-P chain with partial boron occupancy and split phosphorus positions. Learning from all the failed and more successful attempts to synthesize new ternary boron phosphide compounds, a foundation has been established, and there are still other venues that should be explored, such as solvothermal or flux methods. The leaching of Na, harking back to the synthesis of Si clathrates by leaching Na through thermal decomposition [17], should also be more thoroughly explored to target Na_2BP_2 and other Na-deficient B-P compounds.

6.5 Acknowledgements

We would like to thank Dr. Wenqian Xu and Dr. Andrey Yakovenko for assistance in synchrotron data collection as well as Dr. Juli-Anna Dolyniuk, Dr. Josh Greenfield, and Shannon Lee for performing the in situ "Na-Cu-B-P" experiment to 773 K. This research is

supported by ACS Petroleum Research Fund, grant 55036-DNI10. Use of the Advanced Photon Source at Argonne National Laboratory was supported by the US Department of Energy, Office of Science, Office of Basic Energy Sciences, under Contract No. DE-AC02-06CH11357.

6.6 References

[1] a) H. He, C. Tyson, M. Saito, S. Bobev. *J. Solid State Chem.* **2012**, *188*, 59; b) H. He, C. Tyson, M. Saito, S. Bobev. *Inorg. Chem*. **2013**, *52*, 499.

[2] S. Lange, M. Bawohl, R. Weihrich, T. Nilges. *Angew. Chemie. Int. Ed.* **2008**, *47*, 5654.

[3] a) O.N. Carlson. *Binary Alloy Phase Diagrams, II Ed., ed. T.B. Massalski* **1990**, *1*, 123; b) D.J. Chakrabarti, D.E. Laughlin. *Binary Alloy Phase Diagrams, II Ed., ed. T.B. Massalski* **1990**, *1*, 474; c) P.K. Liao, K.E. Spear. *Binary Alloy Phase Diagrams, II Ed., ed. T.B. Massalski* **1990**, *1*, 508.

[4] a) H. Okamoto. *Binary Alloy Phase Diagrams, II Ed., ed. T.B. Massalski* **1990**, *1*, 538; b) H. Okamoto. *J. Phase Equilib*. **1991**, *12*, 391; c) H. Okamoto. *Binary Alloy Phase Diagrams, II Ed., ed. T.B. Massalski* **1990**, *1*, 531.

[5] P. Popper, T.A. Ingles. *Nature*. **1957**, *179*, 1075.

[6] B.G. de Boer, A. Zalkin, D.H. Templeton. *Inorg. Chem*. **1969**, *8*, 836.

[7] W. Haubold, W. Keller, G. Sawitzki. *Angew. Chem.* **1988**, *100*, 958.

[8] a) M. Somer, M. Hartweg, K. Peters, H.G. von Schnering. *Z. Kristallogr*. **1990**, *191*, 311; b) M. Somer, T. Popp, K. Peters, H.G. von Schnering. *Z. Kristallogr*. **1990**, *193*, 281; c) M. Somer, T. Popp, K. Peters, H.G. von Schnering. *Z. Kristallogr*. **1990**, *193*, 297. d) M. Somer, K. Peters, H.G. von Schnering. *Z. Kristallogr*. **1990**, *194*, 133; e) M. Somer, W.C. Cabrera, E.M. Peters, K. Peters, H.G. von Schnering. *Z. Kristallogr*. **1995**, *210*, 779.

[9] H.-J. Meyer. *Dalton Trans.* **2010**, *39*, 5973.

[10] a) X. Liu, M. Krott, P. Müller, C. Hu, H. Lueken, R. Dronskowski. *Inorg. Chem.* **2005**, *44*, 3001; b) M. Krott, X. Liu, B.P.T. Fokwa, M. Speldrich, H. Lueken, R. Dronskowski. *Inorg. Chem.* **2007**, *46*, 2204; c) X. Liu, L. Stork, M. Speldrich, H. Lueken, R. Dronskowski. *Chem. Eur. J.* **2008**, *15*, 1558; d) M. Neukirch, S. Tragl, H.-J. Meyer. *Inorg. Chem.* **2006**, *45*, 8188; e) L. Unverfehrt, M. Ströbele, H.-J. Meyer. *Z. Anorg. Allg. Chem.* **2012**, *639*, 22.

[11] Bruker (2008). *APEX3*. Bruker AXS Inc., Madison, Wisconsin, USA.

[12] G. M. Sheldrick, *Acta Crystallogr., Sect. C: Struct. Chem.* **2015**, *71*, 3.

[13] K. Momma, F. Izumi, *J. Appl Crystallogr.* **2011**, *44*, 1272.

[14] S. Rundqvist. *Acta Chem. Scand.* **1962**, *16*, 1.

[15] a) A. Henschel, M. Binnewies, M. Schmidt, H. Borrmann, Y. Grin. *Chem. Eur. J.* **2017**, *23*, 15869; b) A. Henschel, M. Binnewies, M. Schmidt, R. Köppe, U. Burkhardt, Y. Grin. *Chem. Eur. J.* **2018**, *24*, DOI: 10.1002/chem.201801778; c) K.E. Woo, K. Lee, K. Kovnir. *Mater. Res. Express* **2016**, *3*, 074003.

[16] J. Cueilleron, J.C. Viala. *J. Less Common Met.* **1978**, *58*, 123.

[17] H. Horie, T. Kikudome, K. Teramura, S. Yamanaka. *J. Solid State Chem.* **2009**, *182*, 129.

CHAPTER 7. CONCLUSIONS

In the past five years, I have dealt with reactions involving two notoriously inert elements—silicon and boron. Although they belong to two different groups, Group 14 and 13 respectively, they are known to share similar characteristics. Both are semiconductors, classified as semimetals, and have one of the highest melting and boiling points of the semimetals and nonmetals, only being surpassed by carbon [1]. The main goal with these elements was to create new multinary compounds with much more reactive arsenic or phosphorus and a metal. I aimed for compounds containing covalent bonds between the main group elements. Through the successful synthesis of these compounds, we would not only learn how to address the reaction of elements of highly different reactivities, but also define structure-property relationships of new structures.

Working with Si and As, two major groups of compounds have been discussed. First are those composed of Mg-Si-As, and the other is a family of $Cs_{0.16}M_xSi_{1-x}As_2$ (M = Cu, Zn, Ga). With Mg-Si-As, the previously highly theoretical non-centrosymmetric $MgSiAs_2$ was finally brought into experimental reality using a method of repeated grinding and annealing of the starting elements. The next compound, $Mg_3Si_6As_8$, was surprisingly found to crystallize in a non-centrosymmetric space group. However, unlike $MgSiAs_2$, which showed a decent second harmonic generation response, the high cubic symmetry of $Mg_3Si_6As_8$ forbade that unique property from occurring. Although optical properties may not be the primary focus of $Mg_3Si_6As_8$, its electronic structure suggests that it may have potential as a thermoelectric material. Doping may be required for this property to be realized. A third compound, $Mg_3Si_3As_8$ was discovered after running the synthesis for $Mg_3Si_6As_8$ for 480 h instead of only 140 h. $Mg_3Si_3As_8$ and its Zn-doped variant, $Mg_{2.6}Zn_{0.4}Si_3As_8$, finally

crystallize in a centrosymmetric space group. Drawing crystallographic structural elements from both $MgSiAs_2$ and $Mg_3Si_6As_8$, this compound may have interesting properties to discover and research.

$Cs_{0.16}M_xSi_{1-x}As_2$ (M = Cu, Zn, Ga) is a unique family of 2-D compounds that appear to accept high levels of modifications to its chemical composition while retaining its structure. Varying amounts of Cu, Zn, and Ga can partially occupy the Si site in the Si-As framework, and the compound can be synthesized with the rest of the Group 1 elements. The 2-D nature and interspersed Cs atoms between the layers encourage low thermal conductivity, a favored trait in thermoelectric materials such as with the famous SnSe compound [2]. While several challenges pose problems with pressing dense pellets, techniques such as time-domain thermoreflectance can be performed on single crystals and determine room temperature thermal conductivity. If a large enough crystal can be grown, the Seebeck coefficient may be determined, perhaps using a technique as described by H. Takahashi et al. for $FeSb_2$ [3], allowing for the compound's efficiency as a thermoelectric material to be evaluated. Given the favorable flexibility of $Cs_{0.16}M_xSi_{1-x}As_2$ (M = Cu, Zn, Ga) to modifications of its chemical composition while retaining its overall structure, it would be interesting to see whether the 1+ cation can be replaced by a 2+ metal, such as Ba or Sr, or even a 3+ metal, such as La or Eu. Examples of intercalation of these metals have been demonstrated in other systems, such as Ba in β-FeSe to give $Ba_{0.28}Fe_2Se_2$, increasing the T_c from 8 K to 34 K [4] or Eu in TiS_2 to make $Eu_{0.10}TiS_2$ [5].

Moving from Si to the less reactive element boron, the main goal was to discover new ternary metal boron phosphides with B–P bonds. Compounds of this type are few and far in between, either synthesized with alkali metals as A_3BP_2 (A = Na, K, Rb, Cs) [6] or with a

very low percentage of B–P bonds due to B or P being doped in the compounds, as with the cases of $Li(P_xC_{1-x})_2B_{12}$ [7] and $(Al_{1-x}B_x)PSi_3$ [8]. First, while investigating methods of synthesizing cubic BP, $Sn_{0.02}B_{0.98}P$ was found by using a Sn flux. In addition, a new synthesis method in which phosphorus was reacted with BI_3 at temperatures below 1273 K to form BP was also developed, leading to the easy synthesis of metal borides by this same method. Ternary Ni_2CoP was successfully synthesized by using a NiCo alloy and BI_3, and topotactic reactions were proven possible with the synthesis of a Ni_3B foam.

As the BI_3 method can be likened to solid state metathesis reactions, and prior attempts to synthesize metal boron phosphides by direct reaction of elements were unsuccessful, we turned to a true solid state metathesis reaction using Na_3BP_2 as a starting material to react with a metal halide to synthesize new metal boron phosphides. This technique had been shown to synthesize thermally labile compounds, such as $MnCN_2$ from $ZnCN_2$ [9]. This posed great interest as the $[CN_2]^{2-}$ ion is isostructural to the $[BP_3]^{3-}$ ion in Na_3BP_2, and so the B–P bond would already exist and theoretically be preserved during the formation of a new metal boron phosphide compound via this reaction. Of course, hypothesis tends to be simpler than reality, and a new metal boron phosphide was not formed so easily. Focusing on using CuCl to react with Na_3BP_2 resulted in a potentially new compound formed at a low temperature of 773 K that was detected by powder X-ray diffraction (XRD), although a large enough crystal was not found for single crystal XRD experiments. Performing in situ synchrotron experiments revealed the formation of $NaCu_2P_2$ at a slightly higher temperature of 1023 K. There is potential for B to insert itself in the crystal structure, but a large enough single crystal for this compound was also not achieved by lab experiments to confirm this hypothesis. In the end, a new metal boron phosphide compound was found

when using a CsI/NaI flux, though unexpectedly not with Cu or another transition metal. Instead, the new compound was Na_2BP_2, essentially a Na leached version of Na_3BP_2 in which the $[BP_2]^{3-}$ ions of Na_3BP_2 condensed into a B-P chain in Na_2BP_2. This B-P chain consists of bridging phosphorus atoms and B–B bonds. The crystal quality of the measured sample was admittedly not the best, but the synthesis can now be altered since the chemical composition is now known, and there is potential to grow a larger and higher quality crystal. There is still much work to do to finally synthesize a transition metal boron phosphide, but much of a foundation has been laid.

7.1 References

[1] F.A. Cotton, G. Wilkinson. *Advanced Inorganic Chemistry, 4th ed.*, John Wiley and Sons, Inc., New York, USA, **1980**.

[2] a) L.-D. Zhao, S.-H. Lo, Y. Zhang, H. Sun, G. Tan, C. Uher, C. Wolverton, V.P. Dravid, M.G. Kanatzidis. *Nature* **2014**, *508*, 373; b) L.-D. Zhao, G. Tan, S. Hao, J. He, Y. Pei, H. Chi, H. Wang, S. Gong, H. Xu, V.P. Dravid, C. Uher, G.J. Snyder, C. Wolverton, M.G. Kanatzidis. *Science* **2015**, aad3749; c) K. Peng, X. Lu, H. Zhan, S. Hui, X. Tang, G. Wang, J. Dai, C. Uher, G. Wang, X. Zhou. *Energy Environ. Sci.* **2016**, *9*, 454; d) C. Chang, M. Wu, D. He, Y. Pei, C.F. Wu, X. Wu, H. Yu, F. Zhu, K. Wang, Y. Chen, L. Huang. *Science* **2018**, *360*, 778.

[3] H. Takahashi, R. Okazaki, S. Ishiwata, H. Taniguchi, A. Okutani, M. Hagiwara, I. Terasaki. *Nat. Commun.* **2016**, *7*, 12732.

[4] K.V. Yusenko, J. Sottmann, H. Emerich, W.A. Crichton, L. Malavasi, S. Margadonna. *Chem. Commun.* **2015**, *51*, 7112.

[5] V. Cajipe, P. Molinié, A.M. Marie, P. Colombet. *Chem. Mater.* **1990**, *2*, 409.

[6] a) M. Somer, M. Hartweg, K. Peters, H.G. von Schnering. *Z. Kristallogr*. **1990**, *191*, 311; b) M. Somer, T. Popp, K. Peters, H.G. von Schnering. *Z. Kristallogr*. **1990**, *193*, 281; c) M. Somer, T. Popp, K. Peters, H.G. von Schnering. *Z. Kristallogr*. **1990**, *193*, 297. d) M. Somer, K. Peters, H.G. von Schnering. *Z. Kristallogr*. **1990**, *194*, 133; e) M. Somer, W.C. Cabrera, E.M. Peters, K. Peters, H.G. von Schnering. *Z. Kristallogr*. **1995**, *210*, 779.

[7] N. Voltjeer, V. Sagaw, J. Stauffer, M. Schroeder, H. Hillebrecht. *Chem. Eur. J.* **2011**, *17*, 3128.

[8] P. Sims, T. Aoki, R. Favaro, P. Wallace, A. White, C. Xu, J. Menendez, J. Kouvetakis. *Chem. Mater.* **2015**, *27*, 3030.

[9] H.-J. Meyer. *Dalton Trans.* **2010**, *39*, 5973.